UNIVERSITY OF SOUTHAMPTON
Faculty of Engineering and Applied Science
Department of Electronics and Computer Science

Ferro-electrets material in human body energy harvesting

By
Junjie Shi

Thesis for the degree of Doctor of Philosophy

May 2017

UNIVERSITY OF SOUTHAMTPON

ABSTRACT

FACULTY OF PHYSICAL AND APPLIED SCIENCES

DEPARTMENT OF ELECTRONIC AND COMPUTER SCIENCE

Doctor of Philosophy

FERROE-ELECTRETS MATERIAL IN HUMAN BODY ENERGY HARVESTING

By Junjie Shi

Using piezoelectric materials to harvest energy from human movement provides a potential power source to wearable devices and electronic textiles in everyday life. Two common comerical piezoelectric material: lead zirconate titante (PZT) and polyvinylidene fluoride (PVDF) are unsuitable for human body energy harvesting applications due to the high hardness and fragility of PZT and the low piezoelectric coefficients of PVDF. Ferroelectret is a thin polymer foam that can store electric charges in its internal voids, have strong piezoelectric properties and low elastic modulus which would make them very desirable for human body energy harvesting. The piezoelectricity of ferroelectrets originates from the combination of the internally stored charges and the cellular structures. However, the resulting pizoelectric properties of commercialized ferroelectrets are limited by the random individual void geometry and irregular overall cellular structure due to its existing fabrication processes.

This work develop a numerical model using finite element analysis (FEA) approach to design and optimize the structure of ferroelectret during fabrication. Based on the models, we used polydimethysiloxane (PDMS) materials to fabricate ferroelectrets with different internal structures. The fabrication is done by casting method with 3D-printed moulds and silicon moulds produced using MEMS processes. The piezoelectric properties of fabricated PDMS ferroelectret are investigated to further validate the accuracy of our proposed numerical model in the work. The designed PDMS ferroelectret presented a maximum piezoelectric coefficient d_{33} of 520 pC/N. It can provide the maximum output voltage of 13 V and average output of 2.73 μW when connected to a 65 MΩ resistive load under a

compressive force of 800 N at human normal walking model. The optimization PDMS ferroelectret strucutre for human body energy harvesting is also evaluated. In additon, a method for further improving the PDMS ferroelectret piezoelectric stability is proposed.

Contents

List of Figures **5**

List of Tables **11**

Declaration of Authorship **13**

Acknowledegments **15**

Abbreviations **17**

1 Introduction **1**

1.1 Overview of the research 1

1.2 Objective and scope of the research 4

1.3 Statement of novelty 5

1.4 Publications generated from this thesis 5

1.5 Structure and content of this thesis 6

2 Literature Review **7**

2.1 Introduction 7

2.2 Harvesting energy from human body 7

2.2.1 Overview of energy harvesting 7

2.2.2 Electromagnetic generators 10

2.2.3 Electrostatic generators 13

2.2.4 Piezoelectric generators 14

2.2.5 Discussion 17

2.3 Ferroelectrets 18

2.3.1 Piezoelectric properties of ferroelectrets 18

2.3.2 Model 24

2.3.3 Typical ferroelectret materials and applications 26

2.4 Ferroelectret fabrication technologies 30

2.4.1 Homogeneous ferroelectrets 30

2.4.2 Heterogeneous ferroelectrets 35
2.4.3 Discussion 42
2.5 Electrical charging for ferroelectret 43
2.5.1 Principle of ferroelectret charging 43
2.5.2 Description of charging process 46
2.5.3 Charging techniques 48
2.6 Conclusions 53
3 Analytical Model and ANSYS Simulation 54
3.1 Introduction 54
3.2 Analytical model 54
3.3 ANSYS simulation 63
3.3.1 Parameters of ferroelectret model 64
3.3.2 Principle of ANSYS simulation 65
3.3.3 The effects of void size and void shape 69
3.3.4 The effects of void distribution 72
3.4 Conclusions 73
4 PDMS Ferroelectret Fabricated by 3D Printed Moulding Method..... 74
4.1 Introduction 74
4.2 Fabrication process 74
4.2.1 Mould preparation 74
4.2.2 PDMS casting and bonding 76
4.2.3 Electrical charging 78
4.3 Experimental setup 79
4.3.1 Inspection of structure 79
4.3.2 Investigation of electromechanical property 80

4.4 Investigation of 3D printed PDMS ferroelectret 82
4.4.1 Inspection of cellular structure 82
4.4.2 Investigation of electromechanical properties 84
4.5 Conclusions 89
5 PDMS Ferroelectret Fabricated by Silicon Mould Method 91
5.1 Introduction 91
5.2 Fabrication process 91
5.2.1 Silicon mould fabrication process flow 91
5.2.2 Photomask design 93
5.2.3 PDMS casting and bonding 100
5.3 Experiments and results 102
5.3.1 Inspection of cellular structure 103
5.3.2 Piezoelectric coefficients measurement 104
5.3.3 Investigation of energy harvesting performance 109
5.4 Conclusions 116
6 PDMS Ferroelectet with Enhanced Piezoelectricity 118
6.1 Introduction 118
6.2 Principle 118
6.3 Fabrication process 122
6.4 Investigation of surface potential 123
6.5 Investigation of electromechanical properties 125
6.5.1 Piezoelectric coefficients measurement 125
6.5.2 Energy harvesting performance 127
6.6 Conclusion 129
7 Conclusions and Future Work 131

7.1 Conclusion 131
7.2 Outlook 133

List of References..... 135

List of Figures

Figure 2-1: Total power from body driven sources for each action [34].....10

Figure 2-2: The schematic of electromagnetic harvester for pacemaker [35].....11

Figure 2-3: The schematic of the hip electromagnetic generator [36].....12

Figure 2-4: Structure of the generator for knee prosthesis [37].....12

Figure 2-5: Honeycomb-type variable capacitor [38].....13

Figure 2-6: Schematic of electrostatic induction harvester using electret [39].....14

Figure 2-7: Energy harvesting shoe [41].....15

Figure 2-8: Impact coupled piezoelectric generator [42].....15

Figure 2-9: Assembly and exploded view of pendulum excited piezoelectric harvester [44].....16

Figure 2-10: Ashby material property chart [56].....21

Figure 2-11: Dependence of piezoelectricity (thick line) and elastic stiffness (thin line) on the density and the corresponding void shape [58-59].....22

Figure 2-12: Simplified model based on charged parallel polymeric and gaseous layers.....24

Figure 2-13: Piezoelectric coefficient as a function of the electret charge density in the absence of external loads [74].....25

Figure 2-14: Piezoelectric coefficient as a function of the static pressure in the absence of external voltage [74].....26

Figure 2-15: The sleep monitor system based on ferroelectrets by Emfit [136].....28

Figure 2-16: SEM photographs of cross sectional view of commercial PP film.....31

Figure 2-17: Phase diagram of CO_2 [100].....33

Figure 2-18: (a) Schematic of the laboratory fabrication process; (b) Optical micrograph of a typical ferroelectret system with tubular channels [105] 36

Figure 2-19: Schematic of preparation process of laminated films [107] 37

Figure 2-20: Scanning-electron microscopy images of the surface of a laminated film (upper part) and cross sections of laminated films (middle and bottom parts) [92] 38

Figure 2-21: Schematic of fabrication process based on PDMS [108] 40

Figure 2-22: SEM photographs of top view, 3D view and cross sectional view of fabricated cellular PDMS microstructures [108] 40

Figure 2-23: Schematic of fabrication process based on parylene and SEM image of parylene beams [109] 41

Figure 2-24: Schematic diagrams of the screen-printing process (a), and of the steps for manufacturing void-containing PC polymer systems ((b) and (c)). (d) Digital photographs of sample prepared by screen-printing process [110] 42

Figure 2-25: Breakdown voltage as a function of the gap distance in air at a pressure of 1 bar according to Paschen's law 45

Figure 2-26: Breakdown electric field as a function of the gap distance in air at a pressure of 1 bar according to Paschen's law 45

Figure 2-27: Electric charging process in a void. $V_{charging}$ is the charging voltage between the sample electrodes; E_{local} is the real electric field in the void, which is the superposition of $E_{void-ext}$ from the external charges on the electrodes, and $E_{void-int}$ from the internal deposited charges; $E_{breakdown}$ is the breakdown threshold. 47

Figure 2-28: Schematic of the contact charging system with temperature controller 49

Figure 2-29: Schematic of the tip-to-plane corona charging system 50

Figure 3-1: A simplified model for the piezoelectricity of a charge-implanted cellular structure 54

Figure 3-2: (a) Analytical rectangle model results varying with the size of voids and (b) the schematic of the structure changing with tr_1 and sr_1 58

Figure 3-3: the relationship between the number of void layer n and the optimised ratio of tr_1 ..59

Figure 3-4: A simplified model for the piezoelectricity of a charge-implanted cellular structure with parallelogram void 60

Figure 3-5: A simplified model for the piezoelectricity of a charge-implanted cellular structure with sector void 60

Figure 3-6: The values of sr_1 varying with the slope of parallelogram 62

Figure 3-7: The values of sr_1 varying with the radius of the sector 63

Figure 3-8: The structure of ferroelectret models with rectangle (a), parallelogram (b) and sector void (c) for ANSYS simulation 65

Figure 3-9: (a) The model feature for Mesh options; (b) the resulting mesh for ferroelectret ANSYS simulations 66

Figure 3-10: Force applied on ferroelectret for ANSYS simulation 67

Figure 3-11: An image of ANSYS simulation deformation results for single rectangle void layer ferroelectret in thickness direction 68

Figure 3-12: Analytical model results and ANSYS simulation d33 results for rectangle voids varying with sr_1 at tr_1=0.8 69

Figure 3-13: Analytical model results and ANSYS simulation d33 results for rectangle voids varying with tr_1 at sr_1=0.4 69

Figure 3-14: Analytical model results and ANSYS simulation d33 results for parallelogram voids varying with the slope 71

Figure 3-15: Analytical model results and ANSYS simulation d33 results for sector voids varying with the radius of curve 71

Figure 3-16: ANSYS simulation of void deformation ratio results varying with off horizontal centreline ratio 72

Figure 3-17: The schematic showing off horizontal centreline ratio 73

Figure 4-1: (a) The image of a prepared 3D-printed mould and (b) the schematic of the 3D printed mould 76

Figure 4-2: Schematic of fabrication processes 77

Figure 4-3: Image of cross-section view of single layer PDMS ferrelectret 78

Figure 4-4: Schematic illustration of the tip-to–plane corona charging system 79

Figure 4-5: Illustration of the PM300 system for piezeoelectric coefficient d_{33} measurement 80

Figure 4-6: The LSM image of cross section view of the realised voids 82

Figure 4-7: The optical microscope image of cross section view for middle area of ferroelectret 83

Figure 4-8: The optical microscope image of cross section view for end area of ferroelectret 83

Figure 4-9: Measured piezoelectric coefficients of three PDMS structure over a month period 85

Figure 4-10: Measured voltage output of under compressive force with 1 Hz force frequency, 800N and 21MΩ load resistance 86

Figure 4-11: Measured voltage output of under compressive force at different frequency with 800N and 21MΩ loading resistance 87

Figure 4-12: Power-resistance trace of PDMS ferroelectret under compressive force with 17 Hz force frequency, 800 N 88

Figure 4-13: Measured voltage output of under compressive force at different force with 17 Hz and 21 MΩ loading resistance 89

Figure 5-1: Schematic of rectangular void silicon mould fabrication process 92

Figure 5-2: The schematic of parallelogram void silicon mould fabrication process 93

Figure 5-3: The mask design for the fabrication of in silicon mould for (a) parallelogram void ferroelectret (b) rectangular void ferroelectet.....94

Figure 5-4: The image of PECVD machine in SNC 94

Figure 5-5: (a) Top view of the etch cavity shape for the rectangular mask windows; (b) SEM top view of the fabricated parallelogram mould [137].....99

Figure 5-6: Silicon etch rate in KOH vs. Temperature and Concentration (left) Silicon etch rate as a function of temperature at fixed concentration of 40% (right) Silicon etch rate as a function of concentration at fixed temperature of 60 °C [138] 100

Figure 5-7: Dependence of PDMS layer thickness for PDMS ferroelectret as a function of spin coating speed for a 5 min spin coating time (left) and as a function of spin-coating time for two given spin-coating speeds (right) [139].....101

Figure 5-8: The image of PDMS membrane 101

Figure 5-9: The image of the cross section image for fabricated (a) rectangular void and (b) parallelogram void PDMS ferroelectret membrane 103

Figure 5-10: The image of the cross section image for multilayer PDMS ferroelectret (a) rectangular PDMS ferroelectret (b) parallelogram void PDMS ferroelectret 104

Figure 5-11: The measured piezoelectric coefficient varying with the thickness ratio for one void layer PDMS ferroelectret 105

Figure 5-12: The measured piezoelectric coefficient varying with the thickness ratio for two void layers PDMS ferroelectret.....106

Figure 5-13: The measured piezoelectric coefficient varying with the thickness ratio for three void layers PDMS ferroelectret.....106

Figure 5-14: The measured piezoelectric coefficient varying with the number of void layers ..107

Figure 5-15: Measured piezoelectric coefficients of three PDMS structure over a month period.....108

Figure 5-16: Waveform of applied compressive force at slow walking mode.....110

Figure 5-17: Waveform of applied compressive force at normal walking mode 110

Figure 5-18: Waveform of applied compressive force at fast walking mode 111

Figure 5-19: Output voltage of PDMS ferroelectret at the optimal resistance of 65 MΩ 111

Figure 5-20: The characteristic *I-V* curves of a four layers PDMS ferroelectret 112

Figure 5-21: Instantaneous power output at different resistance loadings 113

Figure 5-22: Peak output voltage at different applied compressive forces 114

Figure 5-23: Output voltage pulse for three different walking mode under a constant force of 800 N 115

Figure 6-1: A simplified mode for charge implanted PDMS-ADP/PVA composites ferroelectret 119

Figure 6-2: Dielectric permittivity of ADP/PVA composites as a function of volume fraction, measured at 1000 Hz and at room temperature [135] 121

Figure 6-3: Schematic of PDMS-ADP/PVA composites ferroelectret fabrication processes 123

Figure 6-4: The surface potential as function of time for PDMS film with a thin layer of ADP/PVA composite and pure PDMS film at room temperature 124

Figure 6-5: Piezoelectric coefficient d_{33} decay for 72 hours 126

Figure 6-6: The long term measurement of piezoelectric coefficient at room temperature 126

Figure 6-7: Measured voltage output pulse for PDMS and PDMS-AVP/PVA composite ferroelectret 128

Figure 6-8: Measured voltage output for PDMS and PDMS-AVP/PVA composite ferroelectret at 72 hour after corona charging 128

Figure 6-9: The image of mechanical failure for PDMS-ADP/PVA composites ferroelectret 129

List of Tables

Table 2-1: Comparisons of different transduction mechanisms of kinetic energy harvesters.....17

Table 2-2: Comparison of piezoelectric coefficients of several piezoelectric materials [57] 21

Table 2-3: A summary of reported ferroelectret materials.....29

Table 2-4: Comparisons of different fabrication methods.....43

Table 2-5: Relative breakdown strength for some gas in corona charging 52

Table 4-1: The dimensions for the three designed structures.....75

Table 5-1: A summary of the duration of PECVD for different depth mould and the resulted depth.....95

Table 5-2: A summary main parameter for photolithography step 96

Table 5-3: A summary of main parameter for ICP etching.....97

Table 5-4: A summary of designed parameter for silicon mould.....102

Declaration of Authorship

I, Junjie Shi declare that the thesis entitled Ferroelectrets material in human body energy harvesting and the work presented in it are my own. I confirm that:

- This work was done wholly or mainly while in candidature for a research degree at this University;
- Where any part of this thesis has previously been submitted for a degree or any other qualification at this University or any other institution, this has been clearly stated;
- Where I have consulted the published work of others, this is always clearly attributed;
- Where I have quoted from the work of other, the source is always given. With the exception of such quotations, this thesis is entirely my own work;
- I have ackonowledged all main sources of help;
- Where the thesis is based on work done by myself jointly with other, I have made clear exactly what was done by others and what I have contributed myself;
- Parts of this work have been published as listed in section 1.4 of the thesis.

Signed:

Date:

Acknowledegments

I am deeply grateful to my advisors, Prof. Steve P. Beeby, Dr. Dibin Zhu and Dr. Zhenghua Luo, who have always supported and guided my research since the earliest stages of my work as MSc student at the University of Southampton. I would like to express my gratitude to my internal examiner Dr. Maurits de Planque.

I also really appreciate my PhD colleagues, for their support and their warm friendship. In particular, I wish thank Zhihao Li, Sheng Yong, Jingqi Liu, Zhao Zhang, Nhan C Truong, and Kantida Pancharoen.

No words can express my gratitude to my family, my wife, for their unbounded support and best wishes. It was never possible to do PhD without the warm support from my family.

Abbreviations

COC	Cyclic olefin copolymer
DRIE	Deep reactive-ion etching
FEP	Fluorinated ethylene-propylene
GDE	Gas Diffusion Expansion
MD	Machine direction
PC	Polycarbonate
PDMS	Polydimethylsiloxane
PEN	Polyethylene naphthalene
PET	Polyethylene terephthalate
PVDF	Polyvinylidene fluoride
PP	Polypropylene
PTFE	Polytetrafluoro ethylene
PZT	Lead zirconate titanate
RF	Electromagnetic
TD	Transverse direction

1 Introduction

1.1 Overview of the research

With the development in the field of wearable electronics systems, there is essential demand for supplying energy, more specifically from renewable energy sources, in different wearable electronic systems. Some applications require those systems to have a long lifespan. Using conventional batteries is not ideal because their need for periodic replacement. A sustained and reliable technology for energy supplying compared to conventional batteries must be considered. Energy harvesting technologies could potentially fulfil the needs of supplying electrical energy for powering these devices. Energy harvesting is the process of gathering energy from the human activity or the surrounding environment and converting it into electrical energy for powering information communication technology devices. Examples include distributed wireless sensor nodes for structural health monitoring, embedded and implanted sensor nodes for medical applications, recharging the batteries in large systems, monitoring tire pressure in automobiles, powering unmanned vehicles, and running security systems in household applications [1] [2].

For wearable electronic systems, the available energy sources generally consist of light energy, thermal energy and kinetic energy. Outdoor light energy has the capability of providing power density of 15000$\mu W/cm^3$ which is about two orders of magnitudes higher than other sources. However, indoor light energy has much lower power density in the range of 10-20$\mu W/cm^3$. In comparison, piezoelectric kinetic energy harvesting from human motion is the most attractive energy harvesting solution (5-8W) [1].

The popular approach to harvest kinetic energy is using piezoelectric materials such as piezoelectric polycrystalline ceramics, piezoelectric single crystal materials, piezoelectric and electrostrictive polymers and piezoelectric thin films. For the majority of applications, current research focuses on improving the properties of the synthesis of high energy density materials. Due to the large piezoelectric coefficients and relatively high energy output of

lead zirconate titanate (PZT), it has attracted the majority of attention in the literature [1] [2]. In particular, the piezoelectric vibration energy harvesting utilized PZT as the functional material, which present excellent dielectric and piezoelectric properties [1] [2]. Alternatively, piezoelectric polymers which have lower Young's modulus, such as polyvinylidene fluoride (PVDF) have been widely investigated for vibration energy harvesting [1] [2]. However, both PZT and PVDF are unsuitable for human body energy harvesting applications. PZT is physically hard and brittle and PVDF has low piezoelectric coefficients. The demand for energy harvesting systems in human body applications is increasing in the market and therefore a novel class of soft and compliant energy harvesting materials needs to be researched and developed.

Since the discovery of piezoelectricity in the late 19th century, its electromechanical properties have attracted a lot of researchers' attention. Research has been focused on the investigation of piezoelectric materials including crystalline and ceramic, and development of piezoelectric devices for various applications. Ferroelectricity, similar to piezoelectricity, is the electric charge that is permanently stored in a certain solid materials and can be released in response to applied mechanical stress. All ferroelectric materials are piezoelectric, but the main difference between them is that they exhibit a reversible, nonvolatile spontaneous electric dipole moment in the absence of an external electric field. At the end of 1960s, a strong piezoelectric effect was observed in β-phase polyvinylidene fluoride (PVDF) [3]. It was a great improvement for the applications of piezoelectric material that met the requirements for a flexible, lightweight, inexpensive material that can be easily fabricated on large scale [4].

In the late 1980s, the concept of the ferroelectricity was expanded into nonpolar polymer foams and this has recently gained more and more attention. Polymer foams are widely applied both in industry and in daily life. Compared with the non-cellular polymer films, these novel materials offer some significant advantages such as low density and low thermal conductivity which are especially good for food packaging, thermal and electrical insulation, and acoustic absorption applications [3]. One or more of appreciable properties of polymer foams are utilized in each of these applications. Combining their electric property and mechanical properties, electrically charged polymer foams can be used as sensors and

actuators by converting between electrical and mechanical energy. They are called ferroelectrets [6-8].

Electret is a dielectric material that has a quasi-permanent electric charge or dipole polarisation [5]. Ferroelectrets is a new class of electret material. An ideal ferroelectret usually consists of a cellular structure filled with gas. A permanent dipole moment formed by the positive and negative charges that are stored separately on the internal gas polymer interfaces. Due to the combination of the internal dipole moment and the anisotropic cellular polymer structure, the ferroelectret presents a strong piezoelectric effect [9-11]. For most ferroelectret applications, the two outside surfaces of the electrically charged polymer foams should be metallized to form electrodes. During the process of ferroelectret compression, to maintain the electrical neutrality of the whole foam, the electrical field in the voids is compensated by induced charges in the electrodes that are generated by the internal stored charges. Because of the lower elastic modulus of gas compared to the polymer bulk, it allows large deformation of the electrically charged voids when the polymer foam is compressed by a mechanical stress. In other words, the distance between the positive and negative charges decreases thus resulting in a change in the dipole moment and the amount of compensating charges. If the electrodes are short circuited, a current is generated. The anisotropic heterogeneous structure with low elastic stiffness is one essential key for the working principle of the ferroelectret. Ferroelectret materials exhibit a permanent spontaneous electric polarization that can be reversed by the application of an external electric field and hysteresis in response to an external electric field.

Since the discovery of ferroelectrets, their properties and applications have been intensively investigated [12] [13]. Ferroelectrets can be utilized as functional materials in electromechanical sensors and actuators and as electrically charged layers in electrostatic transducers. Their applications are mainly based on two modes: the electromechanical mode [14-18] and the electret mode of a classical electrostatic transducer [19]. For example, their typical application utilizing the electromechanical model and the electret model is microphones and loudspeakers, respectively. The principle of the electromechanical operation of ferroelectrets is to vary the thickness of the film while the mechanism of the electret operation is based on the movement of the film with respect to an air gap. Due to it

light weight and flexibility, polymer foams can be manufactured to any complicated shapes. Therefore it opens the possibility of embedding it with flexible electronic components to form a thin and flexible product, for example ferroelectret field effect transistor [20].

Among all ferroelectret material, polypropylene (PP) has been almost the only polymer that was investigated for ferroelectret applications. Hence, PP has become the main material of ferroelectret research and technology [21-24]. The basic preparation and further optimization of PP foams, as well as the resulting electromechanical properties of PP based ferroelectret transducers were extensively and sufficiently studied [10] [11]. Several research groups presented experimental and theoretical investigations on PP ferroelectrets that had large piezoelectric d_{33} coefficients up to some hundreds of pC/N which is comparable to those of PZT. PP ferroelectrets have already been developed into commercial products for different applications such as motion sensors, pressure sensors [11].

Piezoelectric properties of ferroelectrets strongly depend on the geometry of the cellular structure, i.e. the size and distribution of the voids. However, existing foaming techniques are usually poorly controlled in both individual void geometry and cellular structure. This usually impacts the resulting piezoelectric properties, limits the reproducibility of the material and also obstructs to further integration with common microsystems.

1.2 Objective and scope of the research

This work aims to develop and characterise new ferroelectrets with enhanced properties using microfabrication processes. It also targets to evaluate the novel ferroelectrets for use in energy harvesting applications. This research considers suitable materials for processing to form ferroelectrets. This project aims at enhancing piezoelectricity properties through optimising the void geometry of ferroelectrets and development of optimum microfabrication processes for fabricating optimised voids. This project also aims at focusing on the reliability and piezoelectric characteristics achieved for energy harvesting applications.

This work was partially funded by the Engineering and Physical Sciences Research Council as part of the SPHERE project (a Sensor Platform for Healthcare in a Residential

Environment). The goal of this project was to develop a sensor system for the home to diagnose and help manage health and wellbeing conditions.

1.3 Statement of novelty

The novelty in this work summed up as follows:

- Utilizing analytical model and ANSYS simulation to optimized the ferroelectret structure for achieving improved piezoelectricity properties
- Fabricating the optimized structure by MEMS fabrication
- Evaluating the performance of the fabricated ferroelectret in human body energy harvesting application

1.4 Publications generated from this thesis

Five publications have arisen from this work. The published articles are one journal paper and four conference papers. The publications are listed here in chronological order.

Shi J, Zhu D, Beeby S. P. An investigation of PDMS structures for optimized ferroelectret performance, *Journal of Physics: Conference Series*, Volume 557 conference 1

Shi J, Zhu D, Cao Z, and Beeby S.P. Optimization of a PDMS structure for energy harvesting under compressive forces, *Journal of Physics: Conference Series*, Volume 660 conference 1 2015

Shi J, Luo Z, Zhu D, Beeby SP, PDMS/PVA composite ferroelectret for improved energy harvesting performance, *Journal of Physics: Conference Series*, Volume 773. Conference 1 2016.

Shi J, Zhu D, Luo Z, Beeby SP, Optimization a structure of MEMS based PDMS ferroelectret, *Journal of Advanced Materials* (preparation)

Luo Z, Shi J, Beeby SP, Novel thick-foam ferroelectret with engineered voids for energy harvesting applications. *Journal of Physics Conference Series*, 773, (012030), 1-4.

1.5 Structure and content of this thesis

The thesis is structured as follows:

The state of the art ferroelectrets is reviewed in chapter 2. The chapter is divided into three main sections which review the energy harvesting, ferroelectrets, fabrication technologies and electrical charging, respectively.

Chapter 3 presents the ferroelectret structure model and the ANSYS simulation results for optimising the structures with variation of the void sizes and different void shapes. The chapter reveals the relationship between the piezoelectric properties of ferroelectret and its cellular structure.

Chapter 4 describes the 3D printed moulding fabrication process for PDMS ferroelectret with macro-size voids. The electromechanical testing which includes long-term piezoelectric coefficients measurement and energy harvesting performance testing for three different designs are presented. The comparison of practical results and simulation results is analysed.

Chapter 5 describes the silicon moulding fabrication process for PDMS ferroelectret with micro-size voids. The results of piezoelectric properties of structures with different void sizes, void shapes and void layers are presented. The energy harvesting performances of the fabricated sample are investigated.

Chapter 6 presents a method based on coating electret material on the void surface to improve the piezoelectric properties of ferroelectret. The principle as well as model of the method is presented. The piezoelectric properties and energy harvesting performance results are given.

Chapter 7 concludes this thesis with a summary of work, a discussion and recommendations for future work.

2 Literature Review

2.1 Introduction

This literature review aims to provide a background regarding human body energy harvesting techniques and ferroelectrets that are investigated in this thesis. This review includes ferroelectret properties and fabrication methods as well as looking at examples of the state of the art in human body energy harvesting applications.

2.2 Harvesting energy from human body

2.2.1 Overview of energy harvesting

Energy harvesting is the conversion of wasted or unused ambient energy into electrical energy. It is similar in principle to large-scale renewable energy generation such as solar and wind power. The most obvious difference is in scale. The unit of measurement for large scale power generation is megawatt, while the measurement unit of energy harvesting typical refers to microwatt or mill-watt. The goal of this technology is to provide remote power source for powering low power electronic devices [2].

The ambient surrounding is full of different types of energy. According to the types of energy sources, the available ambient energy sources can be generally classified into four types: light energy, kinetic energy, thermal energy and electromagnetic (RF) energy [2]. However, it is difficult to ascertain the universal energy source for energy harvesting technology. Each type of energy source has its own advantages and disadvantages. For example, harvesting solar energy can achieve relatively high power densities in good light conditions while it is unsuitable as a power source in poor light conditions. To harvest thermal energy, a temperature gradient is required but it is not always available especially around miniature devices. Depending on applications, each energy harvesting method should be evaluated to choose the best solution which harvests energy from one energy source only or from more energy sources collectively to power low power electronics.

Practical applications for energy harvesting are primarily limited by the feasibility of harvesters in individual cases. Such feasibility depends mainly on four factors: the typical power consumption of the device; the usage pattern; the device size (and thus the acceptable harvester size); and the environment to which the device is subjected.

Implantable or wearable devices will only significantly increase quality of life if they are unobtrusive to the patient [25], [26] in terms of both use and maintenance. It is especially important to eliminate maintenance for implantable devices, for which replacement of the power source in particular must be avoided or minimised [27]. While some implanted sensors can be totally passive and used in conjunction with active equipment when a measurement is needed [28], and some active devices could be powered up occasionally by wireless energy transfer, many require a continuous source of electrical power [29]. Ideally, all implantable medical devices would have a power-supply lasting as long as the required operational lifetime, thus reducing long-term operation and maintenance costs.

Traditionally, health care has concentrated upon short-term treatment rather than long term monitoring and prevention [30]. With the emergence of a larger number of chronic disease, health monitoring devices are attracting more attention. These devices will potentially require energy harvesting technology to achieve long life time. Normally, the health monitoring devices require being worn on human body for a relatively long-time. However, many chronically ill patients could have a significant increase in quality of life and expectancy if certain biological signs could be continually monitored and maintained during their daily lives. Three examples illustrate the potential of this approach: continually monitoring blood pressure in patients with hypertension can significantly increase medication compliance [31]; real-time processing of electrocardiograph traces can be very effective at revealing early stages of heart disease [32]; and closed-loop control of insulin administration for diabetic patients would significantly reduce the risk of hypoglycaemia [33]. Monitoring can also allow better targeting of medicines, reducing costs and unwanted side-effects. In order to achieve these benefits, many types of body-mounted or implanted medical devices are desired [29].

The biological processes that directly turn fat into electrical energy are difficult to achieve with existing available technology. However, indirectly harvesting energy from everyday human actions can be possibly realised. Products that operate in this mode have been on the market for many years such as hand winding torches and radios as well as self-powered watches. A few years ago, the concept of wearable technology was introduced based on aiming to incorporate computer and advanced electronic technologies with clothing and accessories and have gained more and more attention [34]. Although these electronic devices have been reduced in size to accommodate clothing, their power supplies, mainly batteries, are still bulky and not ideal due to their limited capacity, output current and the necessity of having an electrical outlet within easy access for recharging. Therefore, these problems could be alleviated by powerful, light weight and compact energy harvesting devices which collect energy from the human movement.

Power may be generated passively from breathing, body heat, blood pressure, arm motion, typing and walking or actively through user actions such as winding or pedalling. Each of the power sources has its own peculiar benefits and limits for different applications. A summary of the potential human power sources and the total power from various actions is presented in Figure 2-1 [34]. From this figure, it is shown that the most attractive energy sources on the human body are arm and foot motion. Therefore, kinetic energy harvesting is considered to be one of the best solution in wearable applications and thus is the key focus in this research.

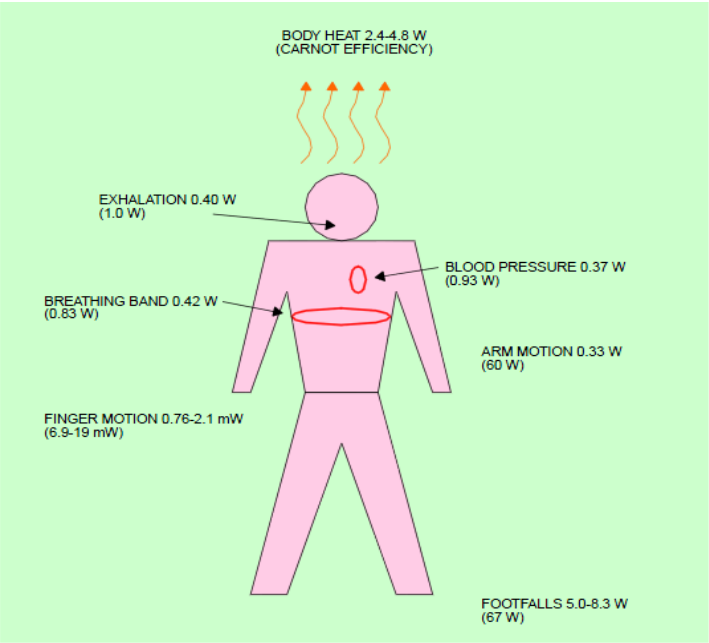

Figure 2-1: Total power from body driven sources for each action [34]

During the last decade, kinetic energy harvesting had received increasing attention since this sort of energy could be found almost everywhere; and a large number of kinetic energy harvesters for different applications had been reported [2]. These reported kinetic energy harvesters can be classified into three major types in terms of the transduction mechanisms: piezoelectric, electromagnetic and electrostatic.

A large number of research groups are currently active in the field of kinetic energy harvesting for wearable applications, and a wide range of devices and applications have been reported. The following sections will summarize reported kinetic energy harvesters based on the different transduction mechanisms mentioned above.

2.2.2 Electromagnetic generators

A typical electromagnetic harvester consists of a resonance mechanism, a permanent magnet and a coil. According to Faraday's law, a time variable magnetic field is produced by relative motive between the coil and the permanent magnet resulting in generating a voltage. Therefore, in order to maximize the amplitude of the relative motive and the magnetic field variation, the electromagnetic harvester operates in resonance conditions.

Goto has proposed a heart powered pacemaker that has been tested in vivo, as shown in Figure 2-2 [35]. It is consisted of a rotator gong, a magnet, a coil, a half wave rectifier and capacitor. The heartbeat move the rotator gong and a voltage generate on the fixed coil. The generated energy is stored in the capacitor. When the system was excited with sinusoidal input with amplitude of 40 mm at 2 Hz, the capacitor stored energy of 0.66 J after 30 minutes. In vivo test, the system was implanted on the wall of the right ventricle of a dog heart, 80 mJ energy was stored in the capacitor after 30 minutes testing.

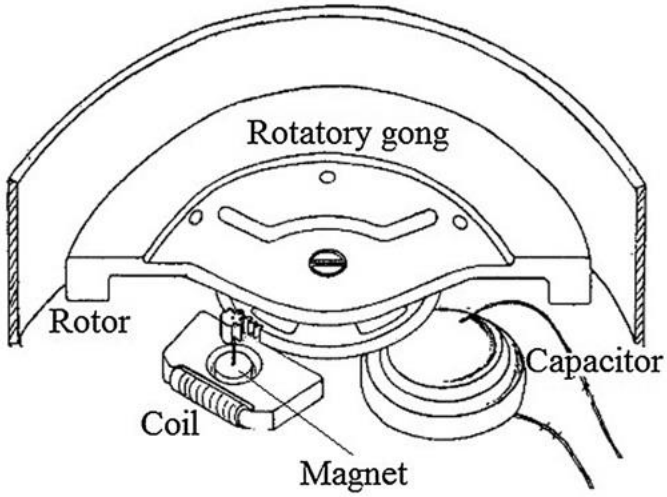

Figure 2-2: The schematic of electromagnetic harvester for pacemaker [35]

Morais has investigated an electromagnetic generator implantable in a hip prosthesis, as shown in Figure 2-3 [36]. The device consists of one or two external coils and a neodymium magnet is attached to a spring which is placed in Teflon tube. In order to avoid the collisions of the magnet against the bottom of the tube, a magnetic brake is place at the bottom of the tube. For a subject moving at a rate of 1.3 Hz and a 100 kΩ load, the device can generate a total energy of 1912.5 μJ after a charging period of 34.8 seconds.

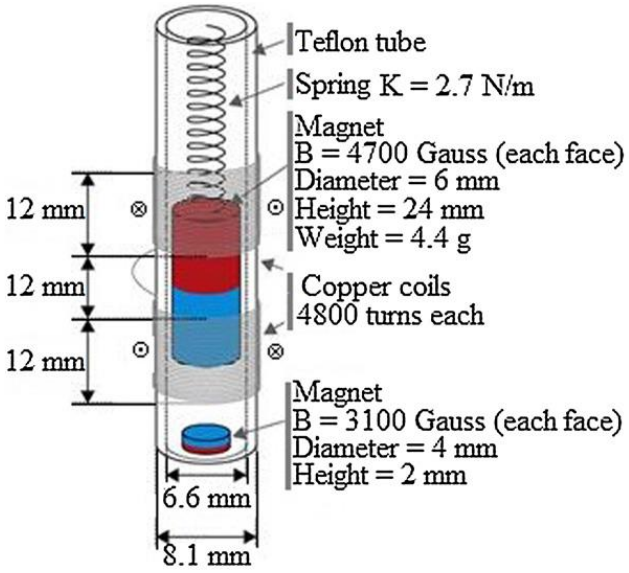

Figure 2-3: The schematic of the hip electromagnetic generator [36]

Luciano report an electromagnetic generator implantable in human total knee prosthesis in order to directly convert the knee movement energy into electrical energy, as shown in Figure 2-4 [37]. This harvester consists of six prismatic magnets placed in each condyle of the knee prosthesis and two copper coils placed between the condyles. The relative movement between tibia and femur produces a relative movement between coils and magnets and consequently generates a voltage on the coils. When the device was excited with a gait frequency of 1.02 Hz, the system produced total energy of about 22.1 µJ after a charging phase of 7 seconds.

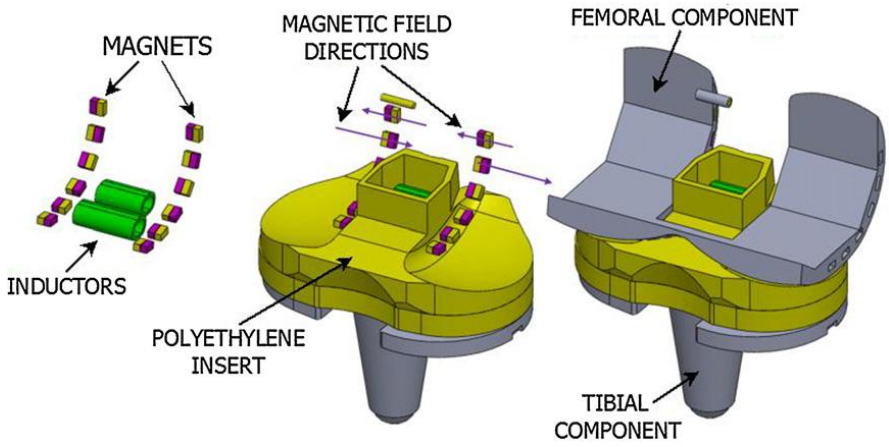

Figure 2-4: Structure of the generator for knee prosthesis [37]

2.2.3 Electrostatic generators

An electrostatic generator is based on a variable capacitor, whose plates are moved by human motion. When the capacitor is moved by the external human motion, a charge movement is generated. Electrostatic power harvesting systems can be built by MEMS technology which make it suitable for application inside the human body. A practical restriction of electrostatic generators is that require a precharge voltage in order to operate. This can be avoided by use of an electret which is dielectric material with a quasi-permanent electrical charge.

An electrostatic converter which is utilized to create an in vivo power supply for use with a cardiac pacemaker is described by Tashiro *et al*, as shown in Figure 2-5 [38].The variable capacitor is a honeycomb structure varying between 110 and 32 nF and attached to a circuit with two rectifiers: one supplying priming energy from a battery and one outputting the generated energy into a storage capacitor. When the generator, with a resonant frequency of 4.76 Hz and a proof mass of 640 g, is excited by a motion equivalent to that measured from the animal experiment, it produces 58 μW.

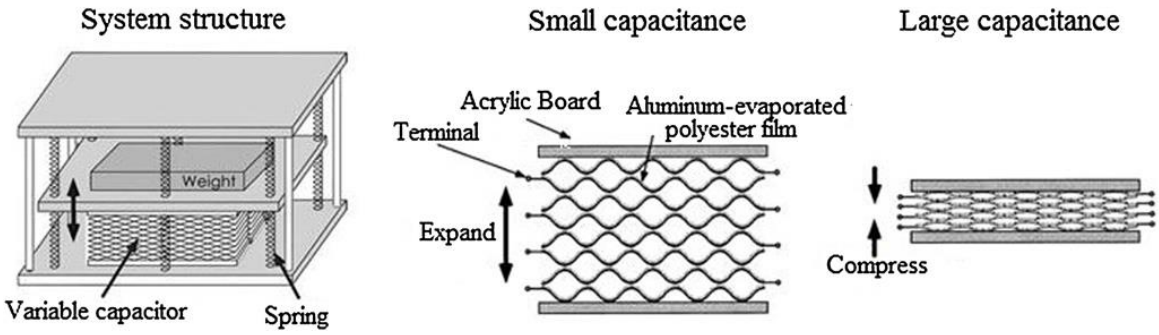

Figure 2-5: Honeycomb-type variable capacitor [38]

Naruse presented an electrostatic induction harvester which was based on the employment of micro ball bearing and an inter-digital electret structure, as shown in Figure 2-6 [39]. A long range movement at low frequency for device structure is achieved by the micro ball bearing. An electret is dielectric material with a quasi-permanent electrical charge and it is equivalent to a permanent magnet due to its electrostatic induction effect. The generator, which has a resonance frequency of 6 Hz, was tested on a shaker and generated an output power of 40 μW with a mechanical input of 2 Hz and 0.4 *g*.

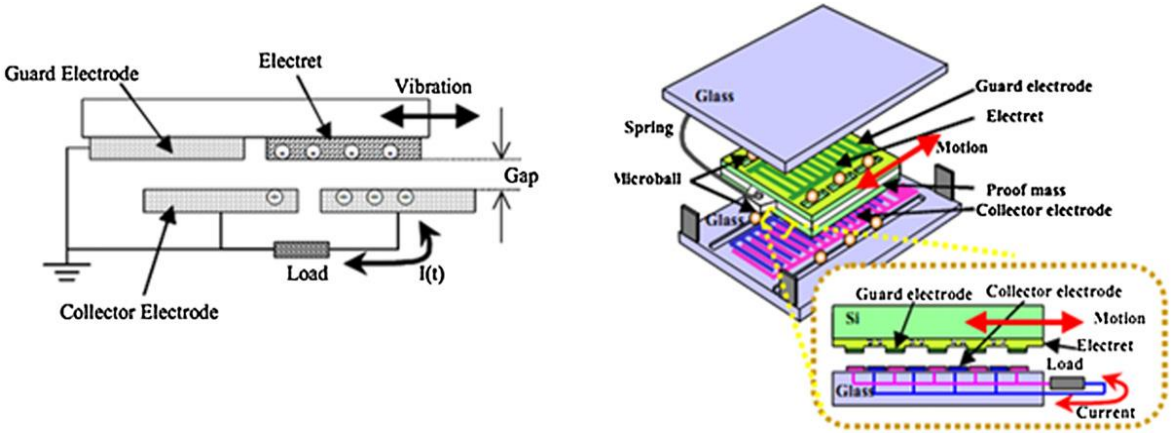

Figure 2-6: Schematic of electrostatic induction harvester using electret [39]

2.2.4 Piezoelectric generators

Piezoelectricity is material property whereby an electrical charge is accumulated in certain solid materials in response to applied mechanical stress. Piezoelectric generators utilize the piezoelectric effect to harvest energy from human motions. When an external force is applied on the piezoelectric material, some of the mechanical work done is stored as elastic strain energy, and some in the electric field associated with the induced polarization of the material. If an external conduction path through a load is provided, a current are generated.

The Massachusetts Institution of Technology (MIT) has investigated power harvesting from running shoes as a method of generating power for wearable electronics [39]. The researchers describe two types of generators: a piezoelectric bender placed in the sole, which flexes during the human gait; a unimorph attached to a curved steel plate, which flexes under the pressure of a heel strike, as shown in Figure 2-7. At a frequency of a footfall of 0.9 Hz, the piezoelectric sole and heel generators produce an average power of 1.3 mW into a 250 kΩ load and 8.4 mW into a 500 kΩ load, respectively.

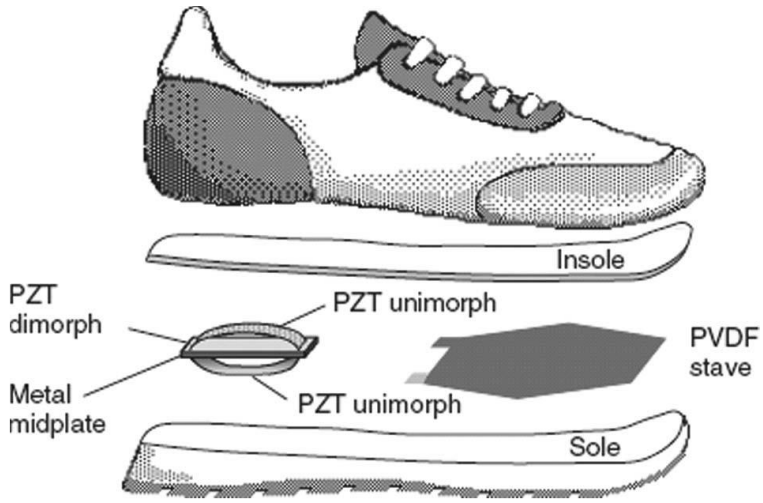

Figure 2-7: Energy harvesting shoe [41]

A type of impact coupled piezoelectric generator has been described by Renaud et al, as shown in Figure 2-8 [42]. The principle of this generator is the sliding mass strikes steel/PZT cantilevers located at each end of the frame for harvesting energy from impact forces. The theoretic results predict that the harvester can produce up to 40 μW power.

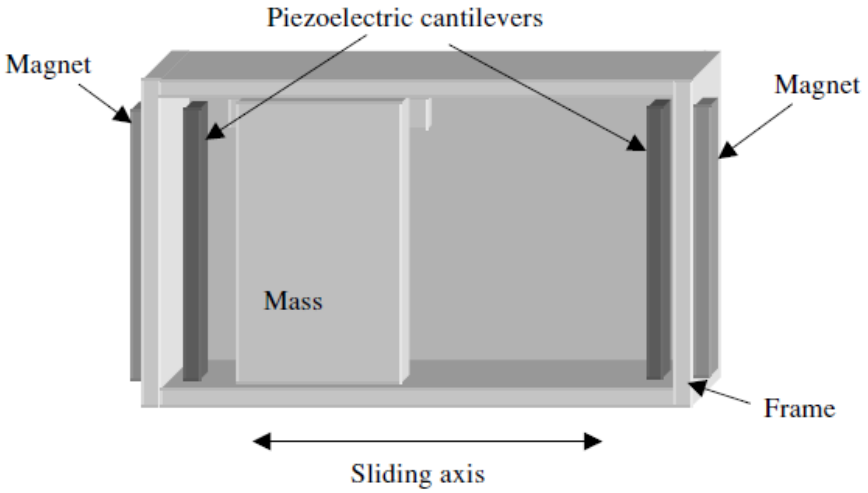

Figure 2-8: Impact coupled piezoelectric generator [42]

Elvin *et al.* report a self-powered strain sensor for application in human health monitoring [43]. A piezoelectric material which was attached to a four-point bending beam flexed by a sinusoidal force charges a reservoir capacitor through a half bridge rectifier, and an RF transmitter attached to the reservoir transmits a signal every time the voltage reaches a

threshold. Consequently, the time between transmissions decreases as the piezoelectric material is subject to higher forces and higher frequency deflections, so that the time between transmissions provides a measurement of strain.

In 2014, Shukla reported a novel piezoelectric harvester using a pendulum to receive kinetic energy from walking and jogging then converting it into electrical energy [44]. The assembly and exploded view of pendulum excited piezoelectric harvester is shown in Figure 2-9. The piezoelectric material (PVDF) was mounted on the periphery of the stator. Multiple strikers were mounted around the periphery of the rotor pendulum. When the rotor pendulum excited at frequency of 2 Hz, the maximum power obtained across the full wave rectifier and 2 MΩ optimum load resistance was nearly 290 μW. The efficiency of this harvester can be further improved by replacing PVDF with some higher performance piezoelectric material.

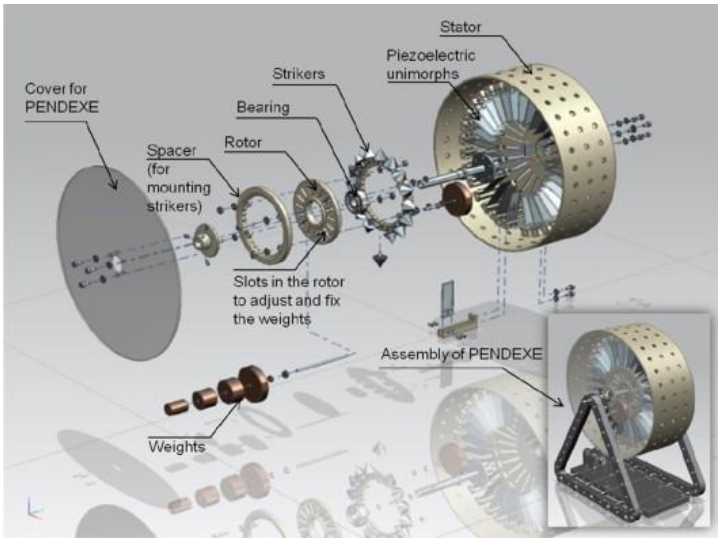

Figure 2-9: Assembly and exploded view of pendulum excited piezoelectric harvester [44]

In summary, comparing with three different harvesters, the piezoelectric harvesters seem the most promising in human body energy harvesting because the value of power produced is greatest. Their respective advantages and disadvantages are summarized in Table 2-1. Piezoelectric generators are the simplest type of generator to fabricate and therefore most suitable for human body energy harvesting applications. The output energy of electrostatic generator is usually lower than other two types of generators. In addition, the electrostatic harvests require complex electromechanical conversion structure and electronics. For human

body application, the energy harvesting devices must be limited in size, typically about 1 cm^3. The electromagnetic generators are typically larger than other two types of devices (more than 1 cm^3).

Table 2-1: Comparisons of different transduction mechanisms of kinetic energy harvesters

Type	Advantages	Disadvantages
Electromagnetic	• No external power source required • No mechanical constraints required • High output current	• Difficult to integrate with MEMS • Poor performance in micro-scale • Low output voltage
Electrostatic	• Easy to integrate with MEMS • High output voltage	• Mechanical constraints required • External power source or pre-charged electret required • Low output current
Piezoelectric	• Compatible with MEMS • High output voltage • No mechanical constraints required • No external power source required	• High output impedance • Low output current • Poor mechanical properties

2.2.5 Discussion

A number of studies have proposed methods to harvest energy from human movements. Human motion is characterized by large amplitude moments (1***g***) at low frequencies (<10 Hz). There are three main approaches that can be used to implement a human kinetic-powered generator. Each of the technologies has their own advantages and disadvantages. A simplest wearable piezoelectric generator would be to use piezoelectric materials on the

clothing that would generate charge from the movement of the user. There are two common industrial piezoelectric materials in the market: lead zirconate titanate (PZT) and polyvinylidene fluoride (PVDF). PZT is a ceramic perovskite material that has spontaneously dipole moment, the direction of which can be aligned and reversed in the presence of an electric field. The material features an extremely large relative dielectric constant about 1700. For PZT with 54 % zirconate and 46 % titanate, piezoelectric coefficients in the range from 155 to 590 pC/N have been reported [44]. However, PZT is not suitable for energy harvesting from human body because it would take an extremely large force to compress the material by a small amount due to its large elastic modulus. Since energy is defined as force by distance, the effective energy generated through human powered compression of PZT would be small. In addition, PZT is very brittle and can be broken when subject to large stresses which are common in human movement.

By contrast, PVDF is very flexible. PVDF is a highly non-reactive and pure thermoplastic fluoropolymer produced by the polymerization of vinylidene difluoride [45]. It is a transparent solid insoluble in water with an amorphous density of 1.74 g/cm^3 and a crystalline density of 2.00 g/cm^3 at 25 °C. Its melting point is about 160 °C and the glass transition temperature is about -38 °C [6]. However, PVDF exhibits a piezoelectric coefficient d_{33} of only 20 pC/N, which is significantly lower than that for PZT. The effective energy generated can be increased with increasing of the number of plies used. However, it results in degrading efficiency of the material. Therefore, in order to achieve high effective energy generated from human body, a more flexible, much lighter and highly piezoelectric material must be developed.

2.3 Ferroelectrets

2.3.1 Piezoelectric properties of ferroelectrets

Piezoelectricity is used to describe the ability of certain materials to generate electric charge when subjected to mechanical stress. In 1880, the first piezoelectricity in materials was discovered by Pierre and Jacque Curie [46-47]. Piezoelectric materials are able to convert electric field into mechanical displacement and vice versa. The piezoelectric coefficients

such as d_{33} d_{31} are used to measure this property. Their values are measured with the unit of pC/N.

The typical piezoelectric materials include crystals such as quartz, topaz and certain ceramics, and biological materials such as bone, DNA (Deoxyribonucleic acid) and various proteins [48]. In 1969, the first ferroelectric polymer material polyvinylidene fluoride (PVDF) was discovered by Kawai [49]. In the 1980s, Kirjavainen and his co-workers discovered that charged cellular polypropylene (PP) films present a strong piezoelectric coefficient [50-51]. They applied a high voltage to the cellular structure, which generated internal dielectric barrier micro discharge. Due to this phenomenon, the generated charges were stored on the internal surface of the voids to create electric dipoles resulting in piezoelectric-like properties. In addition, the cellular polymers show a ferroelectric-like behaviour by the presence of an external electric field [52-54]. This new group of materials is categorized as ferroelectret or piezoelectret materials.

Ferroelectrets are thin film of polymer foams exhibiting piezoelectric-like properties after electric charging. Ferroelectret films usually consist of a cellular structure filled with air. The voids in ferroelectret are lens shaped with a dozen microns in the thickness direction and a few dozen microns in transverse direction. During the electric charging, the positive and negative charges are generated, and separately trapped on the upper and lower gas polymer interface of the voids. A macroscopic dipoles moment is formed by the separated charges resulting in piezoelectric-like property of ferroelectrets. The macroscopic dipole moment is determined by two factors: the amount of charge and the distance between the separated charges. During the process of ferroelectret compression, the dipole moment of ferroelectret is reduced with its thickness decreasing; and the electrical field in the internal voids is compensated by induced charge in the metal electrodes which are generated by the internal stored charges. However, the mechanism of piezoelectricity is totally different between the ferroelectrets and the ferroelectric polymer, such as β-PVDF. For ferroelectrets, the structure of the ferroelectret is much more compressible than the bulk polymer material, so the volume inside the voids can be readily deformed, and the distance between positive and negative charges would be decreased. In other words, the dipole moment decreases. Although the dipole density would be increased due to the decrease of the whole volume,

the level of the increase in dipole density is much less than that of decrease in the dipole moment. Thus the amount of compensating charges decreases and a flow of charge is generated. For β-PVDF, the mechanism of dipole is defined as from fluorine atom (negative charge) to hydrogen atom (positive charge) [55]. The distance between the charges, which is in the magnitude of nanometers, can be considered constant while the film is compressed. In other words, the dipole moment stays constant while the volume of film decreases. The dipole density increases with the decrease of volume resulting in more compensating charges and a flow of charge is generated.

Ferroelectrets can exhibit a large piezoelectric d_{33} coefficient because of the low elastic coefficient in the thickness direction. The unusual softness and high compressibility is also important advantage of cellular ferroelectret polymers. Elastic properties of various materials are presented in Figure 2-10 which is called Ashby material property chart [56]. From this figure, anisotropic cellular polymers have low elastic modulus as well as low densities. Comparing with traditional flexible piezoelectrics such as PVDF, the Young's modulus and density of the cellular ferroelectret polymers is about 1000 times and 2 times smaller, respectively. The piezoelectric coefficient is inversely proportional to the Young's modulus of the foam. Hence, in theory, the piezoelectric coefficient of cellular ferroelectret can achieve several times greater than those of conventional piezoelectric materials. However, they usually have a small value of piezoelectric coefficient d_{31} which relates the change to the length change in the transverse direction. This disadvantage limits their applications as it requires large deflections. Generally piezoelectric coefficient d_{33} is the only coefficient used to evaluate the piezoelectric properties of ferroelectrets [56].

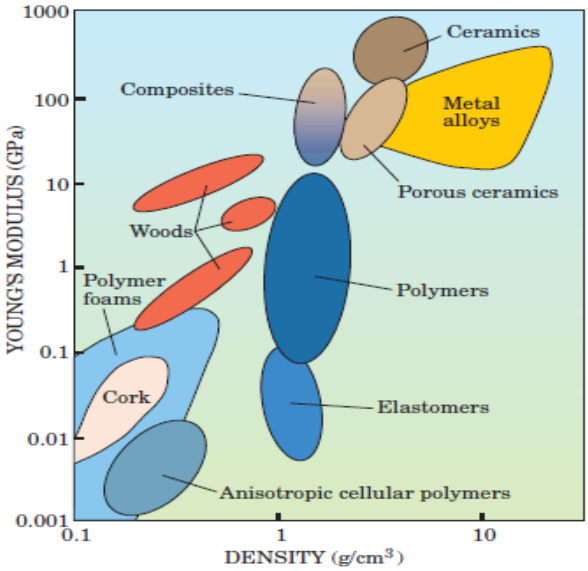

Figure 2-10: Ashby material property chart [56]

Comparing with traditional piezoelectric materials, the most outstanding property of ferroelectrets is their large piezoelectric d_{33} coefficients, as listed in table 2-1. The piezoelectric coefficient d_{33} of optimized cellular polypropylene (PP) can be up to around 600 pC/N. Compared with PZT, β-PVDF has the advantage of light weight; however, its piezoelectric coefficient d_{33} is only around 20 pC/N. Compared with PZT and PVDF, ferroelectret is advantageous for its flexibility and light weight.

Table 2-2: Comparison of piezoelectric coefficients of several piezoelectric materials [57]

Piezoelectric material	***d*$_{33}$ (pC/N)**
Crystal: Quartz (silicon dioxide)	2 (d_{11})
Ceramic: Lead zirconate titanate (PZT)	170-600
Ferroelectrics: β-phase polyvinylidene fluoride (β-PVDF)	20
Ferroelectret: optimized cellular polypropylene (PP)	600

For achieving high piezoelectric activity, the compressibility of ferroelectrets is an important property because the piezoelectric activity derives from the change of thickness by the external mechanical pressure. The cellular structural, elastic stiffness and some other factors

greatly affect the piezoelectric activity. There is an inverse-U-shaped relation between piezoelectric activity and the sample density in recent investigations, as shown in Figure 2-11 [58-59]. It shows the dependence of the piezoelectric response on the elastic stiffness and on the void structure. Ferroelectrets with small voids present low piezoelectric activity due to their high elastic stiffness. By expanding the voids, the void height is increased to a certain extent resulting in the lower elastic stiffness which can enhance the piezoelectric activity of ferroelectrets. While the void height reaches a certain level, meaning there are more spherical voids, the elastic stiffness increases instead of decreases, which causes the piezoelectric activity to decrease.

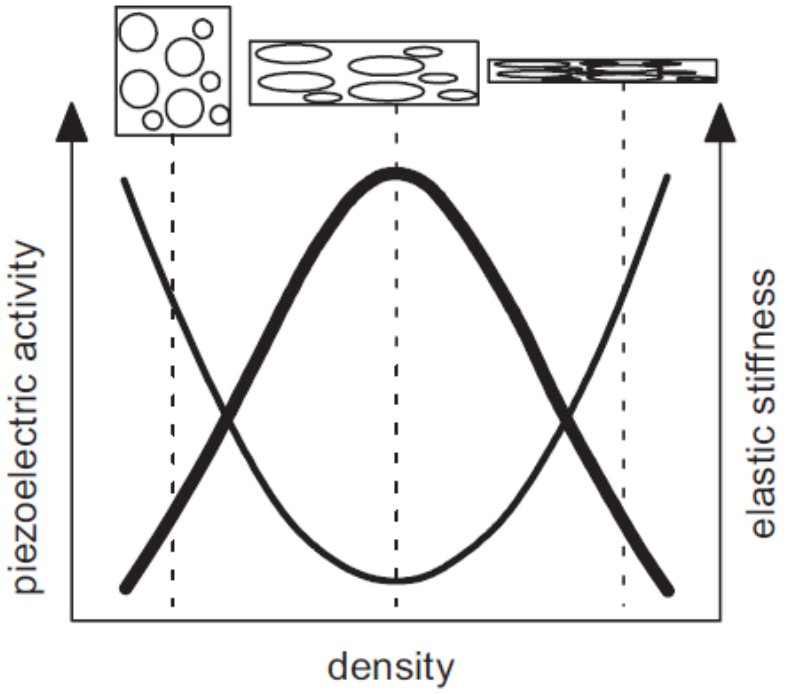

Figure 2-11: Dependence of piezoelectricity (thick line) and elastic stiffness (thin line) on the density and the corresponding void shape [58-59]

The stability of the ferroelectret is a key parameter which will determine whether it can be widely used. The stability of ferroelectrets is affected by two factors: the stability of the cellular structure and the stability of the charges trapped on the internal void surface because the dipole charges and the cellular structure collectively result in the piezoelectric effect. For applications of polymers, the constraint is always temperature. A cellular structure cannot

operate at temperature above its melting temperature. For charge stability, the melting temperature is much higher than the discharge temperature of polymer charges. Therefore, the operating temperature range for ferroelectrets is usually determined by the charge stability.

Charges are stored on the gas-polymer interfaces. However, these charges are not stable and will decay. The decay of ferroelectret can be classified two types: ohmic conduction and ion deposition. Ohimc conduction is an internal phenomenon. The charges are neutralized by positive or negative carriers, especially at high temperatures. The other decay mechanism is the compensation charges in the form of ions from the surrounding environment by the electrical field extending outside the ferroelectret [60]. The charge decay rate can also be influenced by many other factors such as: humidity, radiation and material. In a humid environment, charges decay faster due to the increase of charge carriers. In a radiation surrounding, the mobility of charges is improved resulting charge neutralization. In addition, in some special polymers, excellent charge stability only found for the negative charges [61].

In order to improve the stability of ferroelectret piezoelectricity, several methods were proposed. Several experiments have shown that, for most ferrolectrets, charge stability can be enhanced by charging at suitable elevated temperatures [62-65]. The reason of this phenomenon is that the charges can be located in different trap levels. At elevated temperatures, charges are mostly located in deeper trap levels, which are more stable than those located in shallow level. The overall thermal stability of the remaining charges is improved by this method. However, the shortcoming of this method is also very obvious: the elevated temperature reduces the final piezoelectricity due to the fact that the amount of charge stored in the polymer is reduced. Chemical treatments are usually used as the second method to improve the thermal stability of piezoelectric ferroelectret. An and his co-worker presented a cellular PP treated through chromic acid oxidation at 70-80 °C and then hydrofluoric acid treatment at the room temperature [66]. The modified sample presented twice piezoelectric coefficient d_{33} than the unmodified material after the 112 hours annealing at a given temperature [66].

2.3.2 Model

The piezoelectric behaviour of ferroelectrets has been theoretically analysed with a simplified model based on charged parallel polymeric and gaseous layers, including finite-element calculations [67-73]. Figure 2-12 shows the simplified model, where V is the DC voltage applied between the sample electrodes; σ_i is the charge density on the interface of the i_{th} layer; ε_1 and ε_2 are the permittivity of polymer bulk and gas; I_{1i}, E_{1i} and I_{2i}, E_{2i} is the thickness, electric field in the i^{th} polymer layer and gas layer, respectively.

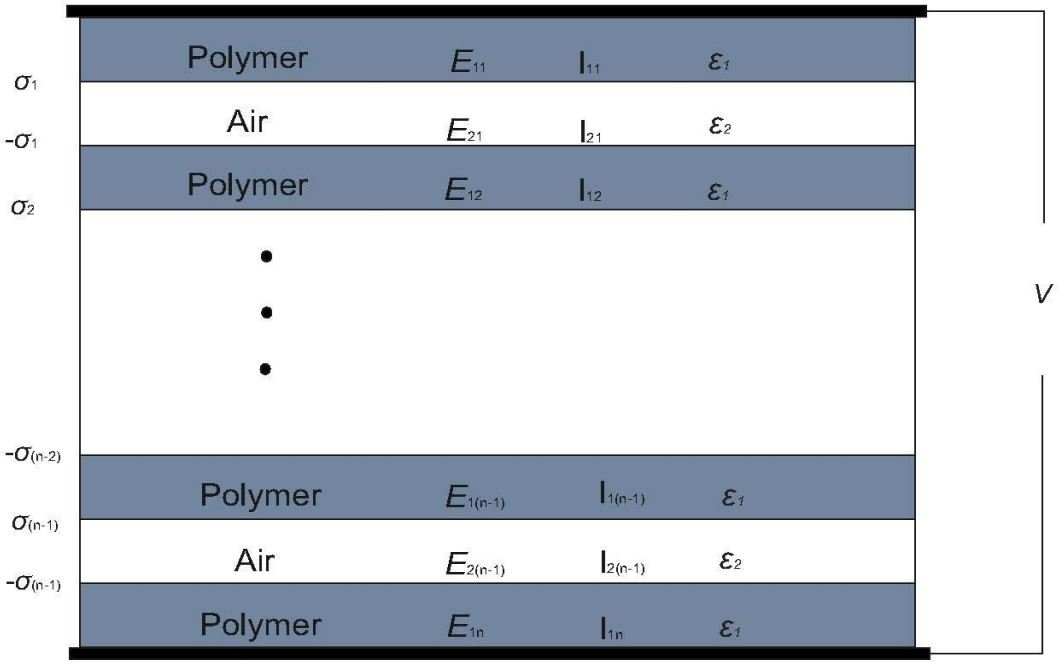

Figure 2-12: Simplified model based on charged parallel polymeric and gaseous layers

Based on the reference state of the multilayer model, when the voltage and the external pressure are very small, the piezoelectric d_{33} coefficient is obtained as [74]

$$d_{33} = \frac{\varepsilon_1 \varepsilon_2 L(\sigma L_1 + \varepsilon_1 V)}{Y(\varepsilon_2 L_1 + \varepsilon_1 L_2)^2} \qquad (2\text{-}1)$$

where L_1 and L_2 are the total thicknesses of the polymer and gas layers, respectively. $L = L_1 + L_2$ is equal to the polymer layer thickness. σ is the charge density of ferroelectret film.

If there is no static load applied on the ferroelectret, the electret charge density is the determining factor of the quasi-static piezoelectric coefficient d_{33}. The variation tendency of piezoelectric coefficient is varying with the electret charge density in the absence of external loads. From Figure 2-13, it can be seen that the piezoelectric coefficient is proportional to the electret charge density [74].

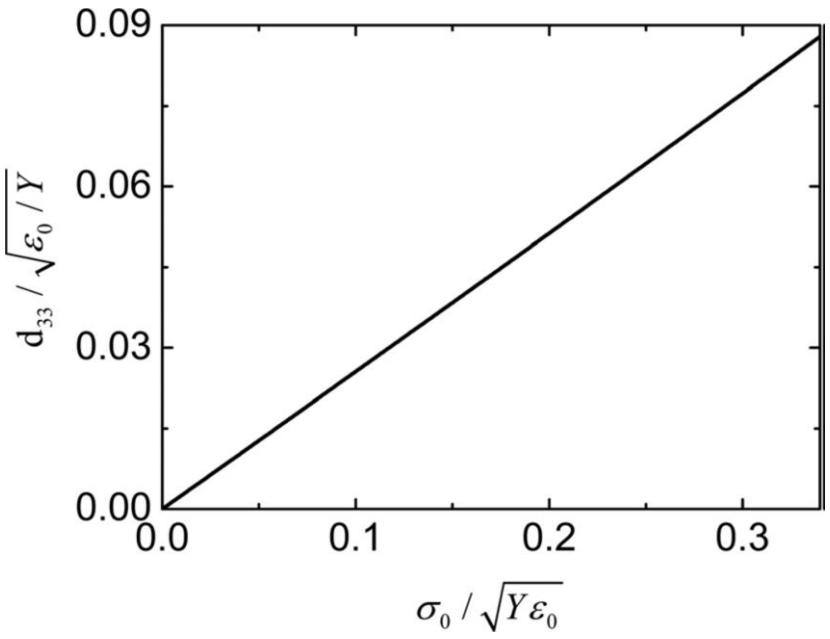

Figure 2-13: Piezoelectric coefficient as a function of the electret charge density in the absence of external loads [74]

When a static load is applied to the ferroelectret, the piezoelectric coefficient d_{33} now also depends on the external pressure because the void height is determined by the external force. The variation of d_{33} as a function of pressure is depicted in Figure 2-14. Compared with the case when no static loads are applied on the ferroelectret, the d_{33} can be improved by 10-30% with the normalized pressure [74].

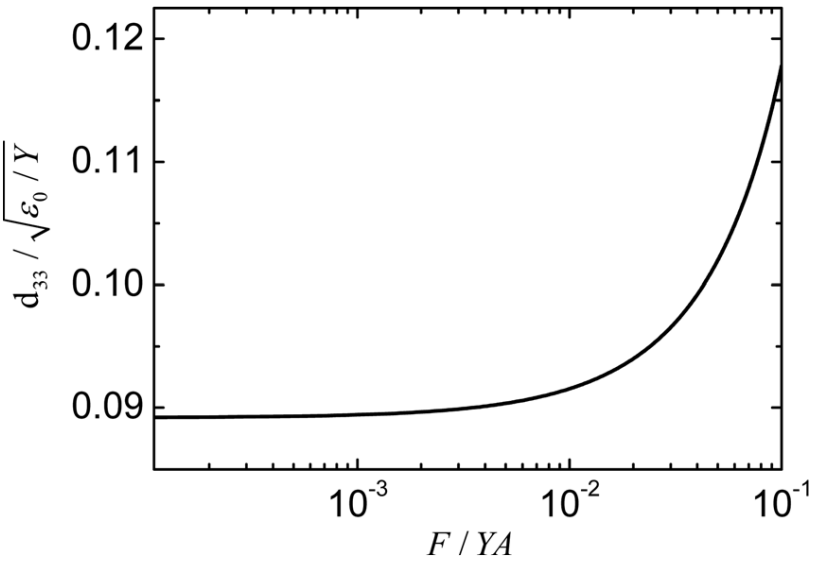

Figure 2-14: Piezoelectric coefficient as a function of the static pressure in the absence of external voltage [74]

2.3.3 Typical ferroelectret materials and applications

Polypropylene (PP) is an addition polymer made from the monomer propylene. PP has an amorphous density of 0.85 g/cm^3 and a crystalline density of 0.95 g/cm^3. It also has good fatigue resistance, which is an import piezoelectric material [52]. Due its dielectric properties, the charge can be trapped on the internal void surface after polarization. Hence, the development of piezoelectric cellular polymers started with PP [53]. Among a variety of ferroelectret materials, cellular PP is the most investigated material as a results of its outstanding properties such as large d_{33} coefficient, flexibility, as well as light-weight and low cost. The thickness of a cellular PP films is usually in the range of 50 to 100 µm with cells having a length of 100 µm and a height up to 10 µm [52]. Single cellular PP films were shown to have a good piezoelectric d_{33} coefficient up to 1200 pC/N [75]. This coefficient can increase up to 2010 pC/N for hybrid multilayer films [76-77]. In addition, it is unusually resistant to many chemicals, solvents, bases and acids. Due to the outstanding material properties, polypropylene foams, also known as PP foams, are the main ferroelectrets (material) that have been studied nowadays, and several industrial sensors and actuator products based on PP foams are already available on the market.

Recently, developments of cellular films made from polyethylene terephthalate (PET), polyethylene naphthalene (PEN), polytetrafluoro ethylene (PTFE) and cyclo-olefins polymers and copolymers were reported [78-85].

Polyethylene terephthalate (PET) is a thermoplastic polymer with a variety of applications including beverage and food containers, synthetic fibres and thermoforming applications. It can be synthesized by the esterification reaction between terephthalic acid and ethylene glycol or by a transesterification reaction between ethylene glycol and dimethyl terephthalate. Wegener *et al.* show that voided, stretched and inflated PET films charged with a corona-tip voltage of -60 kV show a d_{33} of about 23 pC/N with density of 0.67 g/cm^3 and elastic modulus of 7 MPa [86]. Although this value is much lower than that for charged cellular PP film, it is comparable to that of polar ferroelectric polymer such as PVDF. Moreover, PET is more thermally stable than PP [86]. In another investigation on the piezoelectric behaviour of PET, the cellular structure is obtained through a foaming process via supercritical CO_2 [87]. PET film charged with a corona-tip voltage of -60 kV showed a d_{33} of 500 pC/N with density of 0.96 g/cm^3 and elastic modulus of 0.3 MPa [87]. To achieve high piezoelectric activity, the elastic modulus of the PET can be reduced by inflation on supercritical CO_2.

Cyclic olefin copolymer (COC) is an amorphous polymer, which is produced by chain copolymerization of cyclic monomers such as cyclic monomer 2-norbonene with ethylene. From the recently report [88], COC films show a high piezoelectric coefficient d_{33} of 1000 pC/N, comparing with PP ferroelectrets, COC ferroelectrets present better thermal stability: the d_{33} reaches a stable values after polarization for 50 hours; the d_{33} maintains 70% of the initial values at 110 °C for 200 hours [88]. The reported COC ferroelectret consisted of five layers of COC films. Two of the five layers are patterned with 100 μm height rectangle channel arrays [88]. A summary of reported different materials are listed in table 2-2.

Comparing with other fluoropolymer, fluorinated ethylene-propylene copolymers (FEP) is characterized by excellent chemical resistance and high flame retardance combined with a very low smoke emission, outstanding ageing and weathering stability along with

appropriate mechanical properties. Because of its UV-stability, ferroelectrets made of FEP would also meet the needs of applications which have to resist environmental impact [102].

For ferroelectric polymers, numerous applications were suggested, demonstrated and commercially realised [61] [89]. The typical ferroelectric polymer such as PVDF were used in ultrasonic sensor for materials testing and in several medical applications. The application of ferroelectrets was developed much later than that of ferroelectric polymers because this new class of cellular materials was invented only 30 years ago. Owing to their lower stiffness and better piezoelectric properties, the ferroelectrets will usually be more suitable for these application areas than the traditional ferroelectric polymer. Various applications are proposed such as the monitoring of pressure distributions in shoe soles and the measurement of quantitative dynamic force on dog limbs [9]. Recently, a sleep monitor sensor based on ferroelectets has been developed as shown in Figure 2-15. The monitor senor is installed below a mattress, it responds to micro pressure changes caused by patient's heartbeat and respiration, and generates a reflective output voltage, by which the heart and respiration rates and movement activity can be calculated from the sensor signal.

Figure 2-15: The sleep monitor system based on ferroelectrets by Emfit [136]

Several prototypes of a floor sensor system based on ferroelectret have been constructed and tested in Finland. A typical system consists of several ferroelectret sensor and a signal processing unit which is used to analysed the recorded data for producing a desired alarm [91].

Table 2-3: A summary of reported ferroelectret materials

Material	**Year**	**Author**	**Piezoelectric Coefficient d_{33} pC/N**	**Young's modulus (MPa)**	**Thermal stability temperature**	**Charging voltage**
PP	2004	Wegener	300	1.3-1.7	60	
	2004	Wegener	590		60	24kV(30s)
	2005	Qiu	180	1-5.8	60	60kV(15s) 32kV(15s)
	2008	An	507 198(112hours)	1.4	70	25kV(30s)
PET	2005	Wegener	20	7	100	60kV(30s) 27kV(30s)
	2007	Fang	140		100	50kV
	2007	Wirges	500	0.3		60kV
	2010	Zhang	500	0.45-0.8	90	20kV(20s)
COC	2005	Saarimaki	15		110	60kV(60s)
	2007	Montanari	10		120	100kV/mm
	2013	Li	1000		120	5kV(10s)
PTFE&FEP	2007	Zhang	500-2200		90	32kV(60s)

	2009	Altafim	160		130	3kV(10mins)
	2012	Zhang	1000-3000	0.21	120	AC 1.5kV
PEN	2007	Fang	140		100	50kV(10s)
	2010	Fang	45	1.4	110	8kV

2.4 Ferroelectret fabrication technologies

According to the fabrication process and compositions, the polymer foams can be divided into two main cellular structures: homogeneous foams where a few voids are generated in a single film and heterogeneous multilayer foams where the voids are formed by a well-designed combination of polymer film layers and frames. For homogeneous foams and heterogeneous multilayer ferroelectrets, several manufacturing and processing techniques have been reported and demonstrated in the last two decades. Some typical structure preparation methods and optimizations are introduced in the following section.

2.4.1 Homogeneous ferroelectrets

2.4.1.1 Polypropylene foam

Among a variety of ferroelectret materials, cellular PP is the most investigated material as a result of its outstanding properties. The preparation technique of cellular PP is widely applied to manufacturing other cellular polymers. To achieve cellular structure, cellular PP foam can be generally produced by two common methods: foaming and stretching. The foaming method was firstly presented in late 1980s [92-93], a cellular structure was manufactured by a modified blow extrusion process. In the foaming method, the cellular PP structure is created by gas injection into the polymer melt. The polymer melt was extruded into a tube and cooled, and the tube was reheated and biaxially oriented by film blowing. The foamed voids are lens-like with typical diameters above 10 μm and thickness around 1

μm. After the initial foaming, to optimize the overall cellular structure, an additional Gas Diffusion Expansion (GDE) procedure was used to reform voids' size and shape [71] [94-97]. Cellular PP films were placed in a pressured vessel with N_2 at a high pressure (usually 20 bars). The internal voids would sufficiently expand during the fast pressure release to atmospheric pressure because the large pressure difference between the gas inside and outside the voids. Generally, commercially available cellular structure ferroelectret have a closed lens-like void. Dimension of these voids are usually $100 \times 100 \times 10$ μm^3, as shown in Figure 2-16.

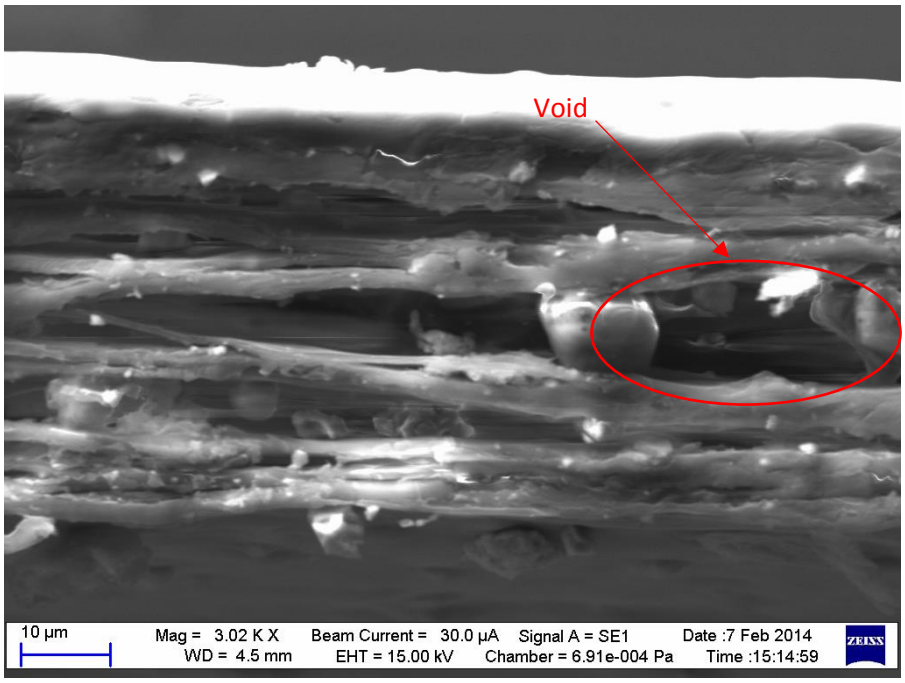

Figure 2-16: SEM photographs of cross sectional view of commercial PP film

In the stretching method, a cellular PP structure is produced by stretching due to the delamination at the interface of molten polymer and introduced solid particles [94-95]. Firstly, some suitable inorganic solid particles, such as titanium dioxide, hydrated magnesium silicate are mixed into the PP melt in an extruder and the polymer composite melt is extruded into films. Then, the polymer composite film is then stretched to generate void around the solid particles by delamination at their interface. Normally, the stretching process includes two parts: machine direction (MD) stretching and transverse direction (TD) stretching. These two types of stretching can be used at the same time or separately. The

needle shaped voids appears during the first stretching in the MD. After the second stretching in the TD, the voids' shape becomes flat and lens-like. The size, shape and distribution of the voids on the films are strongly influenced by the stretching parameters, such as temperature, stretching ratio and speed. In addition, the cellular structure is also affected by the type of the introduced solid particles.

2.4.1.2 Polyethylene terephthalate foam

PET foam is another polymer materials that has been successfully developed into ferroelectrets [98-99]. The physical principle of foaming method for polymer films is that the ability of gas molecules can penetrate into polymer film under high pressure. The carbon dioxide (CO_2) is well known as molecular fluid that can easily penetrate into the polymers. Figure 2-17 shows a phase diagram of CO_2 [100]. Above 31 °C and 72.9 bars, CO_2 behaves as a supercritical fluid and shows properties of both liquid and gas. The CO_2 gas has low viscosity thus can easily penetrate into small pores. To expand the internal voids in these polymers, the polymers can be soaked in supercritical carbon dioxide. For various supercritical CO_2 treatment, the size of the resulting voids is in the range of nanometres to micrometres. Besides CO_2, nitrogen (N_2) is the other alternative gas which can be used for foaming polymers. Because the N_2 molecule is smaller than CO_2, it results in the higher diffusion rate than CO_2. Hence, the resulting cellular structure from N_2 is more uniform.

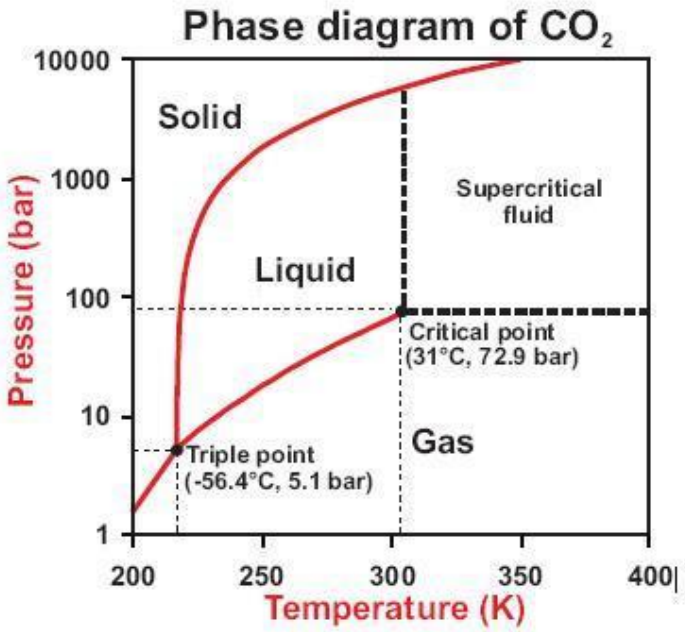

Figure 2-17: Phase diagram of CO_2 [100]

In an investigation on the piezoelectric behaviour of PET foams, the cellular PET structure was obtained through the combination of the foaming method via supercritical CO_2 and biaxial stretching method [98]. During the whole CO_2 foaming process, the temperature and pressure are the main controlling parameters. Firstly, a piece of commercial PET film was placed in a pressure chamber with a heating system. Then, the PET samples were soaked with supercritical CO_2 under 150 bars pressure. In the second step, after a rapid pressure release, the chamber was immediately heated up. Due to the sudden heating treatment, the transformation from supercritical CO_2 to gas state CO_2 leads to a large volume increasing inside the polymer. In other words, due to the large volume increased during the phase change, a large expansion of CO_2 inside the polymer occurs. After a supercritical CO_2 foaming process, a biaxial stretching process at elevated temperature was used to reform the size and shape of voids and the relative density of voids. After stretching, the height of void was decreased while the length of void was increased. The elastic stiffness of PET ferroelectret was also significantly reduced because some of the small polymer layers that existed in the voids had been destroyed by the stretching. In addition, the surface smoothness of PET foams has been improved in certain extent.

A second inflation process is used for a further structure optimization. In the first step, sample was placed in a pressured vessel with N_2 at a high pressure for a period of time. Then a rapid pressure release leads to the inflation of voids because of the large pressure difference. In order to stabilize the formed cellular structure, the sample immediately underwent a heat treatment. The cellular structure and void geometry can be controlled by varying the inflation parameters such as pressure, time and temperature.

2.4.1.3 Fluorinated ethylene-propylene (FEP) foam

Comparing with other polymer such as PP and PET, the higher manufacturing temperatures and the tendency to release hydrofluoric acid could lead to the more expensive and complex processes for manufacturing FEP ferroelectret. From a recent report [101], a two-step physical foaming process that consisted of a supercritical CO_2 saturation and a thermal voiding can successfully prepare cellular PET with appreciable piezoelectricity. Hence, this method is also applied to FEP. However, comparing with other polymers treated in this way, it is notable that the density reduction achieved for filled and unfilled FEP films is poor because the dissolved CO_2 diffuses out of the film at a very fast rate before the voiding step. The low porosity films that obtained by this method could be nearly non-piezoelectric [101]. In order to achieve a successful foaming of FEP, a new process was proposed [102]. In the fabrication method, the two step supercritical CO_2 foaming process was altered to a one step process. This new process performs the pressure release after the supercritical CO_2 saturation and the high temperature voiding at the same time inside an autoclave. Firstly, the FEP sample was heated to the final foaming temperature in an autoclave. Then, CO_2 was fed into the autoclave at the selected pressure. After the saturation, the applied pressure was released in a very short time. At the temperature higher than the melting point of FEP, the polymer is soft enough to be foamed by the fast volume expansion due to the phase change of the supercritical CO_2 to gas. Finally, a biaxially stretching at 120 °C was applied on the FEP foam to optimize the cellular structure.

2.4.2 Heterogeneous ferroelectrets

2.4.2.1 Template-based fabrication

Using fabrication techniques discussed above, dimensions of the generated microscopic cellular voids range from a few to dozens of micrometres. In addition, not only are the variable void size, but the amount of void is also sometimes distributed over a large range. However, it is still a challenge to achieve an ideal cellular structure by existing techniques. This drawback usually affects the final piezoelectric properties and restricts large-scale production in industry, where relatively uniform products with well controlled properties are required. Therefore, such disadvantage of existing preparation techniques can be improved by increasing the dimensions of the generated cellular void from microscopic to macroscopic. Due to the enlarged dimensions of the generated voids, a macroscopic cellular structure with uniform voids can be easily controlled.

In the past few years, a technique towards macroscopic cellular polymer systems was presented. The principle of this preparation method is utilizing a thermo-formed material to form cellular structure in sandwiched polymer films [71] [103] [104]. Therefore, voids are formed between the polymer films and dimensions of these voids are relatively large and almost uniform. After polarization, the layer systems exhibit relatively high piezoelectric coefficients due to a rather large dipole moment which is formed by the relatively large voids. The new preparation technique has been realized on fluoropolymer films with good thermal and long-term stabilities [71] [103] [104]. More recently, another new approach towards macroscopic cellular polymer system was presented [105]. The essence of this method is that a structure with well-defined uniform tubular channels is formed by a template-based fabrication process. It can serve as a material platform for several types of piezoelectric or even multifunctional ferroelectret films. The schematic of the laboratory fabrication process and the cross section at the end of the film are shown in Figure 2-18 [106]. The laboratory template consists of a Teflon PTFE film with parallel rectangular openings cut into the PTFE films by means of laser ablation. Before lamination, two Teflon FEP films are separately placed on the both sides of the PTFE template to form a sandwich structure. The three-layer fluoropolymer-film sandwich is fed into the lamination apparatus which has been preheated

to 300 °C. The lamination temperature is chosen in between the melting temperature of FEP and the melting point of PTFE. After cooling under ambient conditions in the laboratory, the two FEP layers are permanently melted to each other through the openings of the PTFE template. The PTFE template can be easily removed after cutting it open at one end due to the anti-adhesive properties of fluoropolymer. Therefore the resulting FEP-film system contains well-defined tubular channels. With this technique, it is possible to generate uniform channels with a wide range of widths, heights, and lengths, as well as arbitrary channel patterns. Due to the excellent thermal charge stability of FEP, the working temperature of this piezoelectric system is enhanced, comparing to the PP and PET foams.

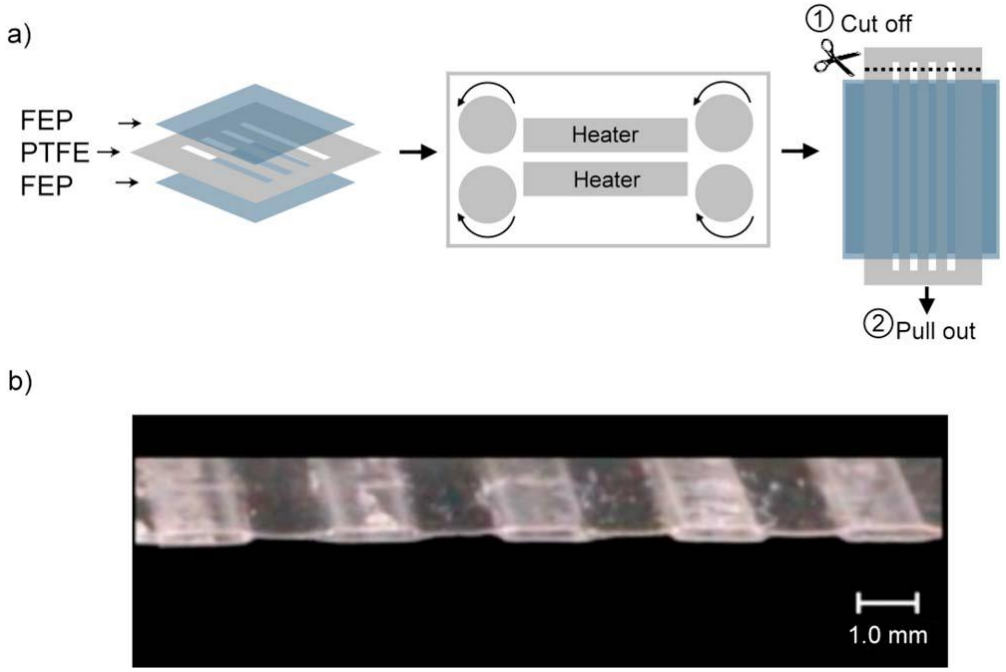

Figure 2-18: (a) Schematic of the laboratory fabrication process; (b) Optical micrograph of a typical ferroelectret system with tubular channels [105]

Recently, an improved process on the basis of template-based methods was proposed for preparing mechanically stable FEP ferroelectrets with highly regular, patterned microstructure and good bonding of the layers. Layered FEP ferroelectret films are prepared from sheets of FEP films by template-patterning following by a fusion-bonding process [106]. Figure 2-19 shows schematically the preparation of laminated film [107]. The templates are made of metal with regularly spaced, hexagonally arranged, circular recesses

obtained by drilling. In the patterning step, two film and one soft rubber pad are inserted in an alternating sequence and sandwiched between the two metal templates. The sandwich is hot pressed by a hydraulic press at an elevated temperature of 90 °C for 60 s. Then the soft rubber pad between the FEP layers is removed resulting in two film-template structures. In the following fusion bonding step, the two film templates structures are clamped and the whole assembly is placed in an oven and exposed to a temperature of 290 °C for 10 minutes. Before removing the templates, the assembly is removed from the oven and allowed to cool down to room temperature. Under the same fusion bonding conditions, a piece of flat FEP film is inserted between the two patterned FEP films to form a three layer sandwich structure. The surface and cross section scanning electron microscopy (SEM) image of the fabricated films are shown in Figure 2-20. With this technique, it is possible to prepare voided films with a variety of other polymers such as pure polytetrafluoroethylene (PTFE), PET and so on.

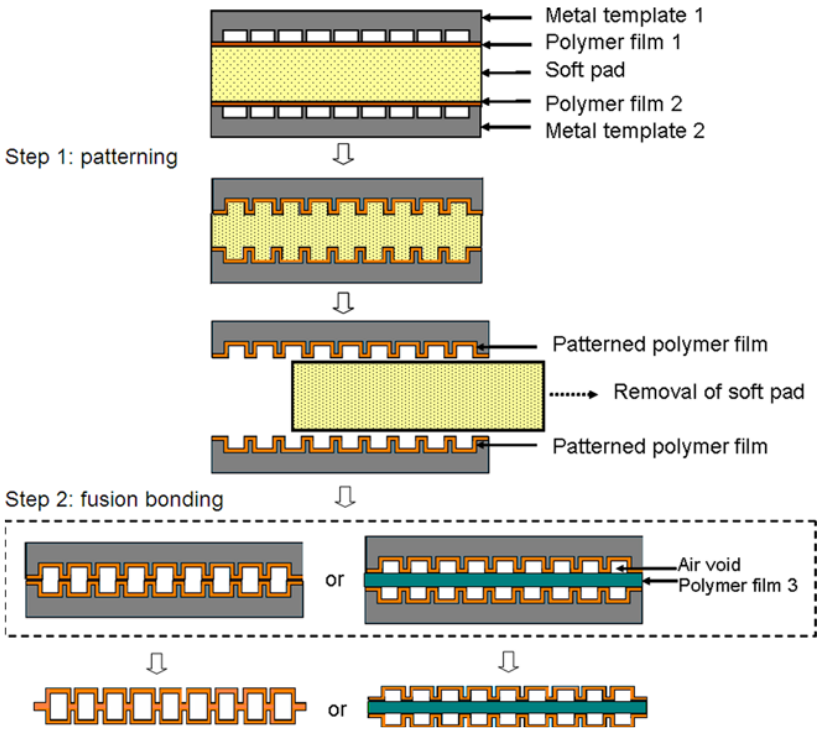

Figure 2-19: Schematic of preparation process of laminated films [107]

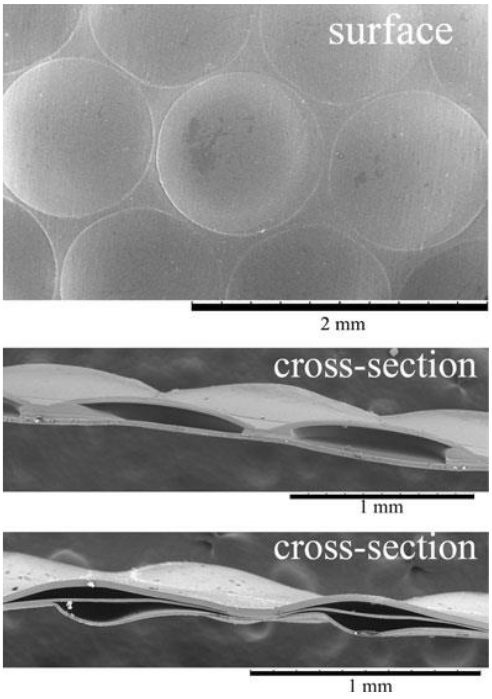

Figure 2-20: Scanning-electron microscopy images of the surface of a laminated film (upper part) and cross sections of laminated films (middle and bottom parts) [92]

2.4.2.2 Microfabrication

Comparing with using traditional fabrication techniques, the template based ferroelectrets have relatively uniform voids. However, the thickness of the whole film is increased due to the relatively larger voids, which will restrict its use for human body applications. If scaling down the desired void size, the desired individual void geometry can't achieved by the template based fabrication method. To address these fabrication issues, several publications have shown that MEMS fabrication processes are compatible with manufacturing cellular structure polymer.

Polydimethylsiloxane (PDMS) is the most widely used silicon based organic polymer. It belongs to a group of polymeric organosilicon compounds which are characterized by a siloxane backbone of silicon and oxygen atoms. In generally, PDMS is inexpensive, nontoxic, optically transparent and chemically stable. Because of its ease of fabrication, its applications range from contact lenses and medical devices to elastomers.

Recently, a new concept of piezoelectric polydimethylsiloxane (PDMS) films with micron-sized voids of cellular structures was presented [108]. In this method, a structure with well-defined uniform micron-sized voids is formed by means of a MEMS fabrication process. Figure 2-21 illustrates the fabrication process of the presented cellular piezoelectric PDMS films. Firstly, the mould used for duplicating the cellular microstructures is fabricated by a spin-coating process to pattern a layer of photoresist on top of a blank silicon wafer. After the photoresist mould is fully stabilized, to silanize photoresist surface for de-molding, the silicon wafer is placed in a desiccator under vacuum with a vial containing a few drops of 1H, 1H, 2H, 2H-perfluorooctyltrichlorosilane (Fluka). Then a thin PDMS mixture layer is deposited on top of the mould and is cured for 1 hour at 85 °C. Similarly with photoresist, the top surface of the cured PDMS layers is also treated by silanizing process. In order to transfer the surface-treated PDMS, on the top of the PDMS should be cast a thin layer of PDMS as a reusable transferring carrier. The PDMS structure is peeled off from the mould and transferred to a spin-cast blank PDMS layer. Before the bonding process, the surfaces of the two PDMS layers should be treated by a corona process to activate the surface for irreversible bonding. The corona treated surfaces are pressed together for at least 1 hour at 85 °C for bounding to take effect. While the bounding strength between native PDMS and silanized surfaces is lower than that between native PDMS surfaces, the transfer carrier can be separated from the cast PDMS layer which is bonded irreversibly with another structure layer. Two and more voids layers can be constructed by repeating the casting and bonding processes. The SEM micrographs of fabricated PDMS microstructures are shown in Figure 2-22. With this technique, the piezoelectricity of ferroelectret films can be tailored by adjusting the dimensions of the cellular structures. However, one severe issue of this fabrication process is that the life span of the implanted charges is only in the range of days to weeks.

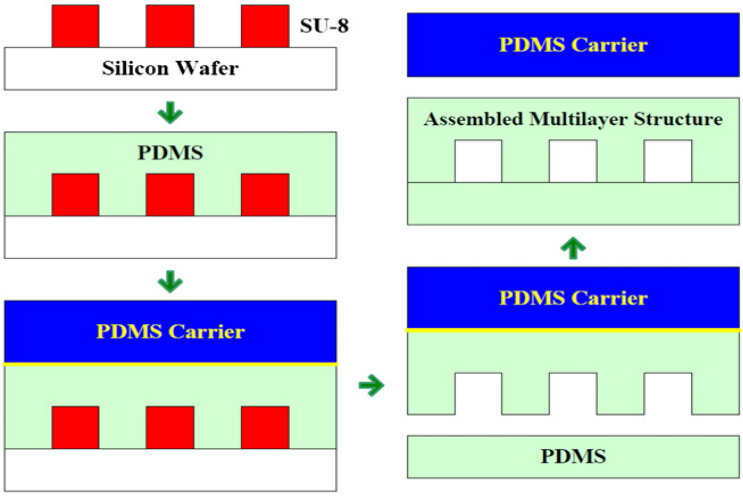

Figure 2-21: Schematic of fabrication process based on PDMS [108]

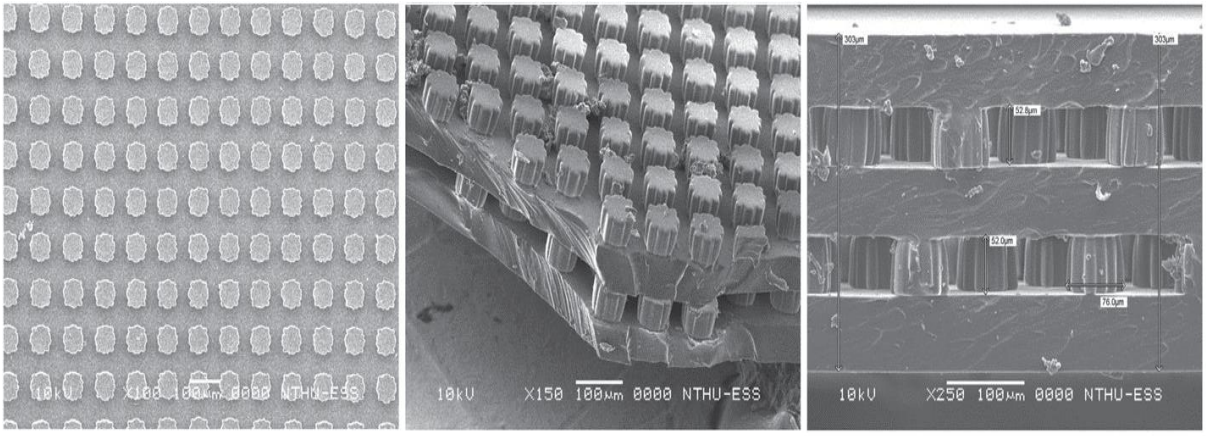

Figure 2-22: SEM photographs of top view, 3D view and cross sectional view of fabricated cellular PDMS microstructures [108]

A novel MEMS-based high density cellular piezoelectric parylene polymer with trench-filled structures was proposed in 2012 [109]. The MEMS fabrication process and the SEM image of the piezoelectret is shown in Figure 2-23. Firstly, silicon trenches are formed in 4-inch silicon wafer by deep reactive-ion etching (DRIE). Following a thermal oxidation process, a thin silicon dioxide (SiO_2) is generated as an eletric isolation layer. Then, the high-aspect-ratio trenches is introduced into 1 μm-thick fluorinated parylene and 18 μm-thick parylene-C for forming a closed polymer channel with 5 μm-wide void. After an etching process, the surface of parylene layer is opened by O_2 plasma. Then PEDOT droplet is

injected into the channel void. After flowing PEDOT through the closed parylene springs, the whole structure should be baked at 100 °C for 15 min. Finally, the structure is released from the silicon mould using XeF_2 etching.

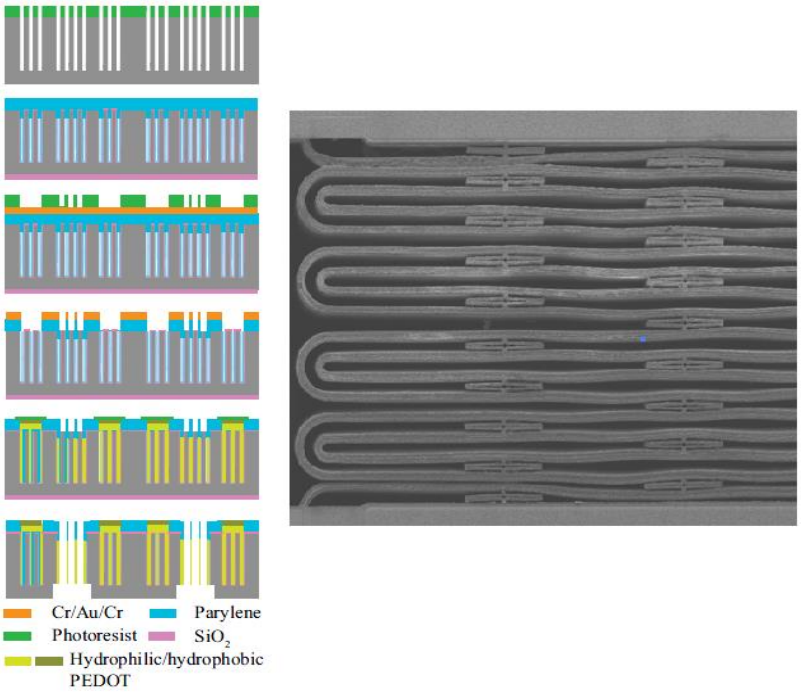

Figure 2-23: Schematic of fabrication process based on parylene and SEM image of parylene beams [109]

2.4.2.3 Screen printing

In 2013, screen printing technology that is widely used in the two dimensional patterning was introduced to the ferroelectrets preparing process [110]. A stable three layer polycarbonate (PC) ferroelectrets with well-defined voids was obtained by means of screen printing following by a heating and curing process. Figure 2-24 shows the schematic diagrams of the screen-printing process. In order to produce polymer-film systems with cavities that are suitable for bipolar electric charging, a tensioned screen is mounted onto a frame and permanently coated with a layer of ink-blocking stencil that provides open areas with the desired pattern for ink transfer. A screen printing paste is deposited through the screen with a predesigned pattern onto the surface of a polymer electret film by application of squeegee's pressure. Figure 2-24 (b) illustrates the pattern (the orange-colored) that was

deposited on the first PC film (dark grey substrate in the figure). Afterwards, the printed polymer ink was cured for 4.5 seconds by means of UV curing at 30 % of the available maximum intensity of 1800 mJ/cm^2. Figure 2-24 (c) illustrates a second layer of ink with essentially the same pattern (blue-colored) was printed on top of the cured first ink layer and the second PC film was placed on the freshly deposited pattern. The sandwich structure was then thermally annealed for 4 h in an oven at 110 °C. As a result of this process, two PC films are tightly bonded to each other by the polymer ink pattern between. A digital photograph of a sample fabricated by screen-printing process is shown in Figure 2-24 (d). As seen in the figure, the sizes of bubbles is relatively uniform and they are almost uniformly distributed within the ink pattern.

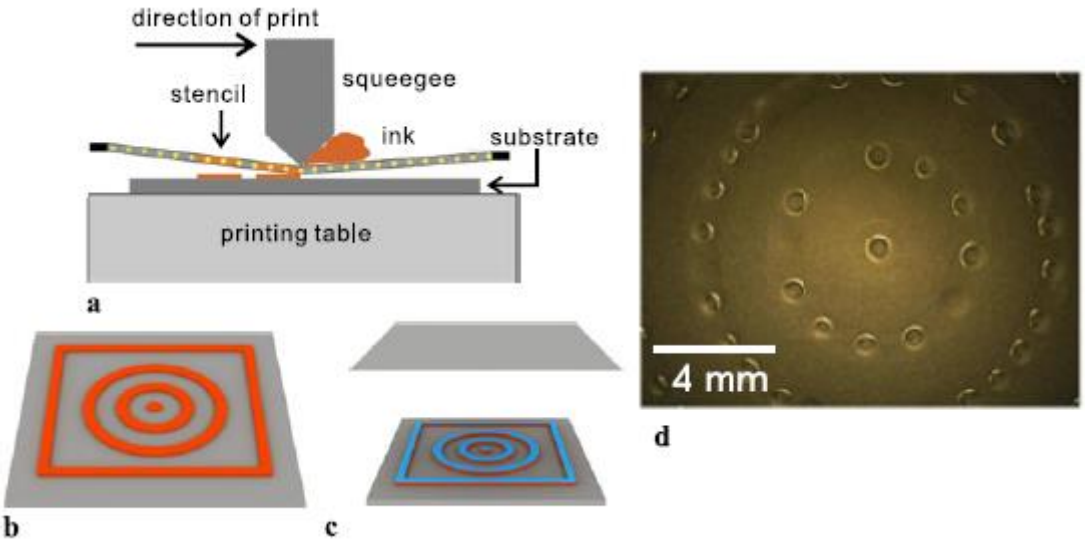

Figure 2-24: Schematic diagrams of the screen-printing process (a), and of the steps for manufacturing void-containing PC polymer systems ((b) and (c)). (d) Digital photographs of sample prepared by screen-printing process [110]

2.4.3 Discussion

A number of studies have proposed method to fabricate ferroelectret. There are four main techniques that can be used to fabricate ferroelectret: film blow and extrusion process, template-based process, MEMS process and screen printing process. Each of the technologies has their own advantage and disadvantages. A summary of their respective

advantages and disadvantages is shown in Table 2-4. Film blow and extrusion fabrication process is the most industrial production method. The deficiencies of this fabrication method are obvious including variable void sizes and irregular overall cellular structure. The final piezoelectric properties of ferroelectrets are usually affected by this drawback. Template based and screen printing fabrication methods generally resolve this problem by enabling a ferroelectret with relatively larger voids. However, the relatively larger voids will lead to the thick film. This problem will restrict it applied on human body applications. To fix these problems, MEMS fabrication method is ideal fabrication method. The fabricated ferroelectrets with smaller size voids have uniform void size and regular cellular structure.

Table 2-4: Comparisons of different fabrication methods

Fabrication method	Advantages	Disadvantages
Film blow and extrusion	• Suitable for mass manufacturing	• Irregular cellular structure and void size
Template-based	• Regular cellular structure • Uniform void size	• Relatively large voids
MEMS	• Regular cellular structure • Uniform void size in micro-scale	
Screen printing	• Regular cellular structure • Uniform void size	• Relatively large voids

2.5 Electrical charging for ferroelectret

2.5.1 Principle of ferroelectret charging

In order to achieve piezoelectricity properties, the fabricated ferroelectrets should be polarized at high electrical field. The polarization in ferroelectrets is generated by electrical

breakdown in voids and charge trapping their inner surfaces during charging at high electric fields. Paschen breakdown is known to be responsible for the internal charging of the void in ferroelectret material [111] [112]. Based on Paschen's law, the minimum required breakdown voltage to start a discharge between two electrodes in a gas can be calculated by:

$$V_{breakdown} = B \times \frac{(p \times d)}{\mathrm{C}+\ln(p \times d)} \quad (2\text{-}2)$$

$$E_{breakdown} = B \times \frac{p}{\mathrm{C}+\ln(p \times d)} \quad (2\text{-}3)$$

And

$$C = \ln\left(\frac{A}{\ln(1+\frac{1}{\gamma})}\right) \quad (2\text{-}4)$$

Where $V_{breakdown}$ and $E_{breakdown}$ are the minimum breakdown voltage and the minimum breakdown electrical field intensity, respectively; constants A and B depend upon the composition of the gas, and γ is the secondary ionization coefficient, p is the gas pressure, d is the gap distance of two electrodes.

When the voids filled by air, A = 11 $(\mathrm{mPa})^{-1}$, B = 273.8 $\mathrm{V}*(\mathrm{mPa})^{-1}$ and γ = 0.01. The breakdown voltage for air at 1 bar can be calculated. The variation of breakdown voltage with gap distances is shown in Figure 2-25. It can be found that the breakdown voltage decreases with the gap distance in the range of 0 to 10 μm and the minimum value achieved is about 350 V at about 15 μm. By contrast, the breakdown voltage increases with gap distance in the range of 15 to 200 μm. According to the formula (2-3), the variations of breakdown electric fields with the gap distances can also be calculated and is shown in Figure 2-26. At relatively small gap distance, the required breakdown field is extraordinary high and is difficult to achieve. Because electrons are much smaller, their average distance between colliding with other molecules is about 0.5 μm. If the electron is in an electric field of 15 MV/m, it will be accelerated and acquire 7.5 eV of energy in 0.5 μm of travel in the direction of the field. The required ionization energy needed to dislodge an electron from nitrogen molecule is about 15.6 eV. The accelerated electron will need more energy to ionize

a nitrogen molecule. It means that at smaller electrode gap, the required electric field is extraordinary high.

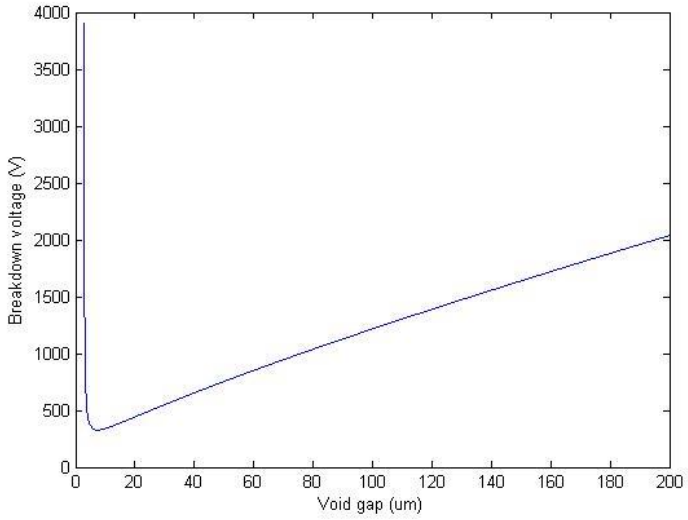

Figure 2-25: Breakdown voltage as a function of the gap distance in air at a pressure of 1 bar according to Paschen's law

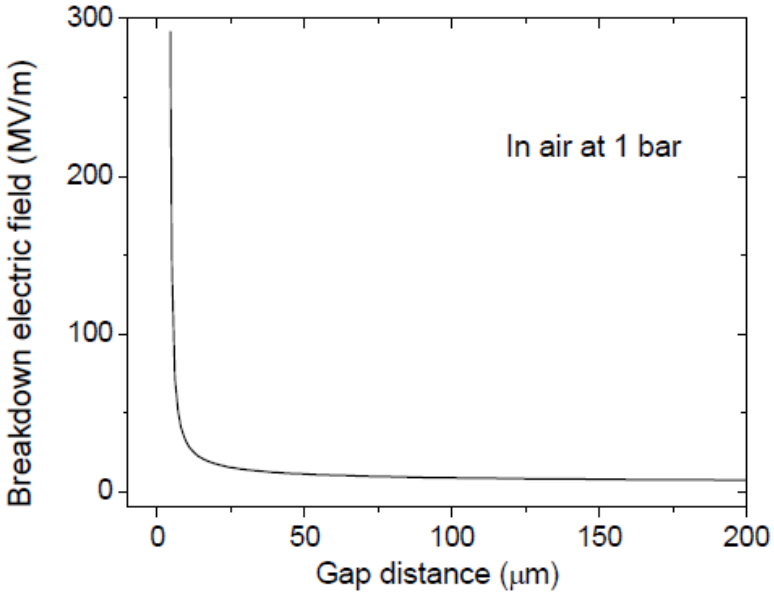

Figure 2-26: Breakdown electric field as a function of the gap distance in air at a pressure of 1 bar according to Paschen's law

In practical experiment, it is impossible to apply the high electric voltage directly applied to the internal voids and the voltage is normally applied on sample electrodes. Hence, in the contact charging method, the charging voltage is given by the following relation [112]:

$$V_{charging} = \frac{E_{breakdown}}{\frac{\varepsilon_2}{\varepsilon_1} s_1 + s_2} \quad (2\text{-}5)$$

Where ε_1, ε_2, S_1, and S_2 are the relative dielectric constant of the polymer and gas, equivalent thicknesses of the solid and void layers, respectively. For a certain ferroelectret, the required charging voltage can be estimated by equation 2-5.

2.5.2 Description of charging process

In order to present piezoelectric properties, cellular polymer should be polarized at a high electric field. Figure 2-27 schematically illustrates the charging process. For simplification, the whole cellular structure ferroelectret is replaced by the polymer film with one void. $V_{charing}$ is the applied charging voltage between the sample electrodes, E_{local}, $E_{void\text{-}int}$, $E_{void\text{-}ext}$ end $E_{breakdwon}$ are the actual electric field, the electric field from the internal deposited charges on void, the electric field from the external charges on the electrodes and the breakdown threshold electric field, respectively. When a voltage is applied to the sample, the actual electric field across the void is contributed by the external charges on the electrodes. Once the actual electric field is higher than the breakdown electric filed, an electric discharge will be triggered, and the generated positive and negative charges will be separately deposited on the void surface due to the influence of electric field (Figure 2-27 (a)). With the charge on the void accumulating to a certain extent, the actual field in the void would be compressed (Figure 2-27 (b)). The gas breakdown would stop until the actual field in the void is lower than the breakdown electric field (Figure 2-27 (c)). While the applied voltage is removed, if the actual field in the void is higher than the breakdown threshold, the electric breakdown still occurs, which will destroy some of the previously trapped charges until the field is once again less than the breakdown field [114-116]. At the same time, with the applied voltage removed, some induced charge is generated at the sample electrodes to

maintain the electric neutrality of the whole ferroelectret (Figure 2-27 (d)). The remaining charges are the final charges that can be trapped on the gas/polymer interfaces (Figure 2-27 (e)).

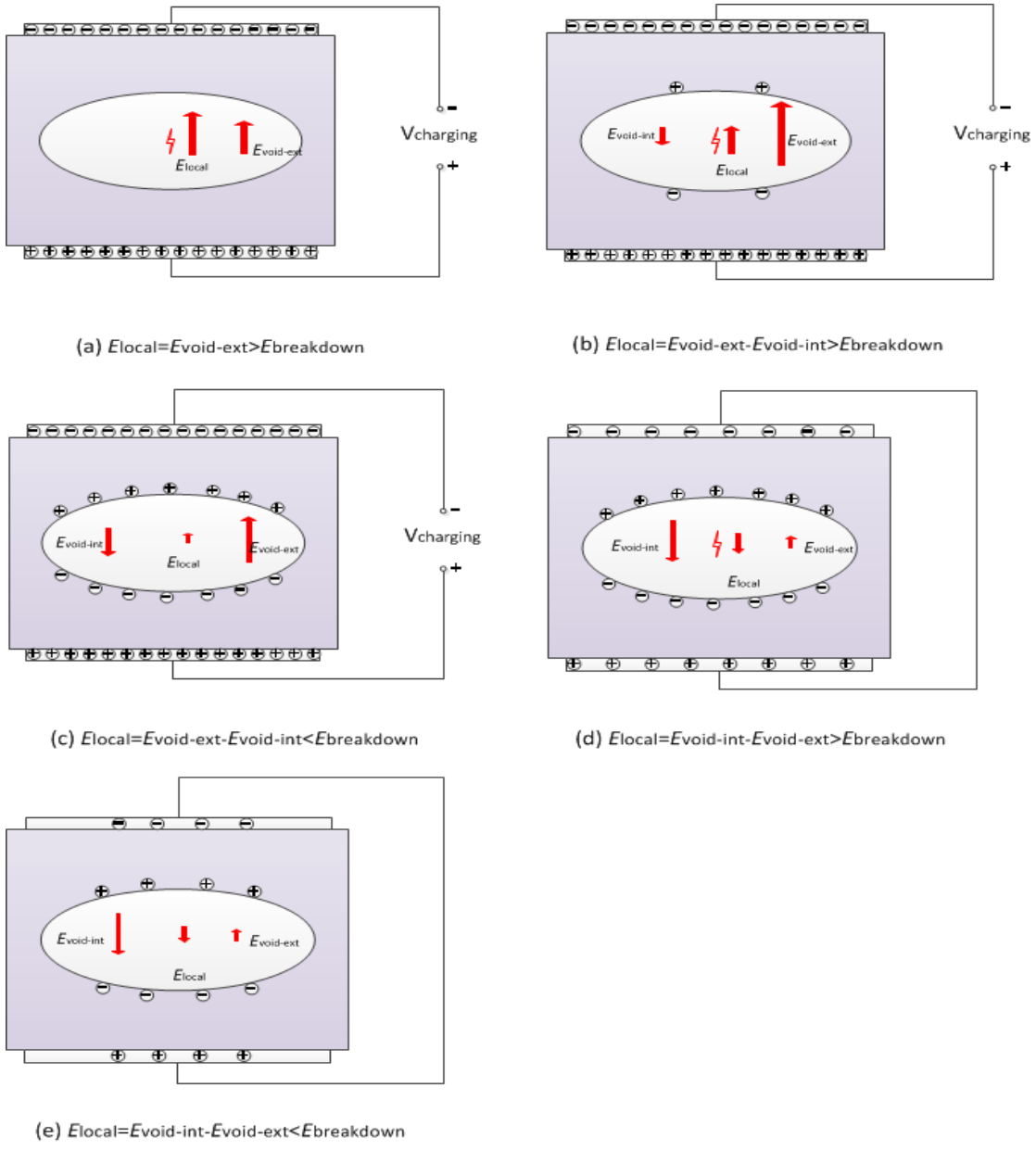

Figure 2-27: Electric charging process in a void. $V_{charging}$ is the charging voltage between the sample electrodes; E_{local} is the real electric field in the void, which is the superposition of $E_{void-ext}$ from the external charges on the electrodes, and $E_{void-int}$ from the internal deposited charges; $E_{breakdown}$ is the breakdown threshold.

During the whole charging process, because the charging electrode and the corona are biased strongly negative, there is a strong repulsion of negative charge. Thus, at the fringes of the corona, any electrons will be accelerated outward into the surrounding air. These free electrons will not travel more than a few millimetres before they are captured by an oxygen molecule to form a negative oxygen ion; a nitrogen molecule which has given up an electron will become a positive nitrogen. For the internal electric breakdown, with the charge on the sample outer surface accumulating to a certain extent, an electric discharge will be triggered in the void, and the generated positive and negative charges will be separately deposited on the void surface.

2.5.3 Charging techniques

In order to render a polymer foam piezoelectric, the voids inside the material must be internally charged [117]. Charging can be achieved by means of direct contact charging, corona discharge without a grid at high corona-point voltages.

2.5.3.1 Direct contact charging

Direct contact charging is the most common polarization technique utilized for piezoelectric material polarization. This charging method can be operated with simple equipment. For piezoelectric material charging, the sample should be coated with electrodes on both surfaces. During the polarization process, the high electric voltage is directly applied to the electrodes and the sample is usually undergoes an elevated temperature treatment to enhance the polarization effect. The schematic of a standard contact charging system is shown in Figure 2-28.

For ferroelectret polarization, the applied charging voltage is usually higher than the expected breakdown voltage, because the size of voids in ferroelectret is not uniform. The problem of this polarization method is that if any defect exists in the sample, it is easily damaged by electric breakdown occurring in the polymer. To reduce the risk of damaging the sample, the charging voltage should be increased gradually and the sample should be immersed in dielectric oil during the polarization [118].

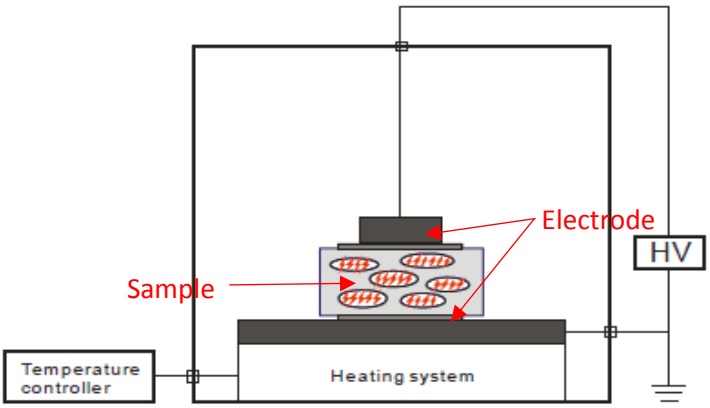

Figure 2-28: Schematic of the contact charging system with temperature controller

2.5.3.2 Corona discharge

Corona discharge is a self-sustainable, non-disruptive electrical discharge which occurs when a sufficiently voltage applied on an asymmetric electrodes such as a steel needle and a metal plate. Because of the high electric filed near the point electrode (steel needle), the air becomes ionized and the resulting ions are driven towards the lower electrode.

Positive ions and negative ion could be generated on positive corona and negative corona, respectively. In air, the positive corona generates hydrated ions $(H_2O)_nH^+$ while the negative corona generates carbonic acid ion (CO_3^-). Ions deposited on the surface layer, these ions can transfer their charges to the surface to create surface potential [119] [120].

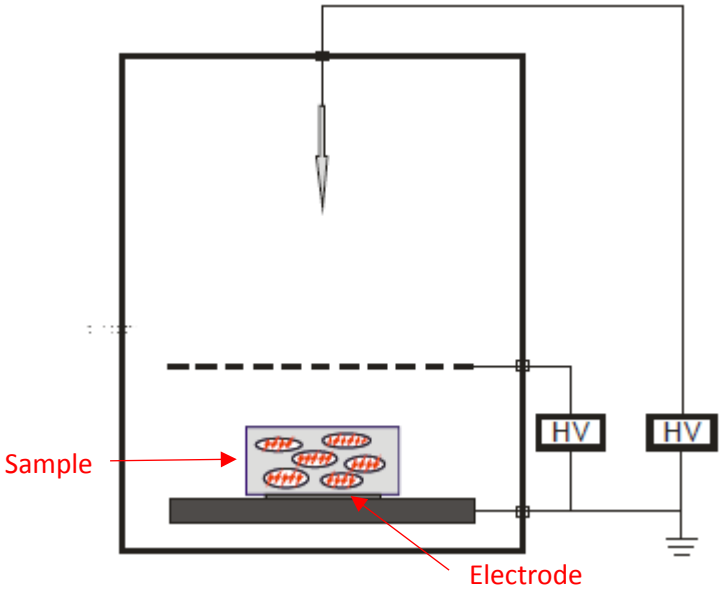

Figure 2-29: Schematic of the tip-to-plane corona charging system

Corona charging method is widely utilized in the lab and in industry. A schematic of the tip-to-plane corona charging system is shown in Figure 2-29. For ferroelectret charging, the bottom of sample can be coated with an electrode to ensure good contact with ground but it is not necessarily required. The needle electrode should be positioned a few centimetres above the sample. When a high electric voltage is applied on the needle electrode, a large amount of ions are deposited on the sample surface to establish a surface potential. The electric breakdown in a void can be triggered by the established surface potential.

In summary, both contact charging and corona charging can trigger gas-breakdown in voids. The difference between them is the mechanisms of creating an internal electric field in the voids. For contact charging, the internal field is formed directly by the voltage between electrodes; for corona charging, it is formed by the deposited surface charges. By comparison, contact charging is riskier as it may damage sample that have some structural defects. As the electrodes are not required for corona charging, it is easier to implement and safer to apply on the large scale for industrial applications.

2.5.3.3 Charging conditions

The influence of electric charging conditions (voltage, time and pressure) on the piezoelectricity of ferroelectrets has attracted lots of researcher's attention.

It is reported that in the contact charging method, the piezoelectric coefficient presents three different stages related to the charge voltage [113]:

- For $V_{breakdown} < V < 2\ V_{breakdown}$, d_{33} increases with charging voltage,
- For $V \leq V_{breakdown}$, d_{33} is equal to zero, and
- For $V \geq 2\ V_{breakdown}$, d_{33} is almost constant.

When the applied charging voltage is below the required breakdown voltage, the ferroelectret could be polarized. If the applied voltage is above the breakdown voltage, the piezoelectric coefficient linearly increases with the charging voltage. When the applied voltage is higher than twice the breakdown voltage, the piezoelectric coefficient becomes constant and will no longer increase.

In terms of investigate the influence of charging time on polarisation, it was found that a charging time longer than 2 s will not enhance the piezoelectricity of ferroelectrets using corona charging [121]. For polarization by direct contact charging, it found that the application of high voltage for 45 microseconds was sufficient to achieve piezoelectricity in 37 and 70 μm thick cellular PP films [122].

More effective corona charging is possible with higher ambient gas pressure during charging or by using gases with higher electrical breakdown strength [95] [123]. Table 2-3 shows the relative breakdown strength of some commonly used gases in a uniform DC electric field at atmospheric pressure. From this table, SF_6 has the highest breakdown strength which is three times higher than air.

Table 2-5: Relative breakdown strength for some gas in corona charging

Gas	**Relative breakdown strength in an uniform DC field**
SF_6	1.00
N_2O	0.44
N_2	0.36
Air	0.30
Ar	0.07

Paajanen and his coworker presented that using nitrogen (N_2) gas in cellular PP foaming procedure can result in a significant improvement in piezoelectric coefficient of about 790 pC/N comparing to using air [95] [124]. In addition, corona charging in N_2 gas with 100 to 450 kPa pressure or in nitrous oxide (N_2O) gas with 100 to140 kPa can result in higher piezoelectricity. The effect of replacing air with sulfur tetrafluoride (SF_6) inside the cellular structure of PP film on its piezoelectric coefficient was also investigated by Qiu [123]. In the experiment, one sample was charged via corona method at a voltage of -60 kV for a charging time of 15 s in SF_6 with a pressure 400 kPa. Another sample was charged in air via the corona method with a voltage of -32 kV for 15 s. The resulted piezoelectric coefficients of cellular PP films charged in air was 215 pC/N, whereas that of cellular PP films charged in SF_6 was 350 pC/N.

In summary, the piezoelectricity of ferroelectrets is generated by electrical breakdown in voids and charge trapped inside void surfaces during charging at high electric fields. At present, corona charging is the primary method to polarize ferroelectret. With the applied voltage increasing, the resulted piezoelectric coefficient presents three different stages. To achieve the highest piezoelectricity, the applied voltage should be two times higher than the required breakdown voltage. However the duration of charging time is not impacting the

piezoelectricity significantly. In addition, the piezoelectric coefficient strongly depends on the gases present in the voids during charging.

2.6 Conclusions

In this chapter, three mechanisms of kinetic energy harvesting for wearable applications are introduced. Piezoelectric transduction is a direct solution, and the future improvement would be developing the piezoelectric material with better flexibility, portability and high piezoelectricity. As discussed in the Section 2.3, ferroelectrets meet these requirements and thought to be the most suitable material for wearable kinetic energy harvesting. Comparing existing materials, fabrication methods and charging technologies for ferroelectret, it is found that piezoelectric properties are limited by the random individual void geometry and irregular overall cellular structure due to its fabrication process. From literature, it can be seen that the piezoelectricity properties of ferroelectret are determined by geometry of the voids. However, most of existing theoretical models only focus on a simplified model. There is no standard system to show the relationship between these geometry parameters of the voids and the piezoelectricity in numerical model. The following chapters will focus on simulation that investigates an optimized void geometry and cellular structure.

3 Analytical Model and ANSYS Simulation

3.1 Introduction

In this chapter, a prototype of the ferroelectret is analysed with special focus on some key design parameters: the geometry and dimensions of voids and their distribution. Before starting the simulation, a simplified theoretical model for the piezoelectricity of ferroelectret has been established. Based on this new theoretical model, simulation was carried out to investigate cellular PDMS structures with a layer of various sized voids. After that, various shaped voids were studied in ANSYS to compare their performance.

3.2 Analytical model

To analyse the piezoelectricity properties of ferroelectret, a simplified model for the piezoelectricity of a charge implanted cellular PDMS structure with micrometer-sized voids is illustrated in Figure 3-1. The model is similar to several previously published ones [68-74], which are used to investigate structure with voids of random size and space distributions.

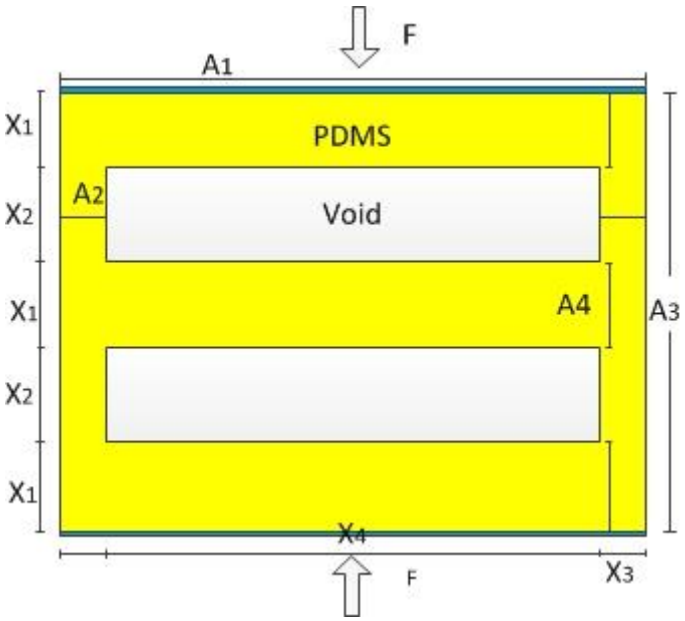

Figure 3-1: A simplified model for the piezoelectricity of a charge-implanted cellular structure

For a structure with *n* void layers and *n*+1 solid PDMS layers, the electric field in the solid layers (E_1) and void layers (E_2) can be obtained from Gauss' law for the interfaces:

$$E_1 = \frac{\sigma_m}{\varepsilon_1 \varepsilon_0} \; and \; E_2 = \frac{\sigma_m - \sigma}{\varepsilon_0} \tag{3-1}$$

where σ_m is the charge density on the electrodes, σ is the charge density on void surface, and ε_1 and ε_0 are the dielectric constant of air and the relative dielectric constant of PDMS, respectively. From Kirchhoff's second law under short circuit conditions

$$V = \int E \, dx = (n+1)x_1 E_1 + n x_2 E_2 = 0 \tag{3-2}$$

where V is the electric potential across the electrode pair, and x_1 and x_2 are the thicknesses of solid and void layers, respectively. Substituting Eq. (3-2) into Eq. (3-1) leads to:

$$\sigma_m = \frac{n\varepsilon_1 \sigma x_2}{[(n+1)x_1 + n\varepsilon_1 x_2]} \tag{3-3}$$

Therefore, the variation of the charge density on the electrodes ($\Delta\sigma_m$) can be expressed as a function of the thickness variation (Δx_1 and Δx_2) as

$$\Delta\sigma_m = \frac{\partial \sigma_m}{\partial x_1}\Delta x_1 + \frac{\partial \sigma_m}{\partial x_2}\Delta x_2 = \frac{-n(n+1)\varepsilon_1 \sigma x_2}{[(n+1)x_1 + n\varepsilon_1 x_2]^2}\Delta x_1 + \frac{n(n+1)\varepsilon_1 \sigma x_1}{[(n+1)x_1 + n\varepsilon_1 x_2]^2}\Delta x_2 \tag{3-4}$$

The application of an external force (F) deforms the multilayer structure, and the relationships between the resulting stresses and strains can be expressed as

$$\frac{F}{A_3} = c_{33}\frac{\Delta x_3}{x_3} \; and \; \frac{F}{A_4} = \frac{F}{sr_2 A_3} = c_{33}\frac{\Delta x_4}{x_4} \tag{3-5}$$

where c_{33} is the elastic modulus of PDMS, A_3 and A_4 are the effective areas of the solid and void layers, respectively and sr_2 is the ratio of A_4 to A_3. The relationship between the thickness variations, Δx_3 and Δx_4, is therefore

$$\frac{\Delta x_4}{\Delta x_3} = \frac{1}{sr_2}\frac{x_4}{x_3} = \frac{tr_2}{sr_2} \tag{3-6}$$

where tr_2 is the ratio of x_4 to x_3,

Due to the Poisson effect, the relationships between the thickness variations, Δx_3 and Δx_2, Δx_4 and Δx_1, are therefore

$$\gamma\frac{\Delta x_3}{x_3} = \frac{\Delta x_2}{x_2}\ and\ \gamma\frac{\Delta x_4}{x_4} = \frac{\Delta x_1}{x_1} \tag{3-7}$$

Where γ is the Poisson's ratio,

By substituting Eq. (3-6) into Eq. (3-7), the relationship between Δx_2, Δx_1, x_2 and x_1 is therefore

$$\Delta x_1 x_2 = \frac{1}{sr_2}\Delta x_2 x_1 \tag{3-8}$$

By substituting equation (3-8) into equation (3-4), the variation of the charge density on the electrodes ($\Delta\sigma_m$) can be expressed as

$$\Delta\sigma_m = \frac{n(n+1)\varepsilon_1\sigma(sr_2-1)x_2}{[(n+1)x_1+n\varepsilon_1 x_2]^2}\Delta x_1 \tag{3-9}$$

Since only a certain portion of the electrode surface is charged, the effective charge density $(\sigma_m)_{eff}$, and its variation, $(\Delta\sigma_m)_{eff}$, should be given by:

$$(\sigma_m)_{eff} = (1-sr_1)\sigma_m\ and\ (\Delta\sigma_m)_{eff} = (1-sr_1)\Delta\sigma_m \tag{3-10}$$

where A_1 and A_2 are the effective areas of the solid and void layers, respectively, and sr_1 is the ratio of A_2 to A_1.

By its definition, the piezoelectric coefficient (d_{31}) can be expressed as

$$d_{31} = \frac{(\Delta\sigma_m)_{eff}}{F/A_3} = \frac{n(n+1)\varepsilon_1\sigma tr_1(1-sr_1)(sr_2-1)\gamma}{[(n+1)+n\varepsilon_1 tr_1]^2 c_{33}} \tag{3-11}$$

where tr_1 is the ratio of x_2 to x_1,

The piezoelectric coefficient (d_{33}) can be expressed as

$$d_{33} = \frac{(\Delta\sigma_m)_{eff}}{F/A_1} = \frac{n(n+1)\varepsilon_1\sigma tr_1(1-sr_1)^2}{sr_1[(n+1)+n\varepsilon_1 tr_1]^2 c_{33}} \quad (3\text{-}12)$$

Hence,

$$\frac{d_{33}}{d_{31}} = \frac{1-sr_1}{sr_1(sr_2-1)\gamma} \ (0 < sr_1, sr_2 < 1) \quad (3\text{-}13)$$

As n, ε_1 and tr_1 are always positive

$$(n+1) + n\varepsilon_1 tr_1 \geq 2\sqrt{n(n+1)\varepsilon_1 tr_1 \varepsilon_1} \quad (3\text{-}14)$$

The piezoelectric coefficient (d_{33}) can be simplified as

$$d_{33} \leq \frac{(1-sr_1)^2\sigma}{4sr_1 c_{33}} (0 < sr_1 < 1) \quad (3\text{-}15)$$

According to equation (3-12), the piezoelectricity of a charged implanted, cellular polymer structure is determined by its geometry, elastic modulus and charge density. To simplify the analysis, it is assumed that the elastic modulus and charge density is constant at this stage. Therefore only the geometry of voids should be considered. If the parameter with the most significant impact on piezoelectricity properties can be identified, the optimal cellular structure can be designed and implemented.

For single layer PDMS ferroelectret, an analytical result of its piezoelectric coefficients d_{33} with regard to its geometry is provided in Figure 3-2 (a). It numerically illustrates the impact of the different void size on d_{33} through Eq. (3-12). Based on Eq. (3-13), the theoretical d_{33} values is calculated with surface charge density σ=100 μC/m^2, Young's modules c_{33}= 360 KPa, the relative dielectric constant of PDMS ε_1= 2.5 and void layer n=1 [125] [126]. While the ratio of the effective areas of the solid and void layers are increased, the piezoelectricity of PDMS ferroelectret is reduced. In other word, the piezoelectric properties of the PDMS ferroelectret are improved with increasing void area (sr_1 reducing in Figure 3-2 (b)). In contrast, when the ratio of the thicknesses of the solid and void layers tr_1 is increased (tr_1 increasing in Figure 3-2 (b)), the piezoelectric properties of the PDMS ferroelectret is

improved and the optimised ratio has been demonstrated at around 0.8, with a peak piezoelectric coefficient of 220 pC/N.

From the simplified d_{33} Eq. (3-16), the ferroelectret material is selected, the value of σ and c_{33} can be considered as constant. The maximum d_{33} of ferroelectret foam only varies with the values of sr_1. To achieve the maximum value, the value of n+1 should be equal to the value of $n\varepsilon_1 tr_1$. Figure 3-3 illustrates the relationship between the number of void layer n and the optimised ratio of tr_1. From this figure, it is found for the multilayer ferroelectret, with increasing number of void layers, the optimised ratio of the thickness of the solid layer to that of the void layer is eventually stabilized at around 0.4. To achieve higher piezoelectric properties for multilayer ferroelectret, one should increase the void area as much as possible and maintain the thickness ratio of the solid and void layers, tr_1 at 0.4.

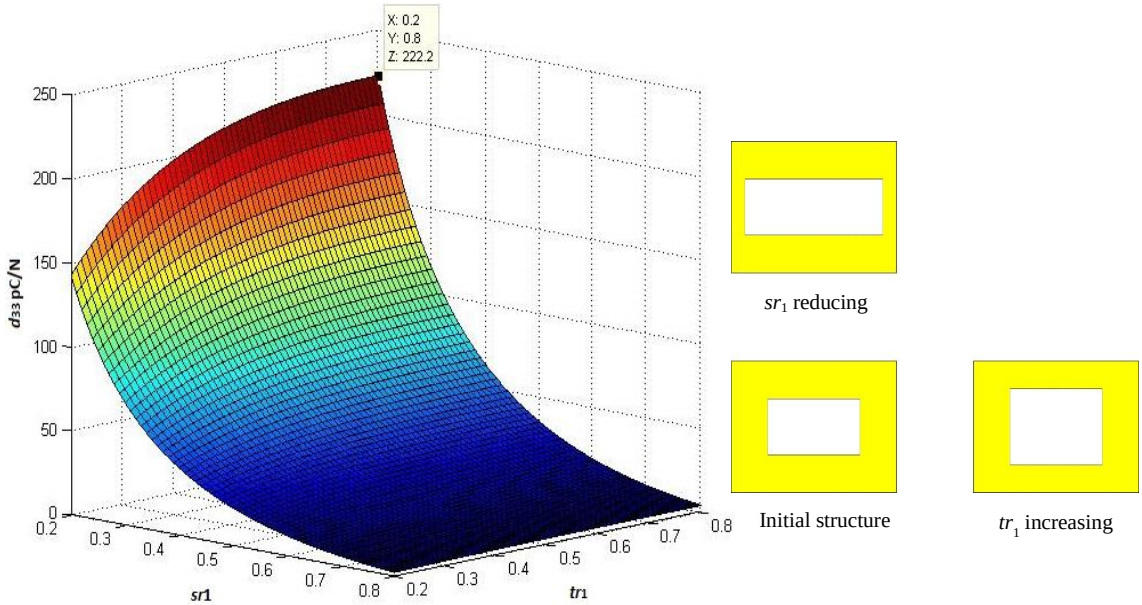

Figure 3-2: (a) Analytical rectangle model results varying with the size of voids and (b) the schematic of the structure changing with tr_1 and sr_1

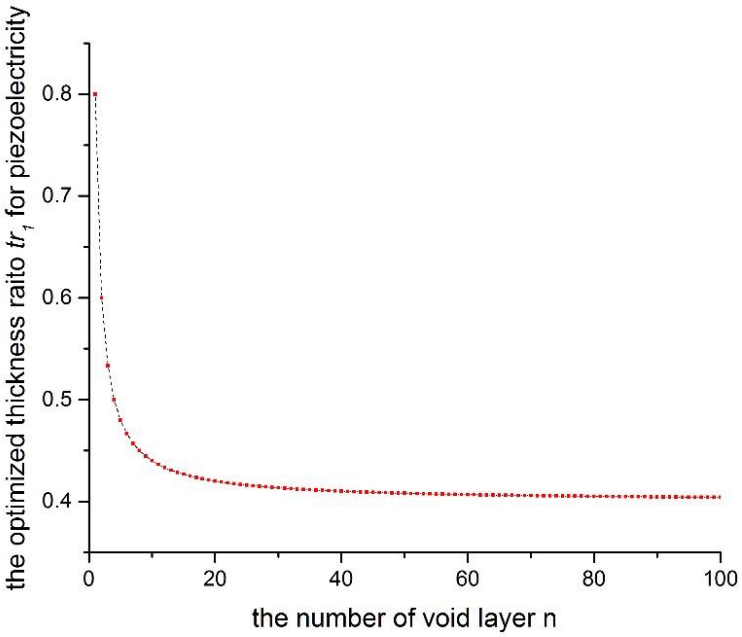

Figure 3-3: the relationship between the number of void layer n and the optimised ratio of tr_1

To investigate the piezoelectricity varying with different void shapes, two models are established based on the rectangular void model: parallelogram void model and sector void model. The two simplified models for studying the piezoelectricity of a charge implanted cellular PDMS structure with parallelogram voids and sector voids are illustrated in Figure 3-4 and Figure 3-5, respectively.

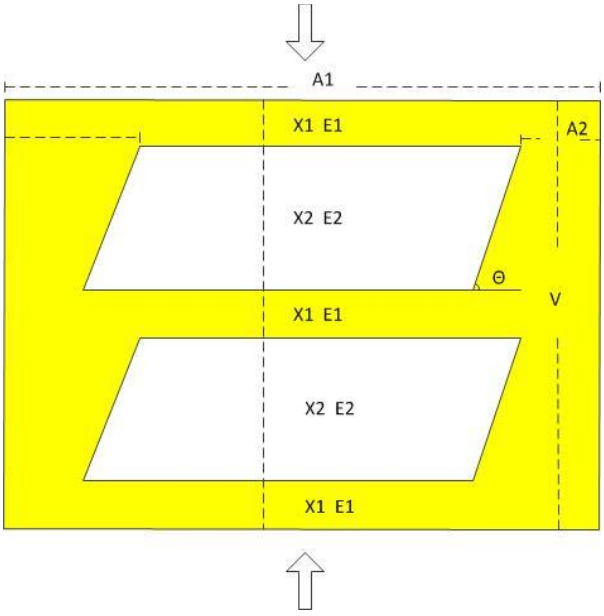

Figure 3-4: A simplified model for the piezoelectricity of a charge-implanted cellular structure with parallelogram void

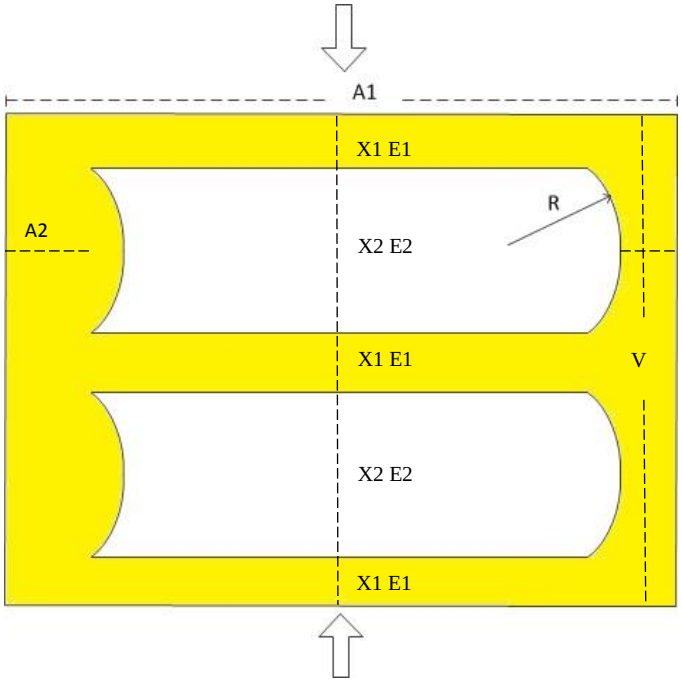

Figure 3-5: A simplified model for the piezoelectricity of a charge-implanted cellular structure with sector void

The void area in the two models is the same as the void area in the rectangular void model discussed above. The main difference between these two models and the rectangular void

model is the relationships between the resulting stresses and strains due to the different area ratio computational formula of the effective areas of the solid and void layers.

For the parallelogram voids model, the ratio of the effective area of the solid layer to that of the void layers can be expressed as:

$$sr_1 = \frac{A_2 - \frac{x_2}{tan\theta}}{A_1} \tag{3-16}$$

Where θ is the slope of parallelogram, A_1 and A_2 is the areas of the solid layers and void layer respectively.

For the sector voids model, the ratio of the effective area of the solid layer to that of the void layer can be calculated by:

$$sr_1 = \frac{A_2 - R + \sqrt{R^2 - \frac{{x_2}^2}{4}}}{A_1} \tag{3-17}$$

Where R is the radius of curves, x_2 is the thickness of the void layer.

The sr_1 value can then be substituted into the equation (3-11); and the piezoelectricity can be estimated. The calculated value of sr_1 for parallelogram void ferroelectret model varying with the slope is shown in Figure 3-6. From the figure, it is found for the ferroelectret with parallelogram voids, the equivalent area ratio increases with the slope of parallelogram void increasing. Figure 3-7 presents the relationships between the calculated values of sr_1 for sector void ferroelectret model and the radius of curves. From this figure, it can be observed that the equivalent area ratio of sector void increase with the radium of curves increasing.

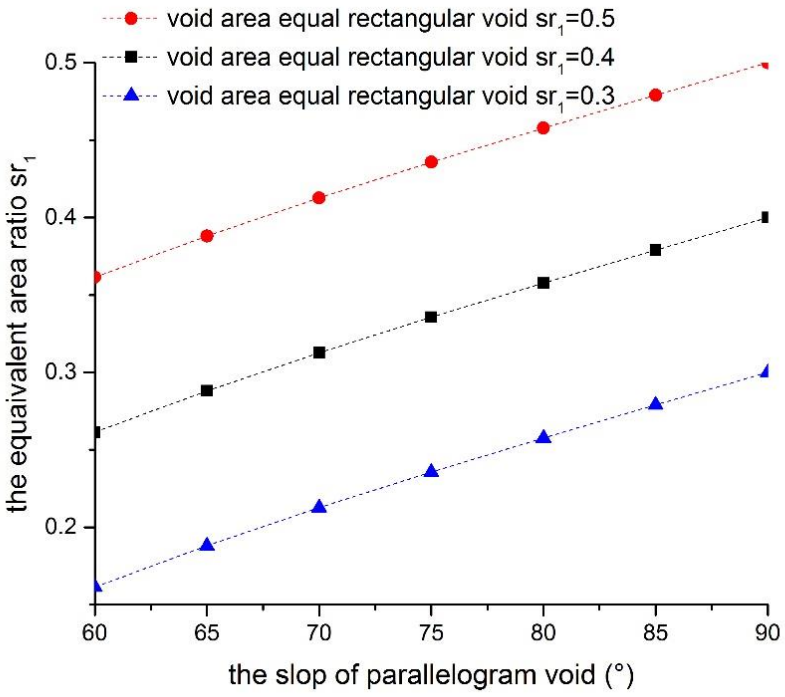

Figure 3-6: The values of sr_1 varying with the slope of parallelogram

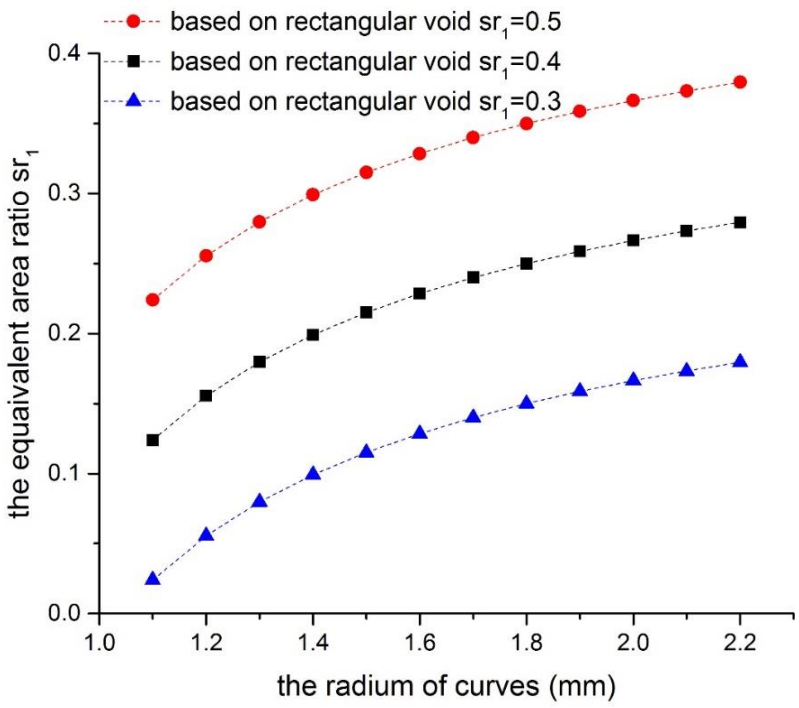

Figure 3-7: The values of sr_1 varying with the radius of the sector

3.3 ANSYS simulation

ANSYS is a Finite Element Analysis (FEA) software models are built as real structure, and then each part divided into discrete parts for analysis. The boundary conditions and environment changes are drawn into the model. Furthermore, all the material properties and some physical parameters such as force or pressure can be applied in the software. This means the FEA model for the ferroelectret material can be built in ANSYS. In addition, ANSYS provides the interface to some CAD (e.g. SolidWorks) software, therefore the void structure of the model can be conveniently modified.

3.3.1 Parameters of ferroelectret model

3.3.1.1 Ferroelectet material and geometry

Ferroelectret material and geometry are two defining elements ferroelectret film. Although the material used in this simulation is PDMS, the model can be applied to any ferroelectret material. The Young's modulus, dielectric constant and Poisson ratio of PDMS are 360 kPa, 2.5 and 0.5, respectively [125]. This project aims to optimise the voids structure in ferroelectret for energy harvesting. Therefore, only materials with high charge density are considered.

For the geometries, different void sizes and shapes will be created and simulated using 2D model in ANSYS. To investigate the effect of void size, single layer rectangular void ferroelectret model is utilized in the simulation. The thicknesses of the solid layer and void layer are selected as 2 mm and 1.6 mm, respectively; the width of the voids and the gap between the voids is selected as 0.75 mm and 0.5 mm, respectively. The entire ferroelectret foam model contains 10 voids.

Three void shapes including rectangle, parallelogram and sector were studied. These models are modified from the rectangle model and the ratio of the thickness of the solid and void layers tr_1 is kept at 0.8.

The three ferroelectret models, rectangular, parallelogram and sector void, are shown in Figure 3-8.

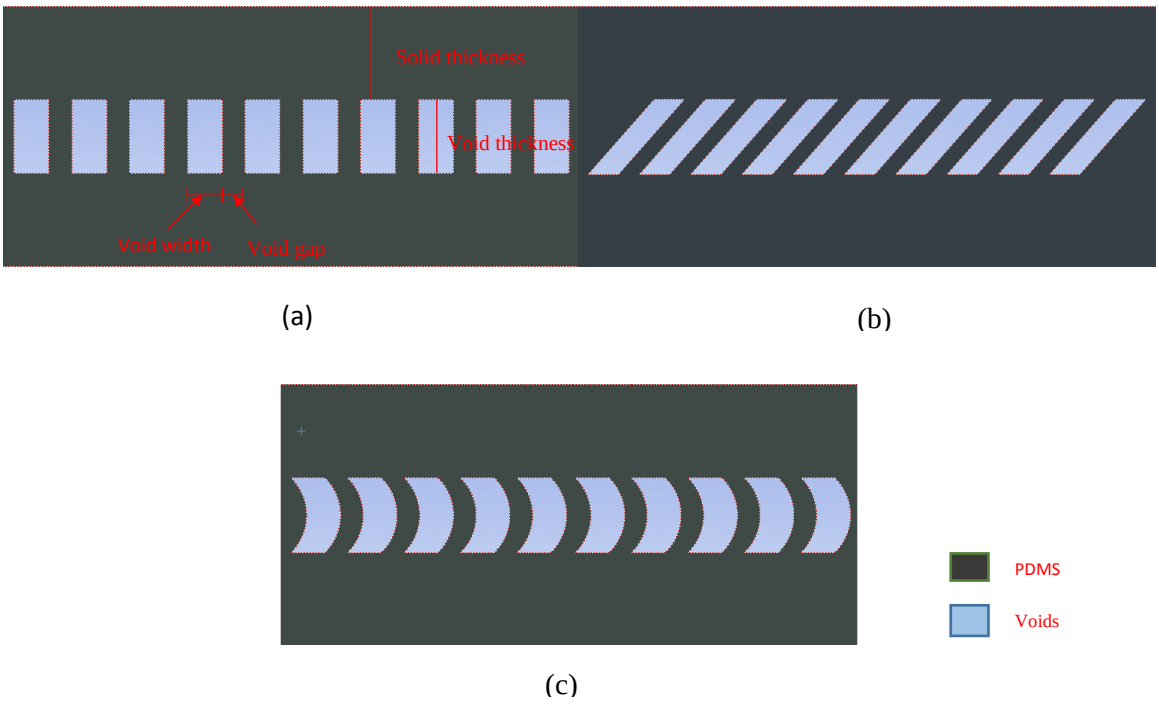

Figure 3-8: The structure of ferroelectret models with rectangle (a), parallelogram (b) and sector void (c) for ANSYS simulation

3.3.1.2 Force applied on film

The force applied on the surface of film generates pressure. As the force is applied, a deformation is generated on the void layer and the void area will be decreased. For this simulation, a uniform pressure is applied on the top surface of ferroelectret and the bottom surface is set to being fixed. In addition, the applied pressure could not be excessive. If applied pressure is overwhelming, all cavities of ferroelectret will collapse. For current geometry size and material Young's modulus, the applied pressure is selected as 1 kPa.

3.3.2 Principle of ANSYS simulation

From the equation (3-4) and (3-11), it can be found that the piezoelectric properties of ferroelectret are determined by charge density variation on the electrodes ($\Delta\sigma_m$) which is changing with the number of void and solid thickness variation. The cellular PDMS structures are simulated in ANSYS 2D. ANSYS results predicted deformation of the voids when the structure is subject to an external mechanical load. In workbench user interface, a

static structural analysis set was selected as analysis system in this work. The PDMS material properties and geometry of sample which were described in previous section were add into "Engineering Data" and "Geometry" analysis module, respectively. The advanced analysis type option in "Geometry" module was set to 2D. Before staring ANSYS, the Finite Element model should be created. The "detail of Mesh" setting in Mechanical window was used to define the generating method and size of Finite Element, as shown in Figure 3-9 (a). "On: Proximity and Curvature" was selected for the "Use Advanced Size Function" option. This means that more elements will be created among the voids. The generated mesh was shown in Figure 3-9 (b). After generating the mesh, the support conditions and force were set as shown in Figure 3-10. In addition, The "Large deflection" in "Analysis Setting" was set to "ON".

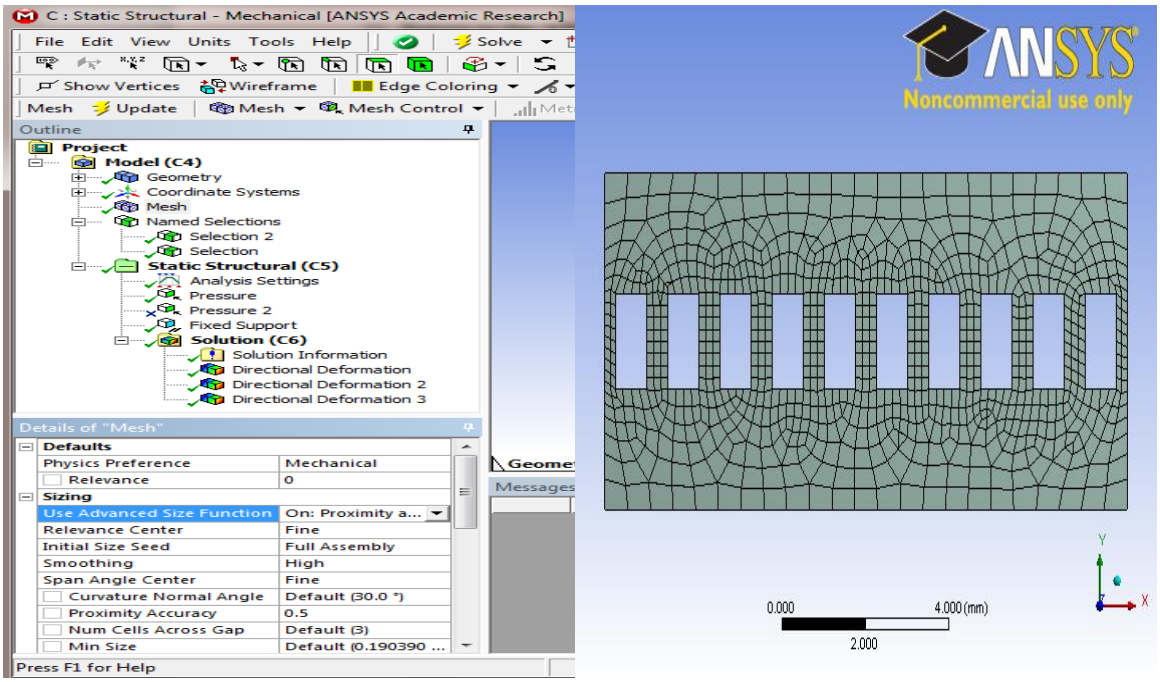

(a) (b)

Figure 3-9: (a) The model feature for Mesh options; (b) the resulting mesh for ferroelectret ANSYS simulations

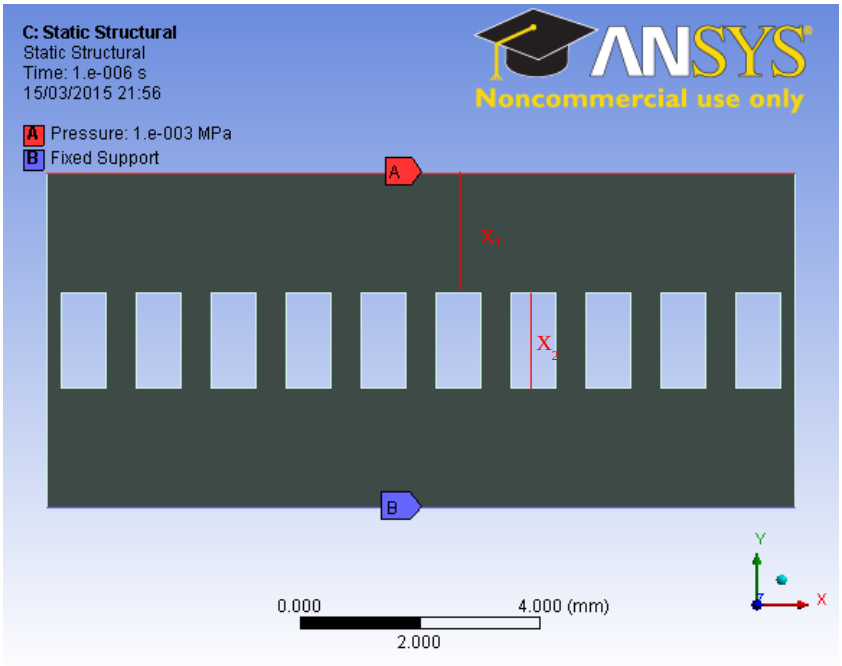

Figure 3-10: Force applied on ferroelectret for ANSYS simulation

Figure 3-11 presents the deformations of ferroelectret with rectangular voids in the thickness direction. The variation of void layer Δx_2 equals the deformation of the upper surface of void plus the deformation of bottom surface of void. Due to the irregular deformation on void area, the variations of void layer Δx_2 should take the average value. The variation of solid layer x_1 equals the variation of whole foam thickness minus the variations of void layer Δx_2. Then the piezoelectric coefficient d_{33} is calculated at surface charge density σ=100 μC/m^2, the relative dielectric constant of PDMS ε_1= 2.5 and the external pressure P=1 kPa.

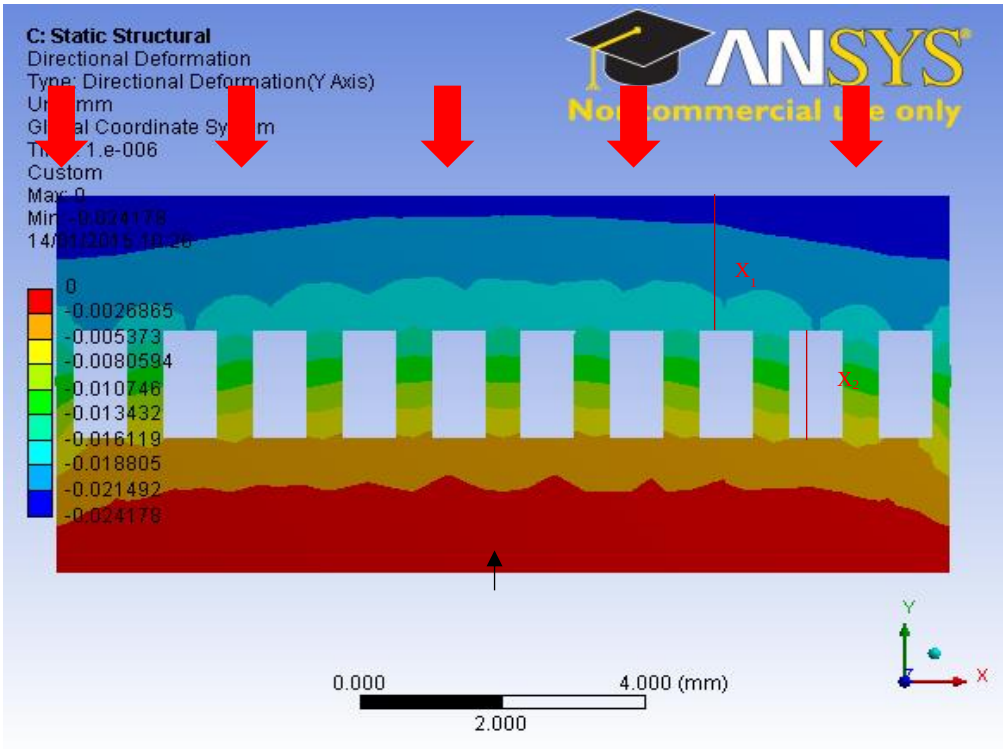

Figure 3-11: An image of ANSYS simulation deformation results for single rectangle void layer ferroelectret in thickness direction

In data processing, assuming the charge densities of the voids surface was uniform; the variation of the charge on the external surface can be calculated by the average of the deformations. Then the piezoelectric coefficient d_{33} can be estimated by it definition:

$$d_{33} = \frac{(\Delta\sigma_m)_{eff}}{F/A_1} \tag{3-18}$$

By substituting equation (3-6) into equation (3-18), the piezoelectric coefficient d_{33} can be expressed as

$$d_{33} = 2\varepsilon_1\sigma(x_2\Delta x_1 + x_1\Delta x_2)(2x_1 + \varepsilon_1 x_2)^{-2}P^{-1} \tag{3-19}$$

where ε_1 is the dielectric constant of air and the relative dielectric constant of PDMS; σ is the charge density on void surface; x_1 and x_2 are the thickness of solid and void layers, respectively; Δx_1 and Δx_2 are the variations of the thickness and P is the external pressure.

3.3.3 The effects of void size and void shape

In the varying void size simulation, the selected values of sr_1 and tr_1 should guarantee that the voids of generated ferroelectret model could not collapsed under an external pressure P=1 kPa. Considering the feasibility of fabrication processes, the possible range of sr_1 and tr_1 for void size simulation is from 0.2 to 0.7.

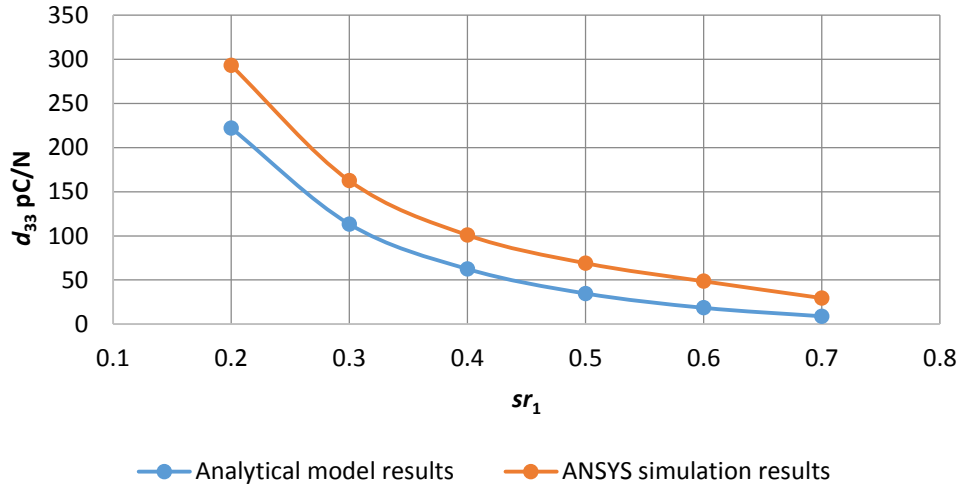

Figure 3-12: Analytical model results and ANSYS simulation d33 results for rectangle voids varying with sr_1 at tr_1=0.8

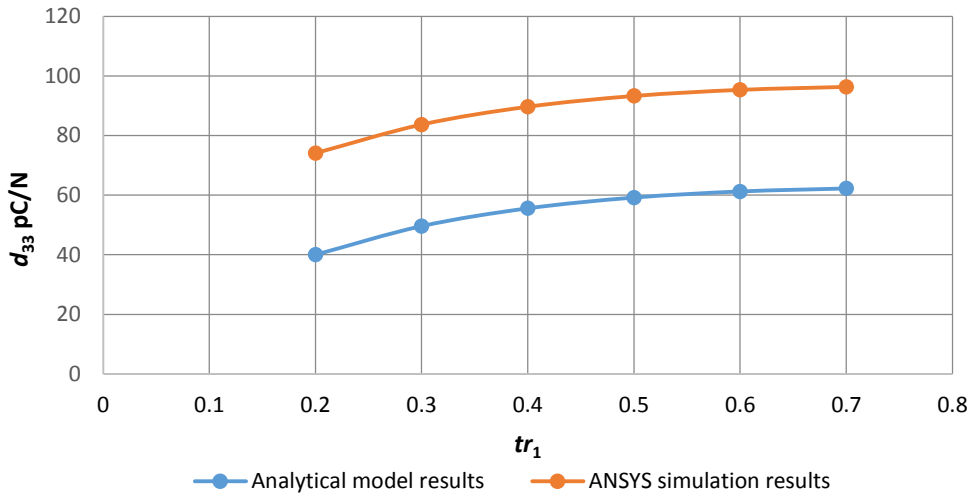

Figure 3-13: Analytical model results and ANSYS simulation d33 results for rectangle voids varying with tr_1 at sr_1=0.4

Results of the analytical model and ANSYS simulation varying with the value of sr_1 and tr_1 are shown in Figure 3-12 and 3-13, respectively. From Figure 3-12, it should be noticed that the piezoelectric coefficients d_{33} increase significantly with the decrease of the value of sr_1 when tr_1=0.8. From Figure 3-13, it can be observed that the piezoelectric coefficients d_{33} increase slightly with the increase of the value of tr_1 when sr_1=0.4. In addition, from these results, there is a difference of 20% to 30% between the analytical model results and the ANSYS simulation results. The possible reason for the difference is caused by that the analytical model only considers rigid deformation. The analytical model does not take into account any bending deformation of material resulting in the shape of void that remains unchanged. In fact, the shape of void will change due to the bending effect of material.

Results of the analytical model and ANSYS simulation for parallelogram void varying with the slope of parallelogram which is the acute angle between the hypotenuse and the base is shown in Figure 3-14. The valid range of the slope of parallelogram should be from 65° to 90° because this model don not consider the electric field distribution. In this model, with the slope of parallelogram decreasing, the distribution direction of electric field is parallel to the slope of parallelogram. In reality, the distribution direction of electric field is always going to be perpendicular. The comparison of analytical model results and ANSYS simulation results for vector void varying with the radius of curve is shown in Figure 3-15. From Figure 3-16, it is found that the piezoelectric coefficient d_{33} increases with the decrease of the slope of parallelogram. Figure 3-14 shows that the piezoelectric coefficient d_{33} decreases with the increasing of the radium of curve. Due to the analytical model is designed for rectangular voids, there are errors between the ANSYS simulation and analytical results in structures with parallelogram and sector voids. However, the values of slope and radius could not achieve too small because the geometry of void cannot exceed the boundary of the film.

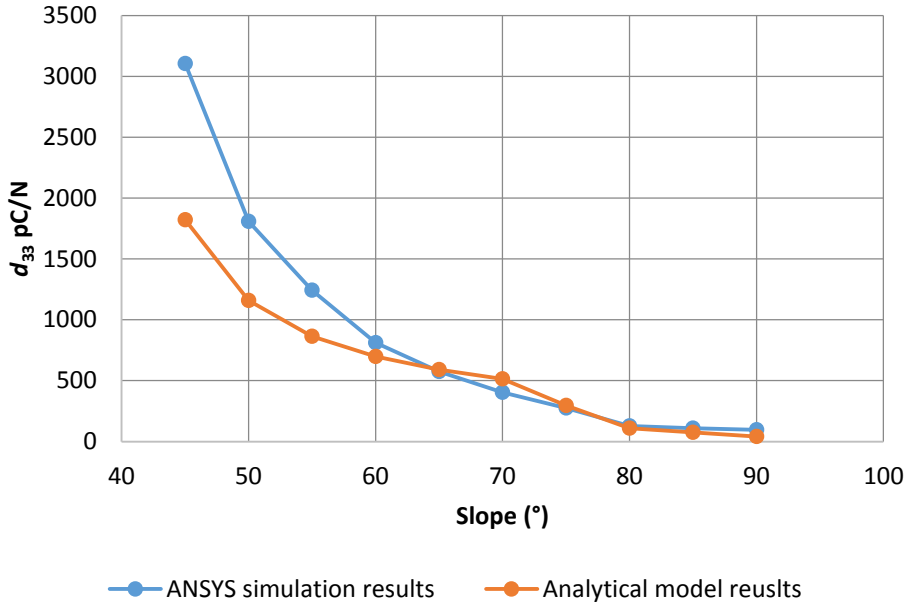

Figure 3-14: Analytical model results and ANSYS simulation d33 results for parallelogram voids varying with the slope

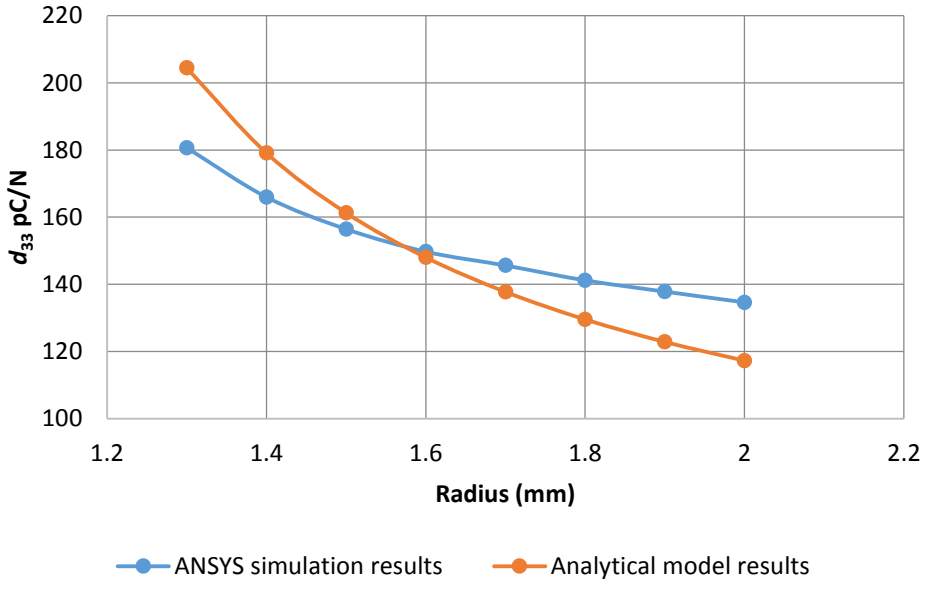

Figure 3-15: Analytical model results and ANSYS simulation d33 results for sector voids varying with the radius of curve

By comparing with results for the three different void shapes, the parallelogram void ferroelectret can achieve higher piezoelectric properties constants. From these results, it is

found that the piezoelectric coefficient d_{33} significant enhance with the decreasing of the sr_1 value.

3.3.4 The effects of void distribution

In the previous ANSYS simulation, the singular void layer was located at the horizontal centerline of film. To investigate the void deformation effected by void distribution, the void layer should be relocated off the horizontal centerline and the other simulation parameters remain the same. Results of void deformation ratio in ANSYS simulation varying with the off horizontal centreline ratio is shown in Figure 3-16. The off horizontal centreline ratio is the ratio of the distance of the void layer from the horizontal centreline to the half thickness of whole film (Figure 3-17). While off centre distance ratio equal zero, the void layer located at the horizontal centreline of the film, the void deformation in this case is used to be the reference value. The void deformation ratio is the ratio of the void deformation to the reference value. It is found that the void deformation increases with the increasing off horizontal centreline ratio. In other word, while the void was disturbed near the surface, the void deformation is significantly increased resulting in higher piezoelectric properties.

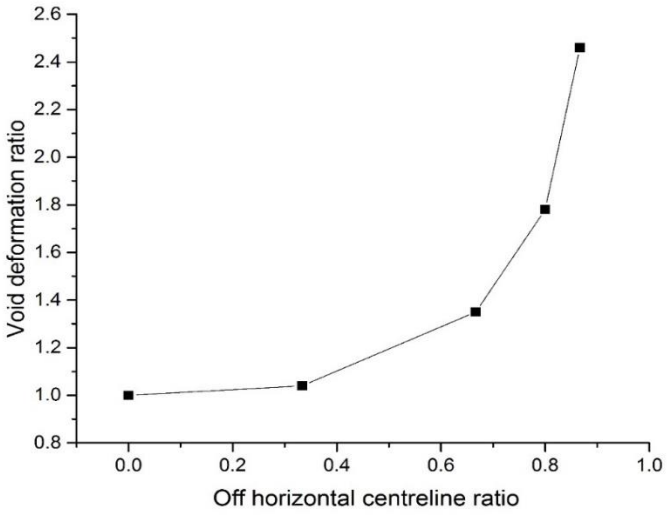

Figure 3-16: ANSYS simulation of void deformation ratio results varying with off horizontal centreline ratio

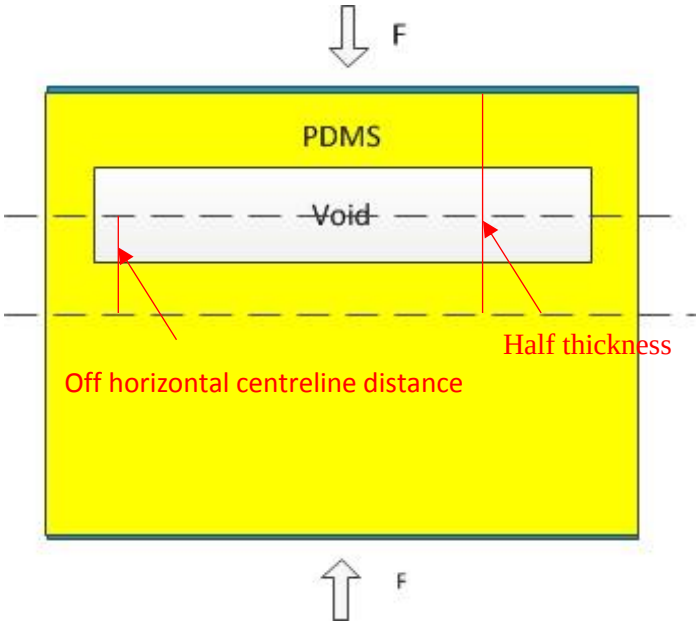

Figure 3-17: The schematic showing off horizontal centreline ratio

3.4 Conclusions

In this chapter, the structure of ferroelectret has been modelled analytically and in ANSYS simulation. Piezoelectric coefficients of ferroelectret structures with different void sizes and shapes were studied and compared. The results for single void layer PDMS ferroelectret show that the optimized piezoelectric coefficients d_{33} is achieved at the thickness ratio tr_1=0.8 and a lowest possible sr_1. From the analytical results, the optimized piezoelectric coefficients d_{33} for multilayers PDMS ferroelectret is obtained at the tr_1=0.4 which is the ratio of the effective area of void layers to the effective area of solid layers. Moreover, the results comparing different void shapes show that the parallelogram void ferroelectret can achieve higher piezoelectric coefficients d_{33} compared to rectangular and sector voids. In addition, while the void is disturbed near the surface, the ferroelectret presents higher piezoelectric properties.

4 PDMS Ferroelectret Fabricated by 3D Printed Moulding Method

4.1 Introduction

In this chapter, fabrication and characteristics of various void structures made of a ferroelectret material, PDMS, using 3D-printed plastic moulding were presented and discussed. The 3D-printing based fabrication strategy is selected as it is more flexible than any other fabrication methods. PDMS was chosen as the material because it is MEMS compatible which greatly facilitates the integration of the presented piezoelectric films with common microsystems. After electric charging, the energy harvesting properties of the PDMS ferroelectret was investigated using an electrodynamic instrument, allowing applied compressive force and momentum to be correlated with energy output.

4.2 Fabrication process

4.2.1 Mould preparation

To investigate the piezoelectric properties that are affected by the structure ratios, three different structures with rectangular voids were designed. Depending on the maximum precision of the 3D printer and the restrictions of the fabrication process, the maximum structure ratio tr_1 and sr_1 for single void layer ferroelectret was 0.8 and 0.4 respectively. Based on these ratios, three ferroelectret structures with different dimensions were designed. For one structure, the thicknesses of the solid layer and the rectangular void layer were selected as 0.4 mm and 0.32 mm respectively; and widths of the voids and the gap between the voids were 0.75 mm and 0.5 mm, respectively. For the other structure, the value of the thicknesses of the solid layer and the rectangular void layer were 5 times larger than the former one, which were 2 mm and 1.6 mm respectively; the width and the gap between the voids remained the same. For the third structure, the structure ratio tr_1 and sr_1 were fixed at 0.8 and 0.5; the thicknesses of solid layer and the rectangle void layer were selected as 2 mm

and 1.6 mm, respectively; the width of the voids and the gap between the voids were 0.625 mm and 0.625 mm. A summary of the dimension of the three structures is shown on the table below:

Table 4-1: The dimensions for the three designed structures

	tr_1	sr_1	Thickness (Solid layer)	Thickness (Void layer)	Width (Void)	Width (Void gap)
Structure 1	0.8	0.4	0.4 mm	0.32 mm	0.75 mm	0.5 mm
Structure 2	0.8	0.4	2 mm	1.6 mm	0.75 mm	0.5 mm
Structure 3	0.8	0.5	2 mm	1.6 mm	0.625 mm	0.625 mm

To obtain each of the required structures, two moulds parts with different details were designed for each structure. One has open void structure pattern in the centre, while the other has a smooth surface of the same area. In addition, sidewalls of these two parts were used to control the thickness and area of film. The outer dimensions for these moulds were 38 × 38 mm.

For this experiment, the 3D-printed plastic moulds were printed by a Connex350^{TM} 3D printing system (Stratasys, MN, USA). The 3D CAD model of the used moulds structure were constructed with Solidworks 2012 (Dassault System, MA, USA) and exported as STL-format file which is for compatibility with Connex350^{TM} 3D printing system. The moulds can be made from VeroWhitePlus^{TM}, VeroGery^{TM} or VeroClear^{TM}. The VeroClear^{TM} was selected because it is transparent and so fabrication process of ferroelectret structures can be better observed. The designed moulds were generated in glossy printer mode on a bed of FullCure®705 support material. The operation mechanism of 3D printer is that the STL file needs to be processed by a piece of software slicer that converts the model into a series of

thin layers and produces a G-code file then the printer follows the G-code file to lay down successive layers of liquid material and be cured by UV-exposure to build the mould from a series of cross sections. Because the 3D printed material inhibits PDMS polymerization and the printed structure tends to warp to some extent when it is removed from the printer, the resulting 3D-printed mould is not directly suitable for PDMS casting. The moulds should first be baked in oven at 80 °C for 24 hours. In this step, the moulds were placed and glued by a drop of degassed non-polymerized PDMS to a piece of clear glass, with its base in contact with the PDMS film. After this step, the glass-backed moulds were exposed to a silane vapour for 1 hour to coat with a thin layer of trichloro(1H,1H,2H,2H-perfluorooctyl)silane (Sigma Aldrich, MO, USA). After this step, these baked moulds were flat and no longer inhibited with PDMS. An example of a prepared mould of VeroClear™ material and the schematic of the 3D printed mould are shown in Figure 4-1.

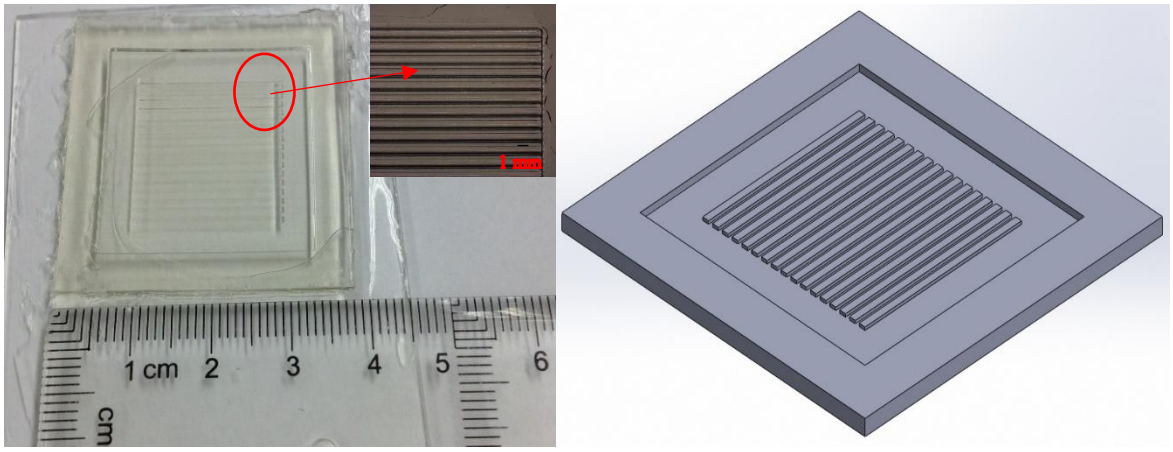

(a) (b)

Figure 4-1: (a) The image of a prepared 3D-printed mould and (b) the schematic of the 3D printed mould

4.2.2 PDMS casting and bonding

Liquid PDMS and curing agent (Sylgard 184 from Dow Corning, MI, USA) were mixed at a 10:1 weight ratio and then the mixture was degassed in a vacuum desiccator for 15 minutes. The degassed PDMS was poured into the glass-backed moulds which were again degassed

and then baked at 80 °C for 1 hour. When the degassed PDMS was poured into the moulds, the fluid level in the mould was monitored to ensure the degassed PDMS would not overflow, which is used to control the thickness of foam. The upper and lower parts were fabricated separately and then bonded together. There are two possible methods to bond the two PDMS parts: applying glue or utilizing an oxygen plasma machine. For the first method, degassed PDMS was utilized as the adhesive. After detaching the polymerized PDMS from the moulds, the degassed PDMS was painted on the PDMS layer with flat surface and then the other PDMS layer was placed on it, with its pattern surface in contact with the flat surface. This bonding method was easily implemented but the dosage of adhesive was difficult to control. Overdose can lead to overflow into the void which could change the whole cellular structure. In the second method, after detaching the polymerized PDMS from the moulds, an oxygen plasma treatment was applied to both the patterned surface of the PDMS layer and the smooth surface of the other PDMS layer (Femto Asher, Diener, Germany, 30 S at 35-40W) which were then bonded together. The bonded PDMS was then baked in oven at 80 °C for 1 hour with a 1kg mass was placed on top of the sample to improve the bonding effect. The schematic of PDMS casting and bonding processes, and the cross-section view of the bonded sample by plasma treatment are illustrated in Figure 4-2 and Figure 4-3, respectively.

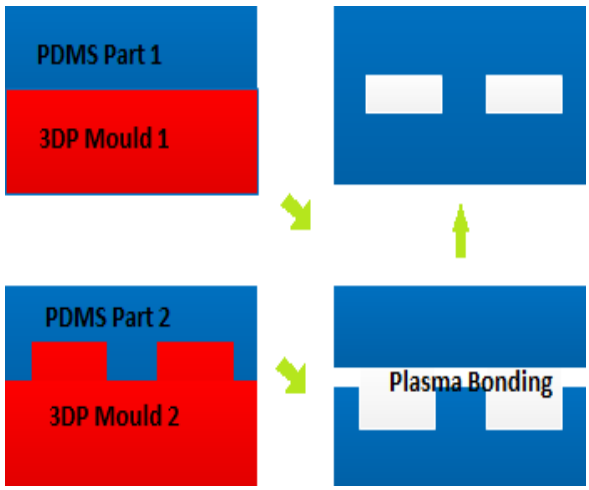

Figure 4-2: Schematic of fabrication processes

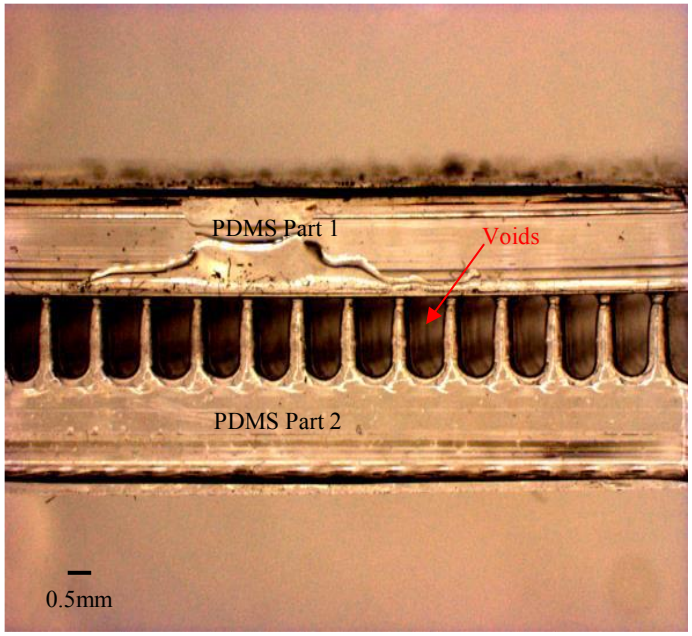

Figure 4-3: Image of cross-section view of single layer PDMS ferrelectret

4.2.3 Electrical charging

In order to achieve piezoelectricity properties, the fabricated PDMS ferroelectret was polarized by corona charging method. Figure 4-4 schematically shows the lab-built corona charging system applied in this work. A sample without electrode or only with a bottom electrode was placed onto a grounded metal holder. A needle, with its tip about $3 - 4$ cm above the sample surface, was connected to a high voltage supply. A metal grid, placed between the sample and the tip, at a distance about $0.5 - 1$ cm above the sample surface and with the same area as the metal holder, was also connected to a voltage supply. The grid was used only when the control of the surface potential was necessary.

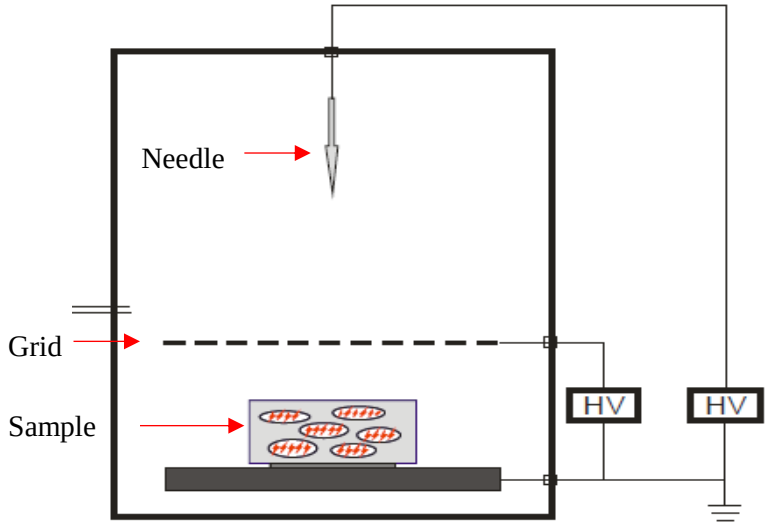

Figure 4-4: Schematic illustration of the tip-to–plane corona charging system

4.3 Experimental setup

4.3.1 Inspection of structure

Confocal laser scanning microscopy (CLSM or LSCM) is a technique for obtaining high-resolution optical images with depth selectivity [127]. The key feature of confocal microscopy is its ability to acquire in-focus images from selected depths, a process known as optical sectioning. Images are acquired point-by-point and reconstructed with a computer, allowing three-dimensional reconstructions of topologically complex objects. For opaque specimens, this is useful for surface profiling, while for non-opaque specimens, interior structures can be imaged. For interior imaging, the quality of the image is greatly enhanced over conventional microscopy because image information from multiple depths in the specimen is not superimposed. A conventional microscope observing as far into the specimen as the light can penetrate, while a confocal microscope only observe images one depth level at a time. In this work the LSM (LSM, Carl Zeiss NTS, Germany) was applied to inspect microscopic cellular structures. The related parameters of void structure can be measured easily. An optical microscope was also used to investigate the macroscopic cellular structures. The structures can be directly inspected.

4.3.2 Investigation of electromechanical property

4.3.2.1 Piezoelectric coefficients measurement

Piezoelectric coefficient d_{33} measurement was carried out using PiezoMeter Systems PM300. The system can provide a direct reading of d_{33}. It clamps the sample with electrodes and applies a low frequency force to it. After measuring the electrical signal from the sample and comparing it with a built in reference, the d_{33} value can be calculated. The measurement step is schematically illustrated in Figure 4-5. This device can provide a dynamic force which is variable from 0.05 to 0.50 N and a maximum static force of approximate 10 N which may be adjusted with different force head units with non-standard suspension. The frequency range of the applied dynamic force can vary from 30 to 300 Hz. The sample was placed on the bottom metal sample holder and then the top metal sample holder applied the static force. The moveable shaker which was fixed under the bottom holder provided the dynamic force. The magnitude and frequency of the dynamic force can be adjusted at the PM300 control panel and the value of piezoelectric coefficient d_{33} is directly displayed on the screen. For this measurement, the standard measurement setting was a dynamic force of 0.25 N, static force of 10 N and frequency of 110 Hz.

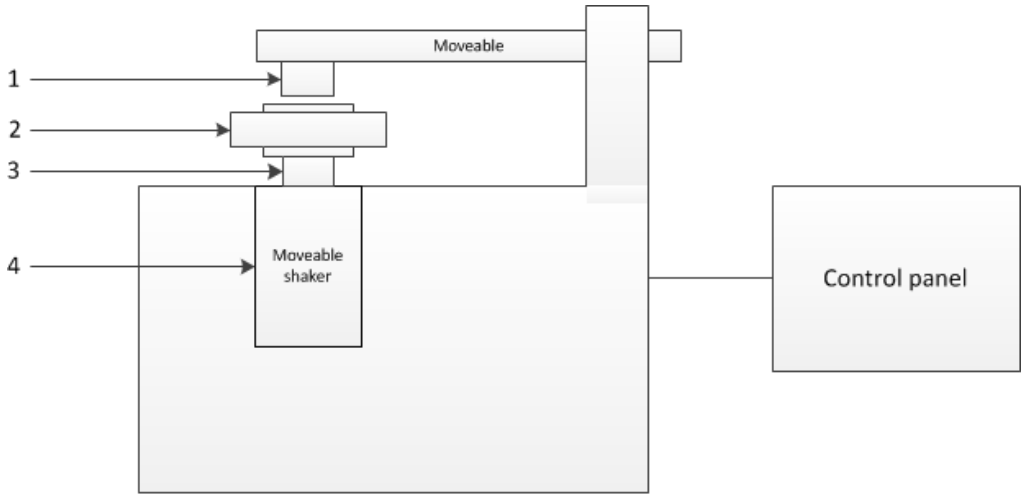

1. Moveable Top sample holder
2. Sample with electrode on both sides
3.Bottom sample holder
4. Moveable shaker

Figure 4-5: Illustration of the PM300 system for piezeoelectric coefficient d_{33} measurement

4.3.2.2 Investigation of energy harvesting capability

To investigate the capability of energy harvesting, an Instron electrodynamic instrument (ElectroPuls E1000, Instron Ltd) was used to apply a known force to the test sample. The maximum dynamic force this equipment can produce is 1000N and it can provide several types of compressive force including square wave force, sinusoidal force and triangular wave force. The frequency of the compressive force applied on the test samples can vary from 0 to 100Hz. These parameters can be modified in the control software. The sample was placed in the Instron and electrically insulated from the equipment with a piece of paper. The area of the sample holders which were used to apply the compressive force was 7cm^2. The output voltages of the PDMS ferroelectret under compressive force were recorded using an oscilloscope. In order to calculate the output energy from the voltage signal, the measurement data were transferred from the oscilloscope to a computer and analysed. The root mean square voltage of a periodic voltage signal can be calculated by:

$$V_{rms} = \sqrt{\frac{1}{n}\sum_{a=1}^{n} {V_a}^2} \tag{4-1}$$

Where V_a is the original voltage,

Then the average output power can be calculated as:

$$P_{avg} = {(V_{rms})^2}/{R} \tag{4-2}$$

Where R is the output resistance,

The V_{rms}value is the effective value of an AC voltage. It is the equivalent steady DC value which gives the same meaning.

4.4 Investigation of 3D printed PDMS ferroelectret

4.4.1 Inspection of cellular structure

The realised geometry of the void inside the PDMS ferroelectret by CLSM is illustrated in Figure 4-6. From the figure, it can be observed that the realised dimensions of the void had are slightly different from the desired structures especially at the top and bottom of the void. The reasons causing the difference include the precision of 3D printer and the surface tension of the mould material. The cross-section view for the middle and end of the bounded sample by optical microscope is shown in Figure 4-7 and Figure 4-8, respectively. It is found that there are some gaps between the two bonded parts in middle of the PDMS ferroelectret. These gaps affect the sealing of the ferroelectret to some extent.

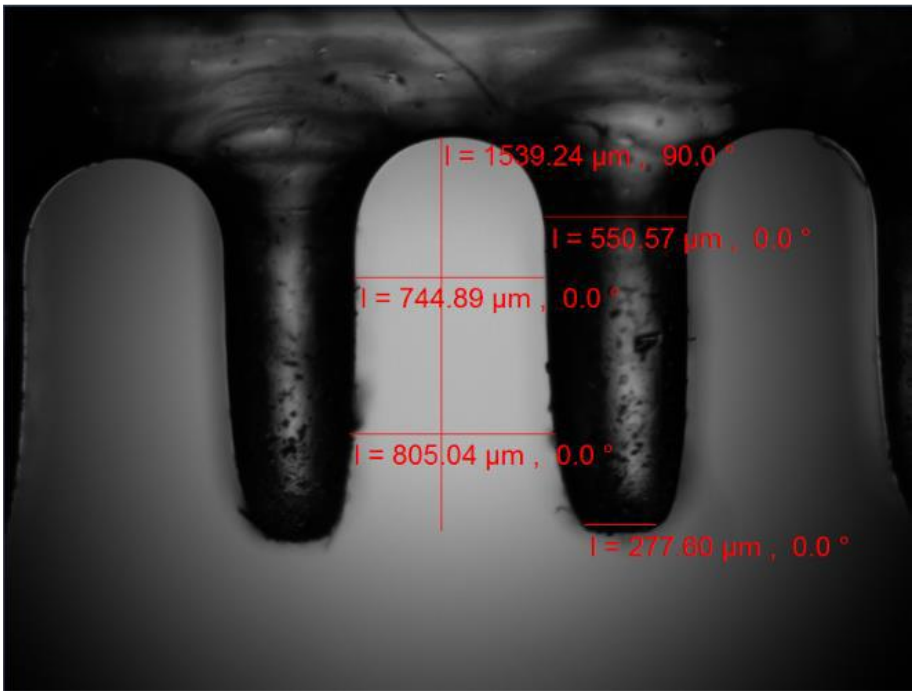

Figure 4-6: The LSM image of cross section view of the realised voids

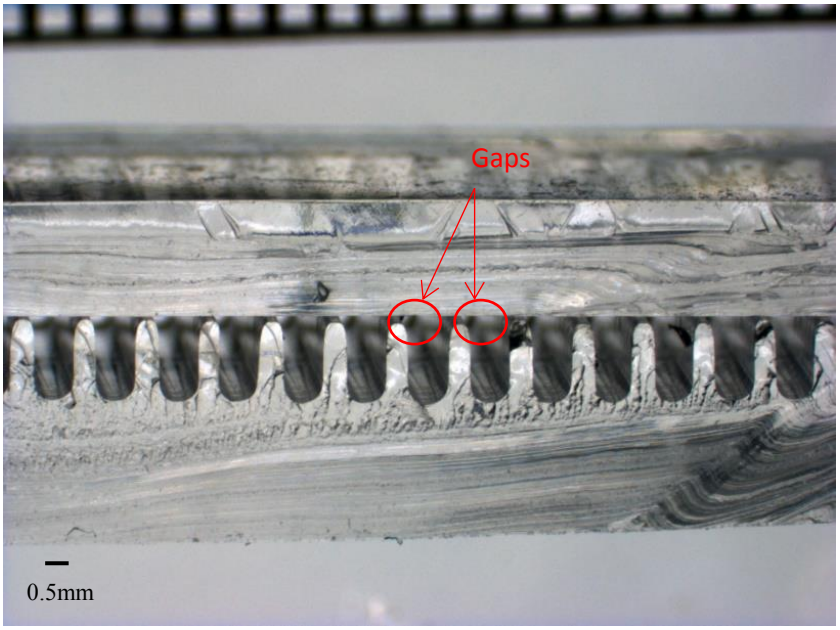

Figure 4-7: The optical microscope image of cross section view for middle area of ferroelectret

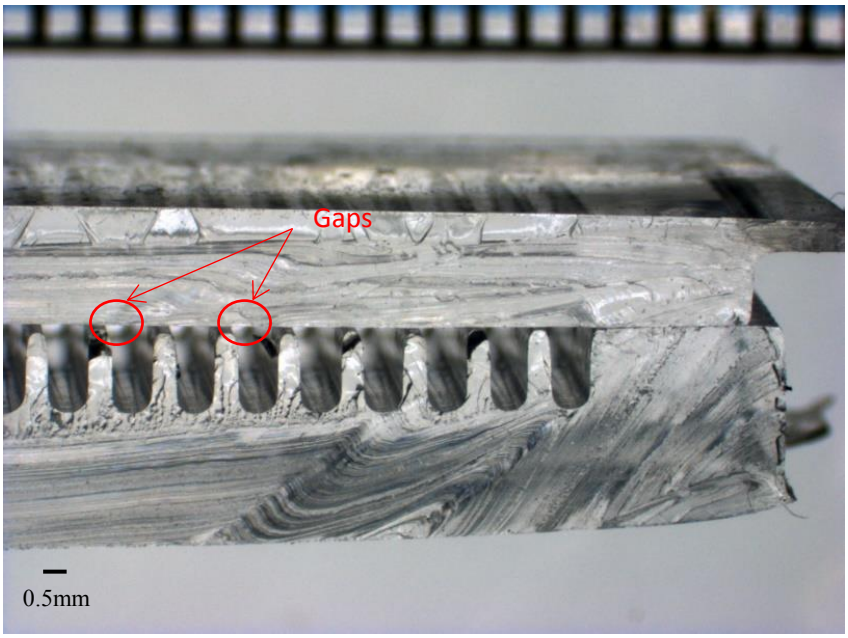

Figure 4-8: The optical microscope image of cross section view for end area of ferroelectret

4.4.2 Investigation of electromechanical properties

4.4.2.1 Long term piezoelectric coefficient measurement

The piezoelectric coefficient d_{33} of PDMS ferroelectret was measured by using PiezoMeter System PM300. For long term testing, all samples were stored at room temperature and normal atmospheric condition. In this experimental measurement, five samples for each structure are under investigated. For each samples measurement, it is measured in different positions. Figure 4-9 shows the measured piezoelectric coefficients of the three PDMS structures over a month period. The error bar in this figure indicates the variation of piezoelectric coefficient during measuring a single PDMS sample at different positions. The variation of measured piezoelectric coefficient for different samples with the sample structure is less than ±2 pC/N. It is found that the piezoelectric coefficients drops to about half of the initial value in the first 48 hours and reduces slowly after one week. After the first week, the piezoelectric coefficients of the structure 1 PDMS, the structure 2 PDMS and the structure 3 PDMS ferroelectret stabilised at around 20 pC/N, 10 pC/N and 7 pC/N, respectively. The issue of short life-span can potentially be solved by the deposition of extra semi-crystalline polymers or dielectric nanoparticles on void surface. As shown in Figure 4-9, the PDMS ferroelectret with lower sr_1 can achieve higher piezoelectric coefficient d_{33}. The thin PDMS ferroelectret presents higher piezoelectric coefficients than the thick one despite of the same structure ratios. The predicted piezoelectric coefficients d_{33} by ANSYS based on these structure ratios were around 100 pC/N (sr_1=0.4) and 70 pC/N (sr_1=0.5). There was a difference between the ANSYS simulation results and the practical results. The possible reason is that the total thickness of film might affect the surface charge density during corona charging. The thin ferroelectret can generate higher electric field during corona charging, which results an enhanced charge density.

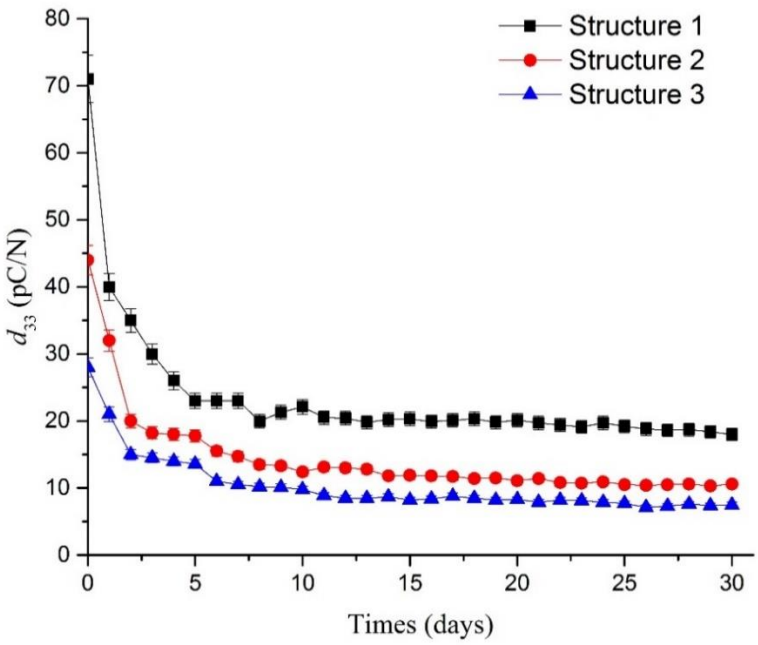

Figure 4-9: Measured piezoelectric coefficients of three PDMS structure over a month period

4.4.2.2 Energy harvesting performance

For the energy harvesting testing, all samples were recharged on the day before the testing. The output voltage of the ferroelectret PDMS film under compressive force takes the form of a voltage pulse as shown in Figure 4-10. Form this figure, the maximal peak voltage after measured at 1 hour and 100 hours after polarization are 0.9 V and 0.48 V, respectively. Thus device voltage is reduced by around 46.7 % after 99 hours. This reduction is related to the poor charge stability at the PDMS/air interface.

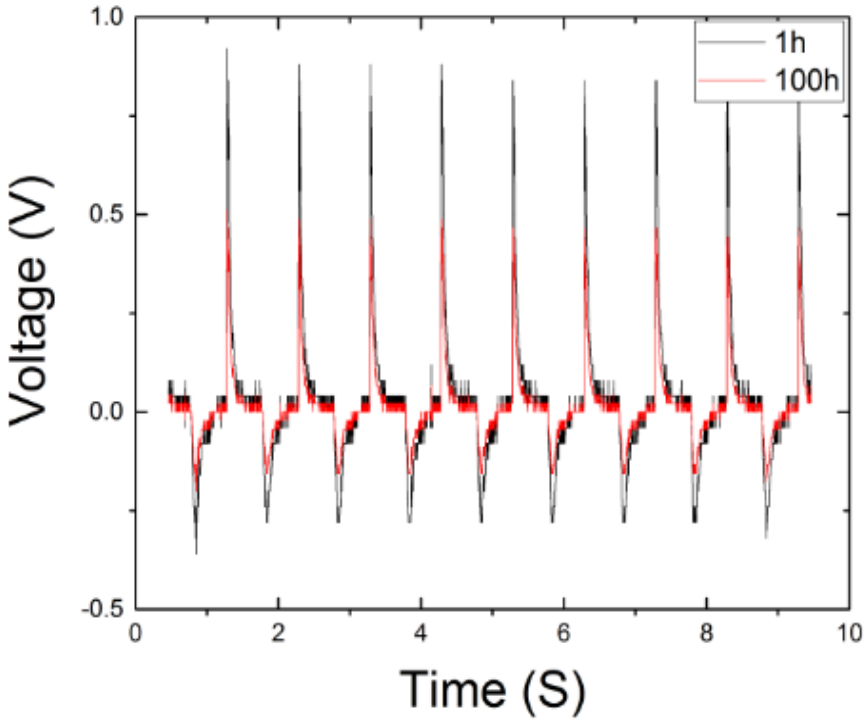

Figure 4-10: Measured voltage output of under compressive force with 1 Hz force frequency, 800N and 21MΩ load resistance

Figure 4-11 shows the peak output voltage of the three samples at different frequencies. The output peak voltage increase with increasing frequency and then start to decline after around 17 Hz. The optimized operating frequencies are close to the first order natural frequencies which are determined by the geometry of materials and their elastic properties. The thinner film have higher optimized operating frequency while the lower effective area ratio can reduce the frequency.

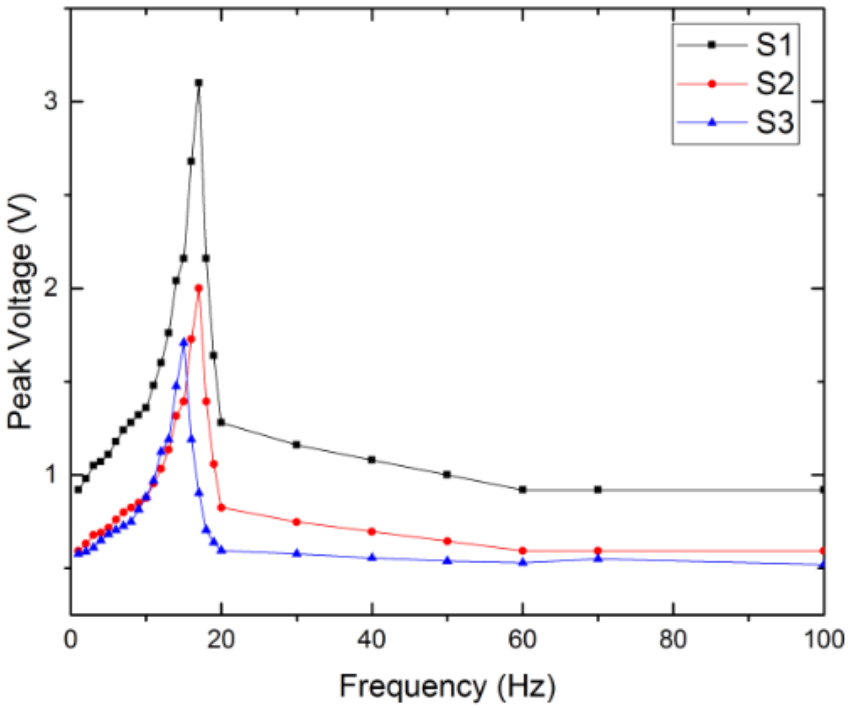

Figure 4-11: Measured voltage output of under compressive force at different frequency with 800N and 21MΩ loading resistance

Figure 4-12 shows the characteristic I-V curves of the three PDMS films under 800 N compressive forces with the frequency of 17 Hz, as a function of load resistance. From the figure, it can be observed that the maximum Peak power of 0.46 μW can be achieved from the structure 1 PDMS ferroelectret on 21 MΩ load resistance at 17 Hz. This is corresponding to area unit energy output of 0.115 μW/cm^2. These results prove that the lower effective area ratio and thinner PDMS ferroelectret can produce more output power, it is believed than a thinner PDMS ferroelectret will further enhance charge density.

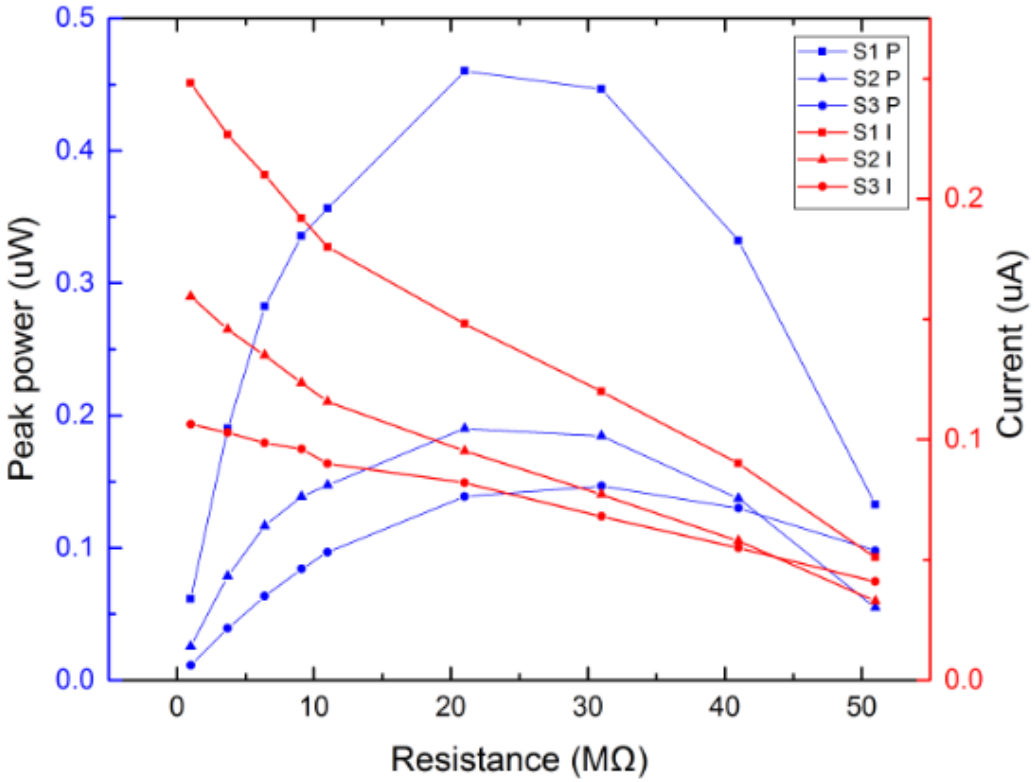

Figure 4-12: Power-resistance trace of PDMS ferroelectret under compressive force with 17 Hz force frequency, 800 N

Figure 4-13 shows the peak output voltage at different applied forces with the frequency of 17 Hz and load resistance of 21 MΩ for these three samples. The output voltage steadily increases with increasing applied force and the maximum peak voltage is achieved at 800N for these samples.

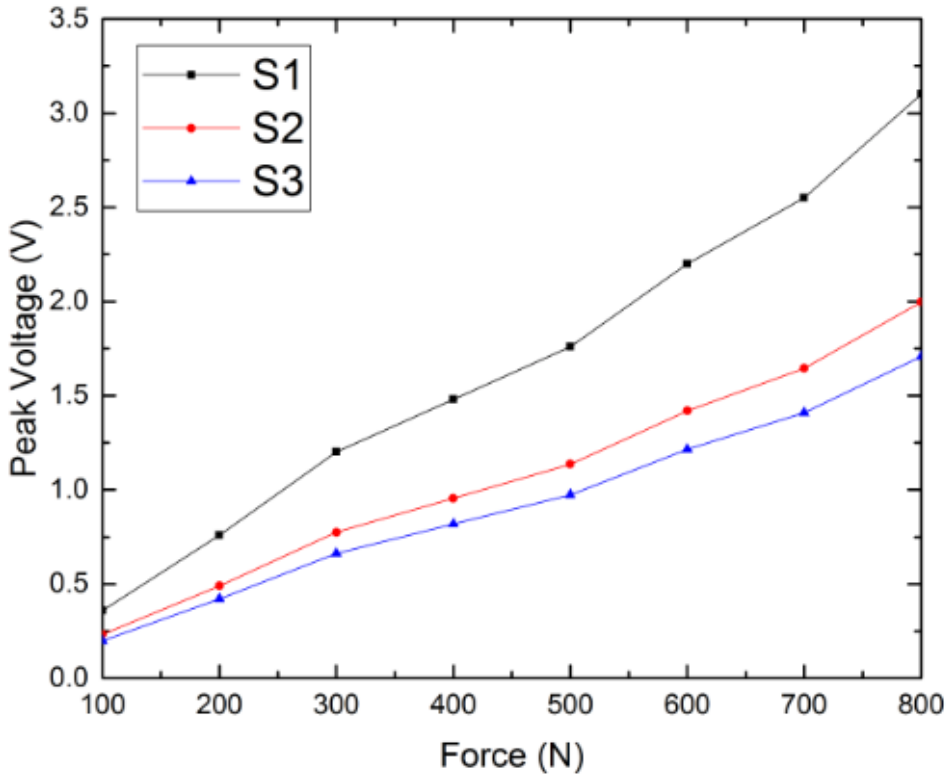

Figure 4-13: Measured voltage output of under compressive force at different force with 17 Hz and 21 MΩ loading resistance

4.5 Conclusions

In this chapter, the long term charge stability, electric charging behaviour and energy harvesting capability of PDMS ferroelectret fabricated using 3D-printed moulding were investigated.

The practical experiment revealed that the PDMS ferroelectret with lower sr_1 can generate higher piezoelectric coefficients d_{33} and the thinner PDMS ferroelectret based on the same structure ratio can achieve higher piezoelectric coefficients d_{33}. The designed PDMS ferroelectret fabricated using 3D printed moulding presented a maximum piezoelectric coefficient d_{33} of 71 pC/N. The optimized PDMS ferroelectret with the size of 2 cm x 2 cm generates maximally 3.1 V, 0.46 μW when connected to a 21 MΩ resistive load under a square compressive force of 800 N and 17 Hz, corresponding to area unit energy output of 0.115 μW/cm^2. Comparing the measurement results with the simulation results, both results show the same trend of piezoelectricity changes with varying the ratio sr_1.

To improve the piezoelectric coefficients d_{33} and energy harvesting performance of PDMS, scaling down its thickness of is a possible solution based on the analytical model. However, due to limitation of the 3D-printed moulding the improve structure cannot be fabricated. It is difficult to further scale down the PDMS structure utilizing this fabrication approach. Therefore micro fabrication methods were also considered.

5 PDMS Ferroelectret Fabricated by Silicon Mould Method

5.1 Introduction

In the previous chapter, PDMS ferroelectret with macro cellular structure has been fabricated using 3D printed moulding and its performance has been evaluated. In this chapter, the fabrication processes for micro scale parallelogram and rectangular void PDMS ferroelectrets with different structure ratio are described and then its energy harvesting performance is evaluated. The PDMS ferroelectret with micro scale structure is fabricated by silicon moulding method. The silicon mould is fabricated using MEMS micromachining processes and exploits the crystalline structure of the silicon to achieve the parallelogram structure simulated in Chapter 3.

5.2 Fabrication process

5.2.1 Silicon mould fabrication process flow

Southampton Nano-fabrication Centre (SNC) have the facility to support a wide range of MEMS device fabrication. Two types of wafers are used in this research: the <100> wafer has a diameter of 150 mm with thickness of 575 μm; the <111> wafer has a diameter of 100 mm with thickness of 525 μm. The fabrication processes used include:

- Plasma-enhanced chemical vapor deposition (PECVD): SiO_2
- Photolithography
- Inductively Coupled Plasma (ICP) Etching: SiO_2 and Si
- KOH Wet etching

The first step of the process is to deposit thin layers of silicon dioxide (SiO_2) on the top of device wafer using PECVD. Secondly, a layer of positive resist is deposited on top of silicon dioxide layer by spin coating. These resist layers are patterned and developed using standard

photolithography. Next, the oxide that is not protected by the remaining resist is removed using ICP etching. The oxide layers act as the mask for removing the silicon that is not protected. After removing all resists, the wafer is processed inside a hydrofluoric acid (HF) to remove the remaining silicon dioxide layer. In addition, for <111> wafer, a potassium hydroxide (KOH) process is used for further etching before removing the SiO_2 layer. The schematic of rectangular void silicon mould and parallelogram void silicon mould fabrication process are shown in Figure 5-1 and Figure 5-2, respectively.

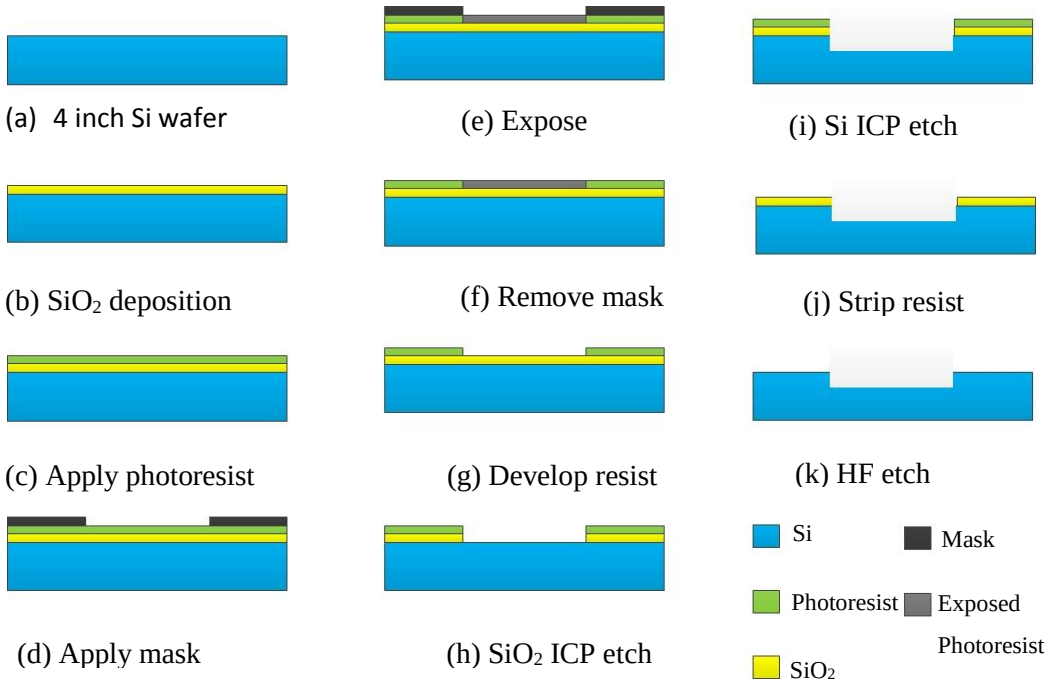

Figure 5-1: Schematic of rectangular void silicon mould fabrication process

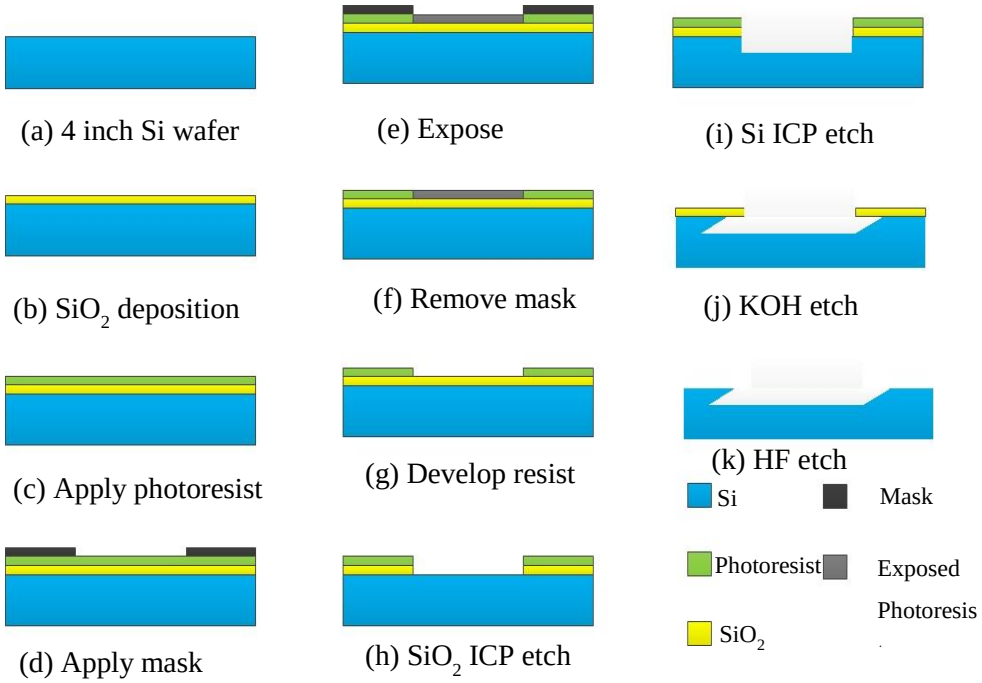

Figure 5-2: The schematic of parallelogram void silicon mould fabrication process

5.2.2 Photomask design

The first step of silicon mould fabrication is to design the photo-mask. Optical lithography is the standard method used to transfer the design in photo-mask onto the wafer. The mask is aligned to the photoresist-coated wafer and exposed by UV radiation inside a mask-aligner/exposer tool. The mask for silicon mould is 5 inches square to accommodate 4 inche diameter silicon wafer. The design contains two types of geometric design to fabricate rectanglular and parallelogram void which is shown in Figure 5-3.

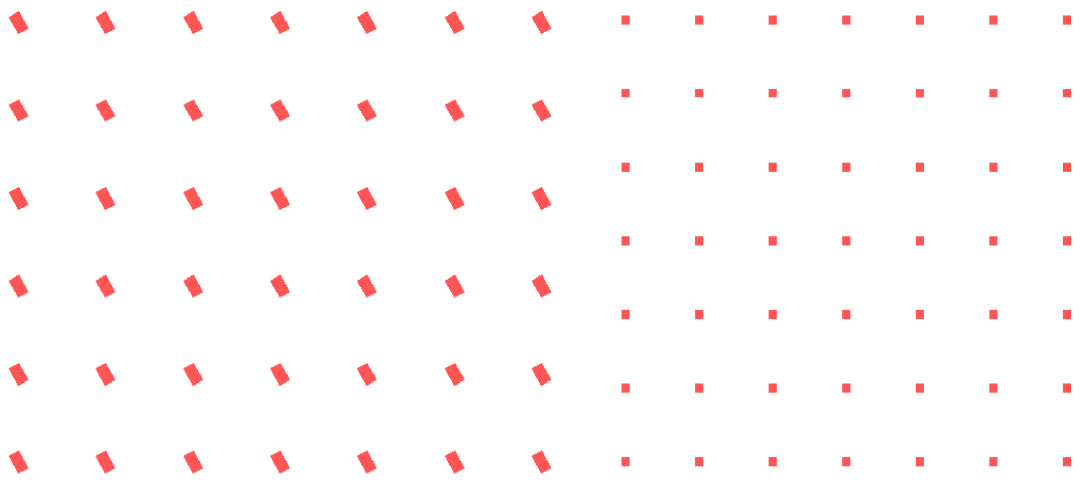

(a) (b)

Figure 5-3: The mask design for the fabrication of in silicon mould for (a) parallelogram void ferroelectret (b) rectangular void ferroelectet

5.2.2.1 Plasma-enhanced chemical vapor deposition (PECVD)

Plasma-enhanced chemical vapor deposition (PECVD) is a process used to deposit thin film from a gas state to solid state on a substrate. Chemical reactions are involved in the process, which occur creation a plasma of the reacting gases. This process was done using the OIPT SYS100 based capacitive PECVD reactor as shown in Figure 5-4.

Figure 5-4: The image of PECVD machine in SNC

The PECVD procedure can be described in following steps:

- Setting up: Checking the pressure of CDA and utility N_2 regulator. Ensuring the fluid level of the heater is not below the operating level and turn it on then set it 90C. Checking the dry and turbo pumps are operating and showing no fault in control system.
- Creating recipes: Selecting the standard silicon dioxide PECVD recipes. Adjusting the duration of process. The thickness of SiO_2 layer is determined by the process duration.
- Loading wafer: Adjusting the size of wafer holder to match the process wafer. Placing the wafer in the etching chamber at appropriate location.

To fabricate different silicon moulds, the duration of the process should be set differently. The thickness of resulted PECVD oxide can be measured using the ellipsometer. The ellipsometer measures the refractive index of oxide layer with different wavelength and then compares the results with the built-in standard model to obtain the thickness of that oxide layer. The detail of duration are summarised in table 5-1.

Table 5-1: A summary of the duration of PECVD for different depth mould and the resulted depth

Target void depth	Duration of PECVD process	Target thickness of SiO_2	Real thickness of SiO_2
30 um	30 mins	2000 nm	2088 nm
40 um	37.5 mins	2500 nm	2540 nm
50 um	45 mins	3000 nm	3080 nm

5.2.2.2 Photolithography

List of process used

- Spin-coating (Brewer spin coater) and Hotplate for photoresist deposition
- Photo mask aligner (EVG620) for ultraviolet exposure

List of materials used

- 6 inch <100> silicon and 4 inch <111> silicon wafers
- Positive photoresist: AZ9260
- Developer solution: AZ400K
- Wafer primer

The first step of photolithography is photoresist deposition. Before coating the photoresist, the Si-SiO_2 wafer should be coated with a layer of wafer primer to enhance the adhesion of the spin-coated photoresist to the wafer. The wafer primer is baked on hot-plate for 120 s at 120 °C. Then a 6 µm layer of positive photoresist AZ9260 is deposited on the top of the oxide layer using spin-coating. This resist is baked on hotplate for 120 s at 110 °C to be hardened. Then, the wafer is positioned in the mask aligner along with the photomask to expose the photoresist under UV light. The exposed resist is developed in AZ400K solution for 6-7mins. The step details are shown in table 5-2.

Table 5-2: A summary main parameter for photolithography step

No	Step	Material	Method	Thickness
1	Deposit	Wafer primer	• Spin coating • Hotplate	1 µm
2	Deposit	Positive resist AZ9260	• Spin coating • Hotplate	6 µm

3	Removal	Positive resist AZ9260	• Expose to UV light under the photo-mask in a mask aligner • Develop in developer AZ400K	6 µm

5.2.2.3 Inductively Coupled Plasma (ICP) Etching

In order to generate the device pattern on the wafer, plasma etching tools such as Inductively Coupled Plasma (ICP) is deployed. ICP uses parallel plate of opposite charge to drive the ions to the designated plate where the wafer is located and then these ions start bombarding the wafer to etch away any exposed oxide. ICP introduces a radio frequency (RF) powered magnetic field which is capable of generating very high-density plasma. The capacitor plates keep the etching process anisotropic while the magnetic field induces a high-density source of ions, hence increasing the etch rate and also providing a high aspect ratio and uniformity across the wafer.

After Photolithography process, the exposed oxide layer is etched using ICP for 5-6 mins. The reaming oxide layer act as a mask for Si etching. The etching depth is control by the duration of Si-ICP etching process. The detail of duration for each sample are summarised in table 5-3.

Table 5-3: A summary of main parameter for ICP etching

No	Step	Material	Method	Duration
1	Removal	Oxide (SiO_2)	Etch using ICP	5-6 mins
2	Removal	Silicon (Si)	Etch using ICP	30, 40, 50 mins

5.2.2.4 Wet etching

List of processes used

- Wet etch: hydrofluoric acid (HF)
- Wet etch: potassium hydroxide (KOH)

List of materials used

- 6 inch <100> silicon and 4 inch <111> silicon wafers
- HF acid
- KOH

For the 6 inch <100> wafers, after striping the remaining resist, the final step is remove SiO_2 by HF etching. For HF etching step, 6 inch <100> wafers are dip etched in HF for 10 minutes to remove surface oxide layer. For the 4 inch <111> wafer, to create parallelogram void, an additional KOH etching process is applied before removing the SiO_2 layer. The cause for this shape is due to that fact that KOH is an anisotropic etchant that etches the silicon substrate at rates preferential to the various crystal lattice planes. KOH etches quickly in the (100) and (110) directions and slowly in the (111) direction. Figure 5-5 is the top view of the etch cavity shape for the rectangle mask windows [137]. After KOH wet etching, the rectangular windows became hexagon shaped. Its cross section is a parallelogram with an obliquity of 70.5° [137]. The length and width of the silicon line are determined by the dimensions and positions of the mask windows [137].

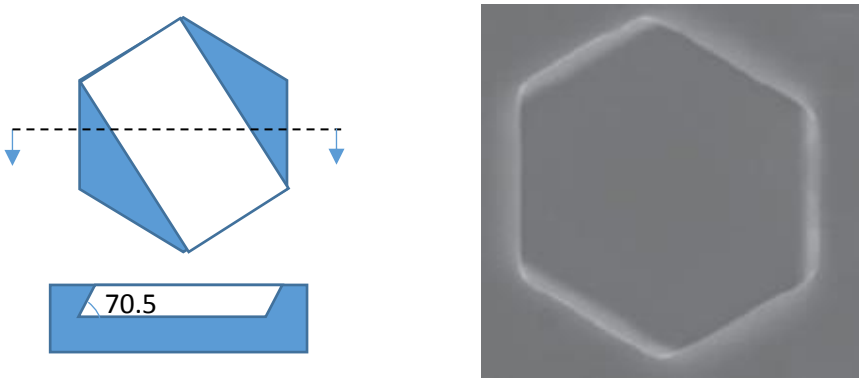

(a) (b)

Figure 5-5: (a) Top view of the etch cavity shape for the rectangular mask windows; (b) SEM top view of the fabricated parallelogram mould [137]

To optimise the KOH etching process, the composition of the KOH/H_2O solution must be considered. The amount of KOH in the solution will impact both the etching rate and the selectivity of the etching rate with respect to the silicon crystal orientation (i.e. etch rate in the direction vs. etch rate in the direction). An ideal etching would offer a reasonably fast etching rate with acceptable selectivity. The etching temperature also impacts the etching rate and selectivity. The <100>/<111> selectivity- data from literature is shown in Figure 5-6 [138]. In this set of experiments, the 4 inch <111> wafer are etched in KOH solution with 37.5% concentration at a fixed temperature of 80°C for 20 minutes. After KOH etching, the 4 inch <111> wafers are dip etched in HF to remove the SiO_2 layer.

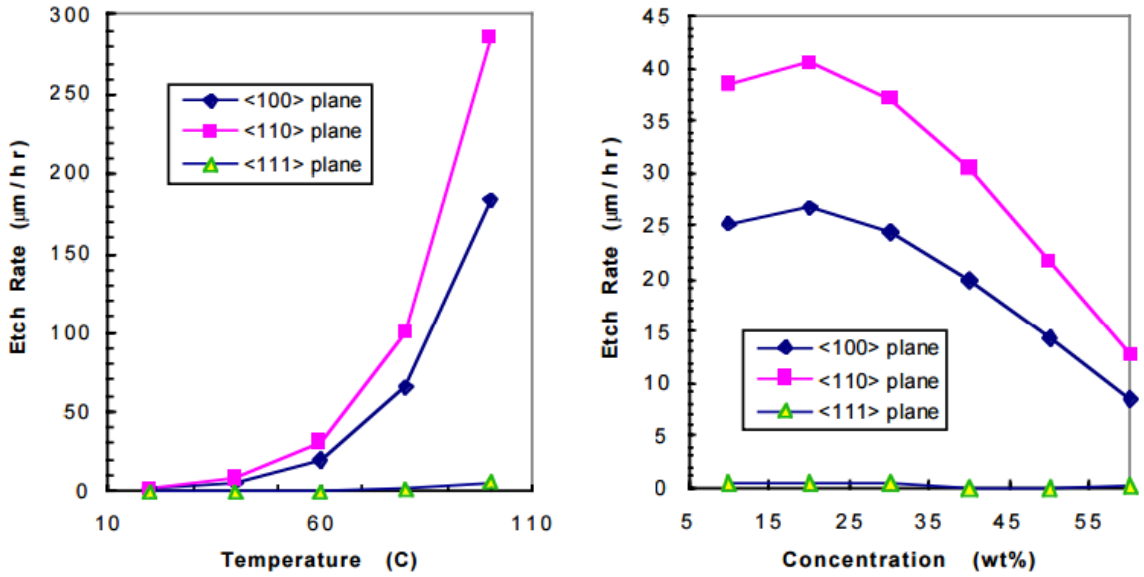

Figure 5-6: Silicon etch rate in KOH vs. Temperature and Concentration (left) Silicon etch rate as a function of temperature at fixed concentration of 40% (right) Silicon etch rate as a function of concentration at fixed temperature of 60 °C [138]

5.2.3 PDMS casting and bonding

A thin layer of PDMS is called a PDMS membrane. The PDMS membrane is generally fabricated on wafer which using a spin coater to the wafer has to be cleaned by acetone before fabricating the PDMS membrane. To remove all moisture on the surface the wafer was baked in oven for 15 mins at 120 °C. After this step, the silicon moulds were exposed to a silane vapour for 1 hour to be coated with a thin layer of trichloro(1H,1H,2H,2H-perfluorooctyl)silane (Sigma Aldrich, MO, USA). Liquid PDMS and curing agent (Sylgard 184 from Dow Corning, MI, USA) were mixed at a 10:1 weight ratio and then the mixture was degassed in a vacuum desiccator. The degassed PDMS was poured into the fabricated silicon moulds which is placed in a spin coater to fabricate the PDMS membrane. This membrane was baked in oven for 20 minutes at 80 °C for it to be hardened. The thickness of PDMS membrane is determined by the spin coating speed and the duration which is shown in Figure 5-7 [139]. To achieve investigate the influence for the spin coating duration, the spin-coating speed was fixed at 1000 rpm.

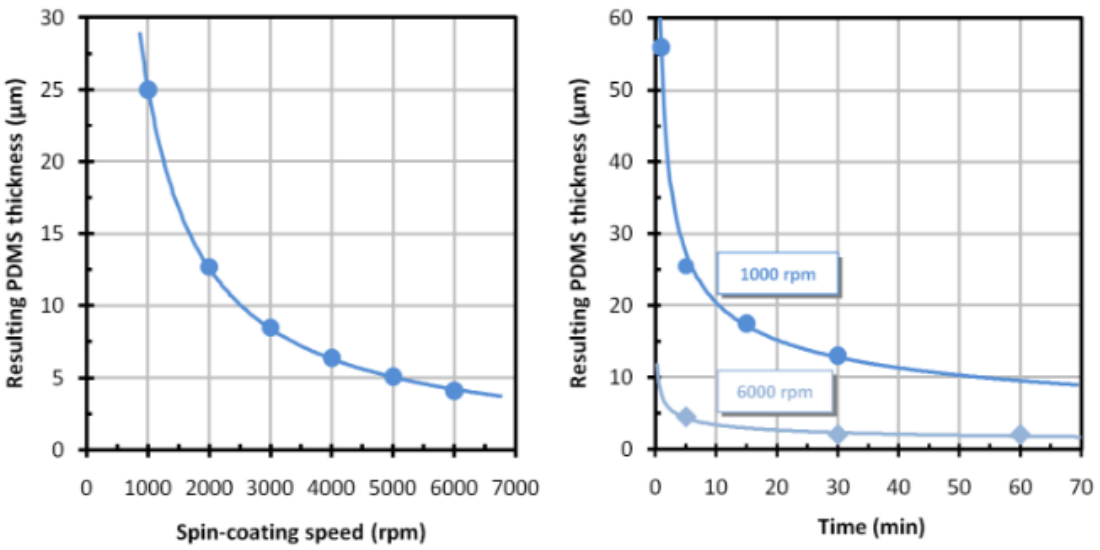

Figure 5-7: Dependence of PDMS layer thickness for PDMS ferroelectret as a function of spin coating speed for a 5 min spin coating time (left) and as a function of spin-coating time for two given spin-coating speeds (right) [139]

Due to the fact that membrane is difficult to handle, the wafer was immersed into water so that the PDMS membrane can be released from the wafer.

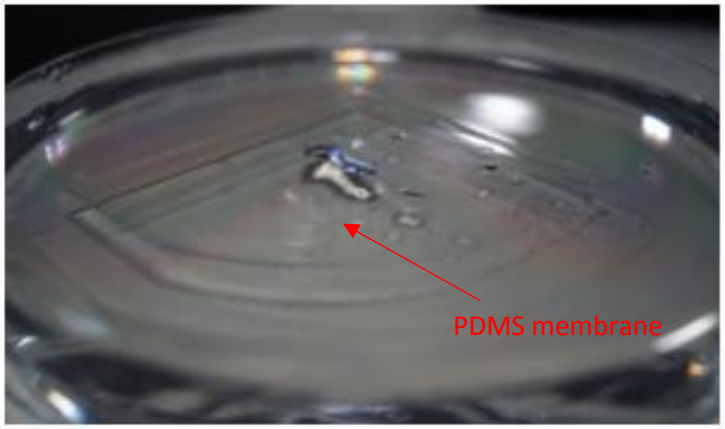

Figure 5-8: The image of PDMS membrane

The 6 inch and 4 inch PDMS membrane was cut into several pieces each 3 cm square. In the second method, after detaching the polymerized PDMS from the moulds, an oxygen plasma treatment was applied on the patterned surface of the PDMS layer and the smooth surface of

the other PDMS layer (Femto Asher, Diener, Germany, 30 S at 35-40W) and then bonded together. The bonded PDMS was then baked in oven at 80 °C for 1 hour while applying a 1 kg mass on the top to improve the bonding effect.

5.3 Experiments and results

To investigate the effect of void shape on the piezoelectric properties of ferroelectret rectangular void and parallelogram void structure having the same effective area ratio were fabricated using in silicon moulds. The top view of the rectangular void structure and the parallelogram void structure is a square shaped and a hexagon shaped, respectively. In order to achieve the same effective area ratio, the area of hexagon should be equal to the area of the square. Therefore, there is a difference between rectangular and parallelogram structure in designed void width and designed void gap parameter. To evaluate the piezoelectric properties of ferroelectret at lower effective area ratio, the three void structures with different effective area ratio (0.25, 0.16 and 0.0625) were designed. As mentioned in section 2.5.1, the minimum required breakdown electric voltage and electric field are achieved at gap distances from 20 to 50 µm; also considering with the feasibility of MEMS fabrication process, three silicon moulds with different depth (30/40/50 µm) were fabricated to evaluate the effect of the thickness ratio. A summary of the main parameters of the fabricated sample is shown in the table below:

Table 5-4: A summary of designed parameter for silicon mould

Void shape	Thickness ratio tr_1	Effect area ratio sr_1	Void Thickness	Void width	Void gap
Rectangular	0.4-0.8	0.25/0.16/0.0625	30/40/50 µm	50/75/150 µm	50 µm
Parallelogram	0.4-0.8	0.25/0.16/0.0625	30/40/50 µm	46.3/71.3/146.3 µm	53.7 µm

Repeating the PDMS casting and bounding processes, PDMS ferroelectret with different cellular structures were fabricated. Both of these samples were polarized by corona charging method. For this experiment, corona charging was applied at room temperature and normal atmospheric pressure. A corona-tip voltage of -25 kV was employed for 2 minutes.

5.3.1 Inspection of cellular structure

Figure 5-9 shows the image of the cross section image of the fabricated rectangular and parallelogram void ferroelectret membranes. From the figure, it can observed that the designed void shape is successfully fabricated by using the silicon moulding method.

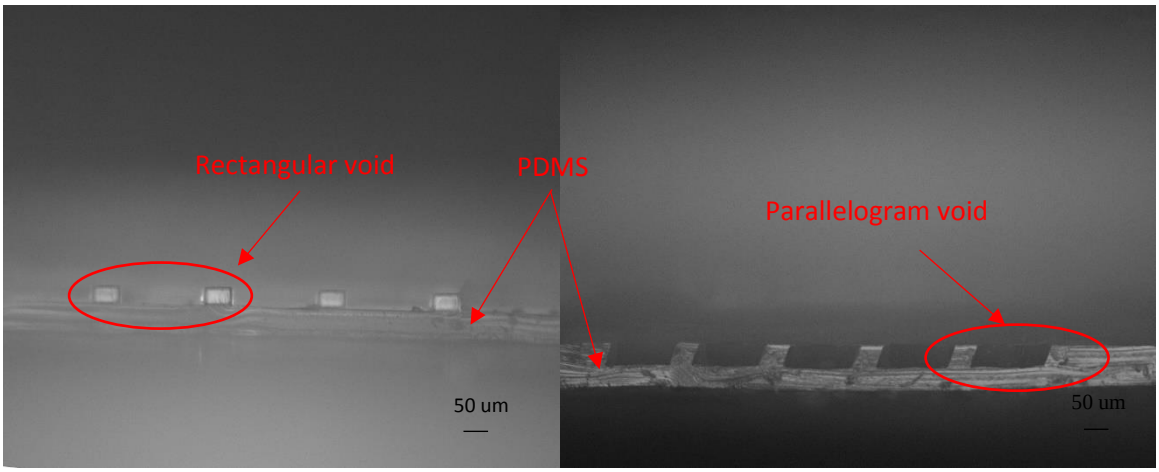

(a) (b)

Figure 5-9: The image of the cross section image for fabricated (a) rectangular void and (b) parallelogram void PDMS ferroelectret membrane

Figure 5-10 shows the image of the cross section image of multi-voids layer PDMS ferroelectret. It is found that the voids are not aligned vertically for both rectangular void and parallelogram void PDMS ferroelectret.

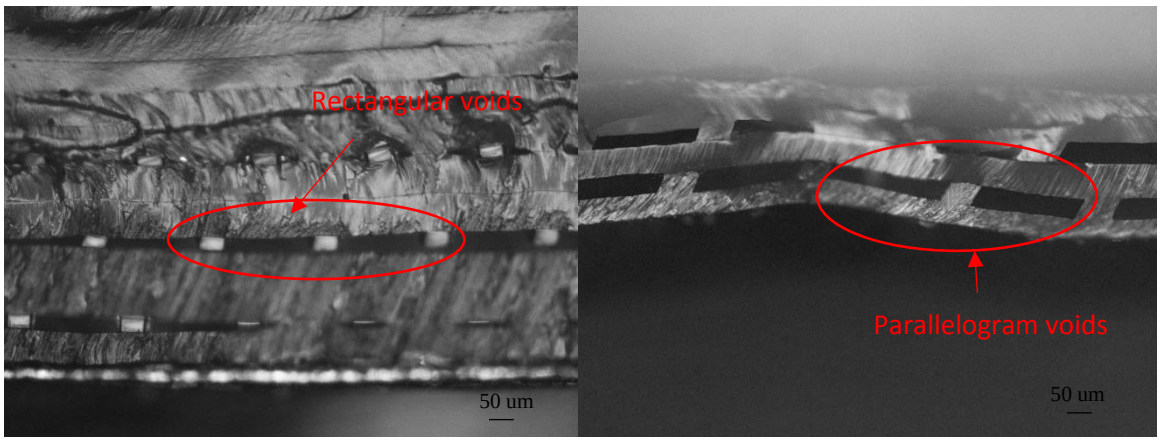

(a) (b)

Figure 5-10: The image of the cross section image for multilayer PDMS ferroelectret (a) rectangular PDMS ferroelectret (b) parallelogram void PDMS ferroelectret

5.3.2 Piezoelectric coefficients measurement

Piezoelectric coefficients d_{33} of the fabricated PDMS samples were measured using Piezometer Systems PM300. Results of the piezoelectric coefficient d_{33} varying with the thickness ratio for the PDMS ferroelectret with one void layer is shown in Figure 5-11. It is found that the piezoelectric confident d_{33} of both samples increase with the thickness ratio. The best piezoelectric properties among all samples are achieved around the thickness ratio of 0.8. It is also found that the effective area ratio does affect the resulting piezoelectricity. The structure with lower effective area ratio can achieve better piezoelectric properties. In addition, the PDMS ferroelectret with parallelogram voids present better piezoelectric properties than those with rectangular voids in one void layer PDMS ferroelectret.

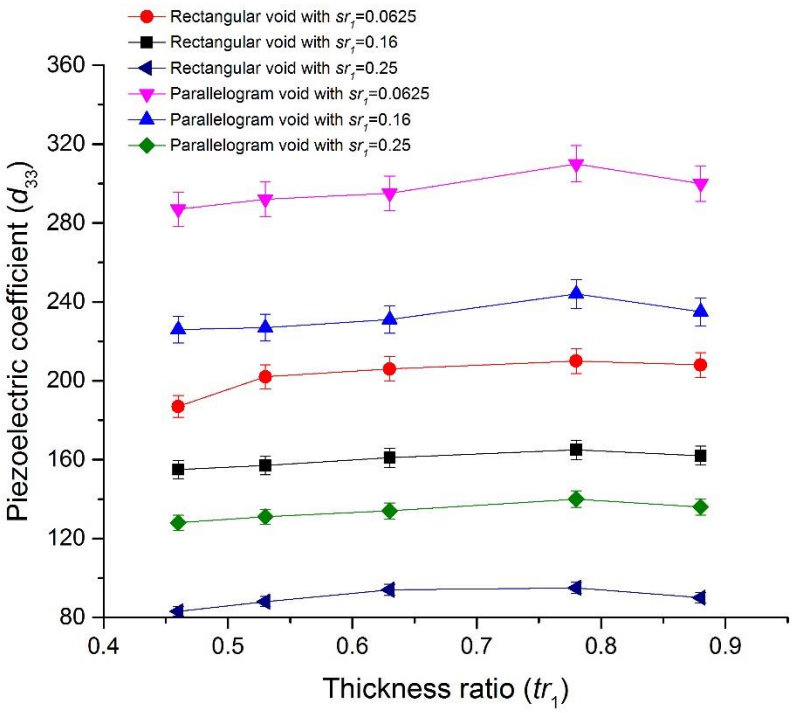

Figure 5-11: The measured piezoelectric coefficient varying with the thickness ratio for one void layer PDMS ferroelectret

Results of the piezoelectric confident d_{33} varying with the thickness ratio for PDMS ferroelectret with two and three void layers are shown in Figure 5-12 and Figure 5-13, respectively. For PDMS ferroelectrets with two void layers, the maximum piezoelectric coefficients d_{33} were achieved when thickness ratio is around 0.6. For three void layer PDMS ferroelectret, the maximum piezoelectric coefficients d_{33} were achieved around 0.55.

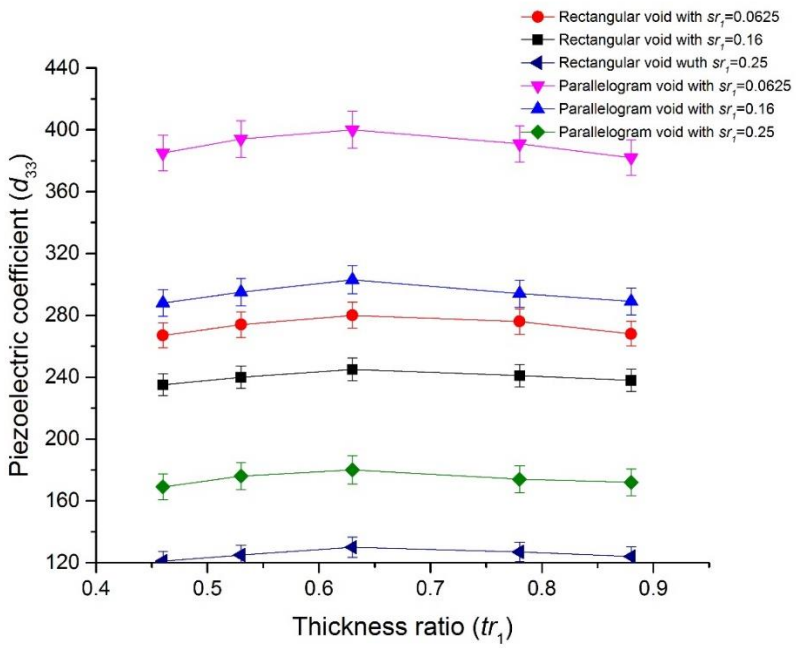

Figure 5-12: The measured piezoelectric coefficient varying with the thickness ratio for two void layers PDMS ferroelectret

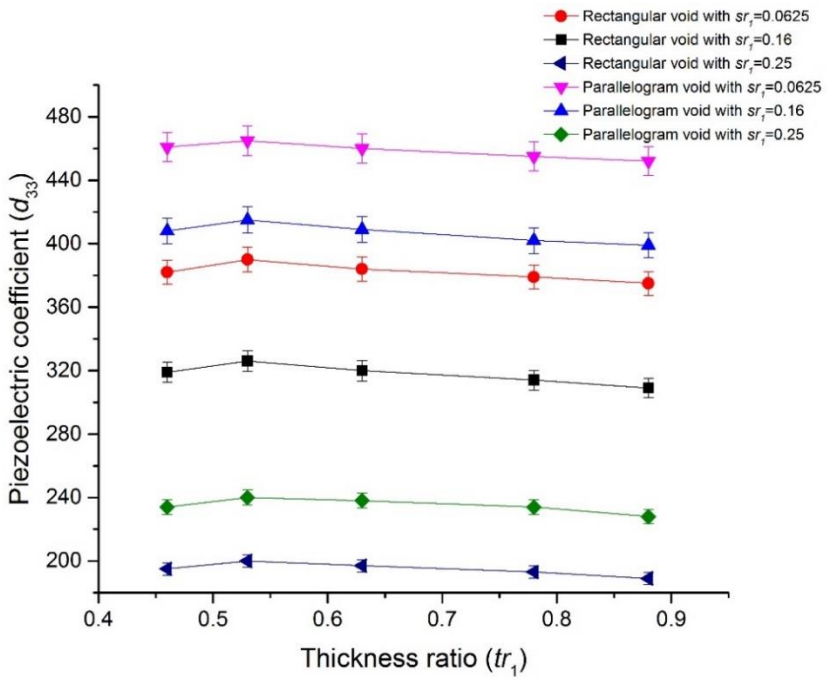

Figure 5-13: The measured piezoelectric coefficient varying with the thickness ratio for three void layers PDMS ferroelectret

With the number of void layer increasing, the variations of piezoelectric properties were shown in Figure 5-14. When stacking more void layers together, it is found that d_{33} of PDMS ferroelectret have a significant improvement up to 4 layers. The maximum piezoelectric coefficients d_{33} are achieved by 4-layer PDMS ferroelectret. When 5 or more layers are stacked, d_{33} does not increase any further. The reason for this phenomenon is that, with the number of void increasing, the void can be considered as distributing more and more away from the horizontal centerline of the ferroelectret. As mentioned at pervious ANSYS simulation in Section 3.3.4, the piezoelectricity properties can be enhanced by the off horizontal centerline ratio. For structures with more than 4 void-layers, the piezoelectric coefficients d_{33} remain almost constant or even decline slightly. While the number of void layer is more than 4, the influence of void distribution is decreased and the effective Young' modulus of the ferroelectret increase resulting in piezoelectricity properties reduced. Furthermore, the parallelogram structure also present higher piezoelectric properties for multi-void layers. The reason for that is the parallelogram void can produce larger deformation comparing with rectangle void.

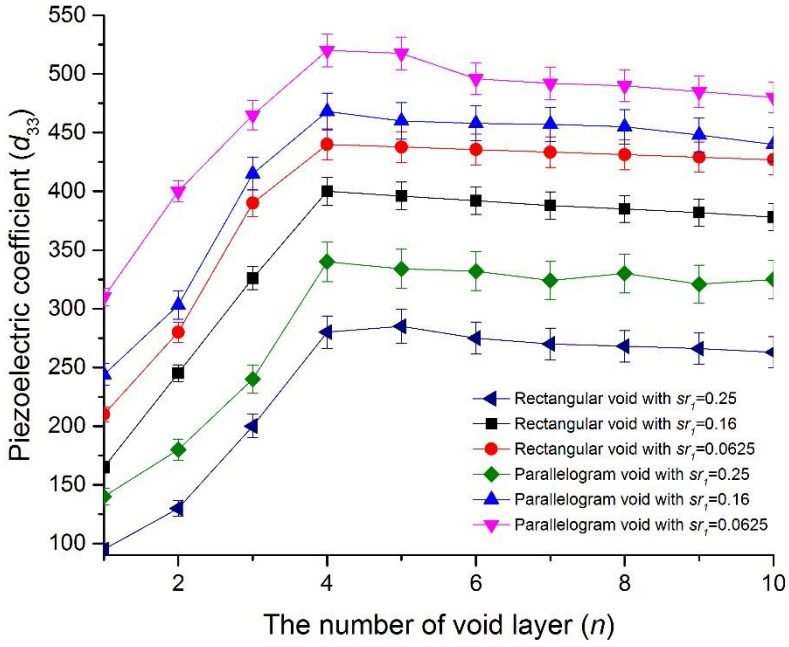

Figure 5-14: The measured piezoelectric coefficient varying with the number of void layers

For long term testing, all samples were stored at room temperature and normal atmospheric condition. Figure 5-15 shows the measure piezoelectric coefficients of these PDMS structure over a month period. Piezoelectric coefficients d_{33} were dynamically determined and the sample showed an initial d_{33} of 310 pC/N. It is found that the piezoelectric coefficient drops to about half of the initial value in 72 hours and remain a lower reducing rate after that. The measured d_{33} can be effected by the measurement positon, since the sample was removed from the sample holder after each measurement, consequently the measurements were not taken at exactly the same positon. In additions, during this one month measurement experiment, the experimental conditions, including temperature and humidity were not well controlled and were varying over time.

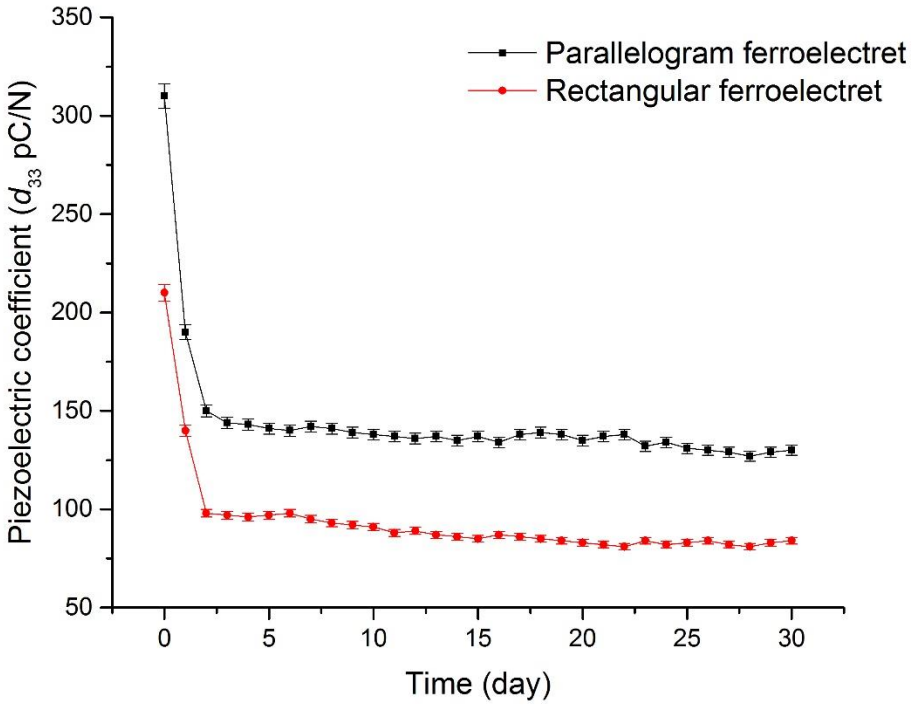

Figure 5-15: Measured piezoelectric coefficients of three PDMS structure over a month period

5.3.3 Investigation of energy harvesting performance

To investigate the energy harvesting performance of PDMS ferroelectret, the energy harvesting experiment carried on immediately after the sample polarization by corona charging. The four-layer parallelogram PDMS ferroelectret with the measured piezoelectric constant of 520 pC/N was selected as the testing sample. The size of the fabricated PDMS ferrolectret sample is 2 cm × 2cm. In order to use these samples for energy harvesting purpose, a thin layer silver conductive tape were stuck onto either side of the samples. To apply compressive force resembling human walking, an Instron electrodynamic instrument (EletroPuls E1000, Instron Ltd) was used to quantify the applied forces. The average step frequency of human walking is in range of 0.4 to 1.45 step/s [128-130]. To simulate three different human walking conditions, three types of compressive forces were applied and their wave forms are shown in Figure 5-16 to Figure 5-18. Each walking function has the maximum force of 800 N. The step frequency of slow walking mode was set as 0.4 step/s, the transition time of the applied force from 0 to 800 N was 0.24 s and the duration of the maximum force on the sample was set to 1 s. For the normal walking mode, the step frequency were 0.8 step/s, the transition time of the applied force was 0.15 s and the duration of the maximum force was 0.5 s. For the fast walking model, the step frequency, the transition time and the duration of the maximum force were 1.4 step/s, 0.1s and 0.3s, respectively. The output voltages of the PDMS ferroelectret under there compressive forces were recorded using an oscilloscope with internal input impedance 1 MΩ (TDS2014, Tektronix UK Ltd).

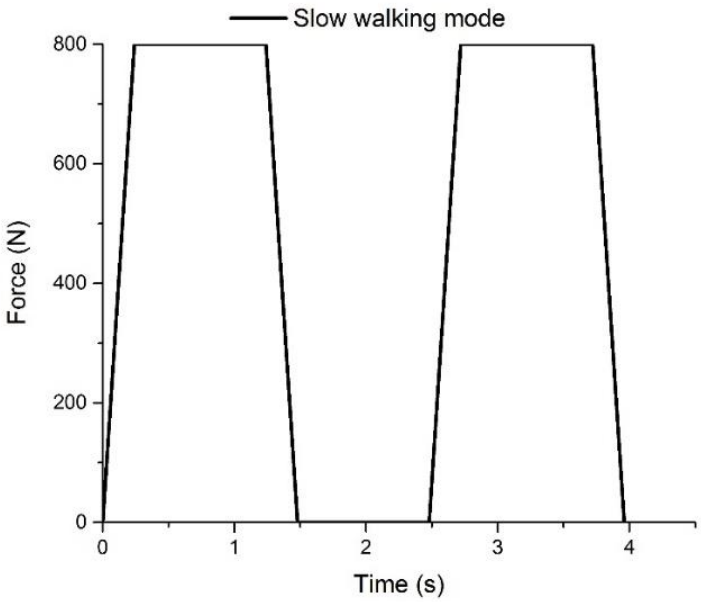

Figure 5-16: Waveform of applied compressive force at slow walking mode

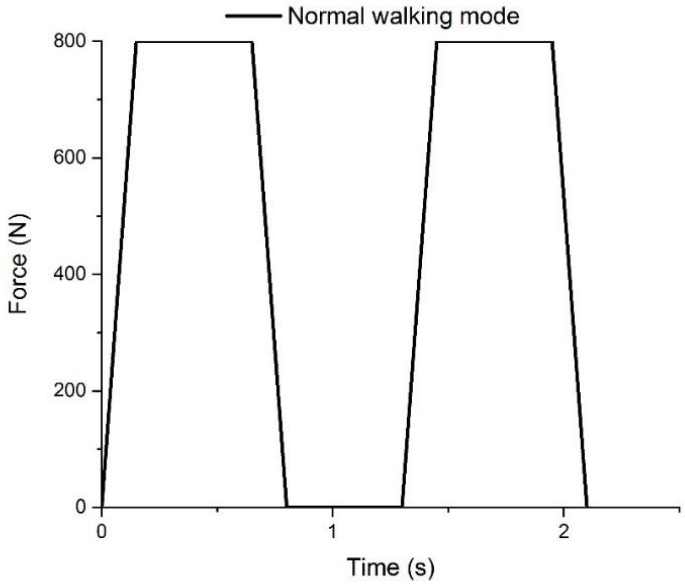

Figure 5-17: Waveform of applied compressive force at normal walking mode

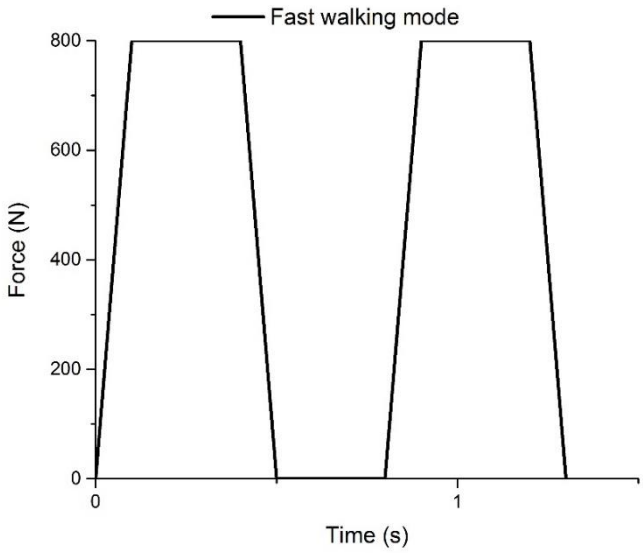

Figure 5-18: Waveform of applied compressive force at fast walking mode

The output voltage of the PDMS ferroelectret film under compressive force takes the form of a voltage pulse as shown in Figure 5-19. The material is characterized by measuring the output voltage pulses, whilst scanning load resistance from 1 MΩ to 1 GΩ.

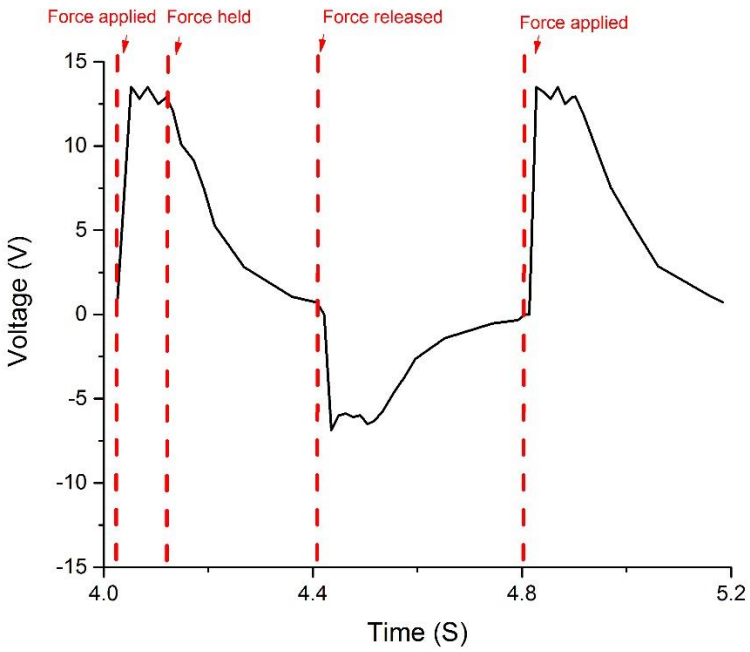

Figure 5-19: Output voltage of PDMS ferroelectret at the optimal resistance of 65 MΩ

Figure 5-20 shows the characteristic current-voltage (I-V) curves of a four-layer parallelogram PDMS ferroelectret under compressive forces that were applied in normal walking mode, as a function of load resistance. The voltage values used in Figure 5-20 are the average of measured voltages from three consecutive pulses. The peak current decreases with increasing load resistance in the range of 1 MΩ to 1 GΩ. The voltage increases with increasing load resistance. Consequently, the power output reaches the maximum value of 2.73 μW with a 65 MΩ loading resistance as shown in Figure 5-21. Due to impedance matching theory, to maximize the output power, the output impedance should be equal to the input impedance of ferroelectret. The input impedance of the ferroelectret can be simplified as an impedance of capacitor. The input impedance of the ferroelectret can be expressed as:

$$X_c = \frac{1}{2\pi f C_f} = R_L \tag{5-1}$$

Where X_c is the impedance of the ferroelectret, f is the frequency of the output current, C_f is the capacitance of the ferroelectret and the R_L is the output impedance.

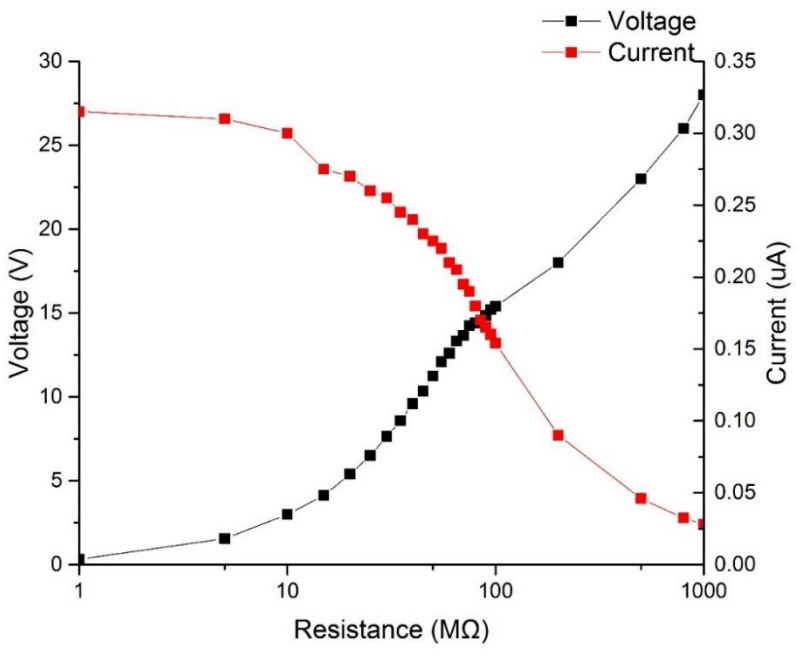

Figure 5-20: The characteristic *I-V* curves of a four layers PDMS ferroelectret

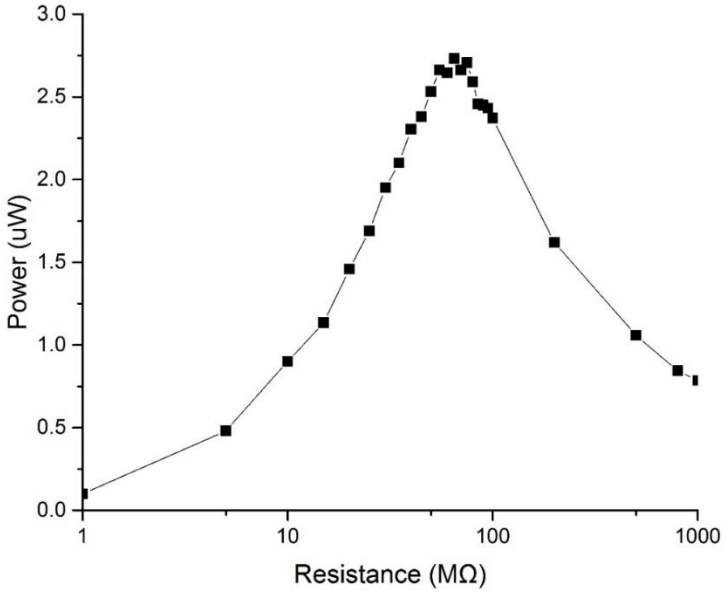

Figure 5-21: Instantaneous power output at different resistance loadings

In energy harvesting applications where the energy is extracted in pulses it may be preferable that the power management circuit is self-powered [131], i.e. the generated energy is used straightway and no energy storage is used. The advantage of powering from the input comparing to powering from the system energy storage is that the power management circuit is active only during the energy pulse, and thus the overall quiescent losses are minimized. However, the power losses of the power management circuit are strongly influenced by the supply voltage [132-133]. Therefore, the high voltage generated by the proposed ferroelectret may not be desirable for the electronic circuit. It may also be desirable to increase the pulse width at the expense of energy content in order to reduce the intermittency, which in itself causes system energy loss during start-up, as shown in [134]. In addition, as many integrated circuits only work safely under a voltage stress of 5.5 V, and a high external resistive load to the materials will make the matching from power converter being difficult in the CMOS process, it is ideal to have output voltage in the range of 1 V to 5.5 V. At 10 MΩ, the output peak voltage is 3 V and its instantaneous current is 0.3 μA, which, once rectified and smoothed, would be suitable to be used directly as the supply to electronic circuits. Thus 10 MΩ is used as the resistive load in the following measurements.

The maximum compressive force applied on the ferroelectret in this work is set to be 800 N, roughly resembling a walking person with weight of 80 kg in normal walking mode. The energy output is investigated in this work by varying the quantities of compressive forces. Figure 5-22 shows the change of peak output voltage at different applied force with load resistance of 10 MΩ. It is found that the output voltage increases linearly with increasing forces.

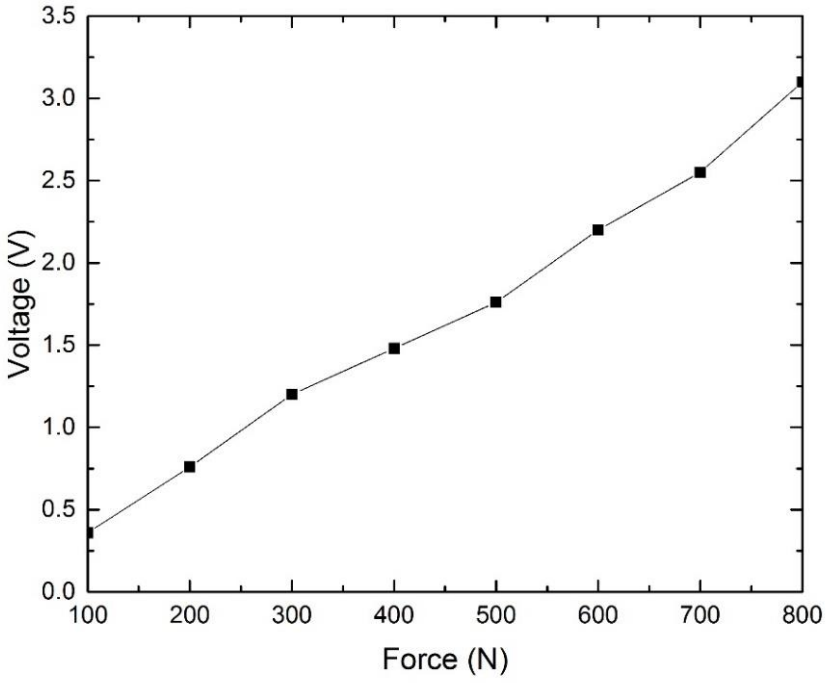

Figure 5-22: Peak output voltage at different applied compressive forces

The output voltage is also affected by walking mode. Figure 5-23 shows the single output pulses of PDMS ferroelectret under 800 N compressive force in different walking modes. From this Figure, the voltage peak increase with the increasing step frequency and the maximum voltage peak is achieved in the fast walking mode with the highest step frequency. However, the duration of voltage output pulses is decreased with the increasing step frequency. This can be explained by considering the change of force. In these walking modes with maximum force of 800 N, the applied compressive force can be considered as an object with a velocity. During the whole collision process, the deformation of sample is regarded

as an elasticity deformation. Due to Hooke's law, the applied force on the sample can be expressed as:

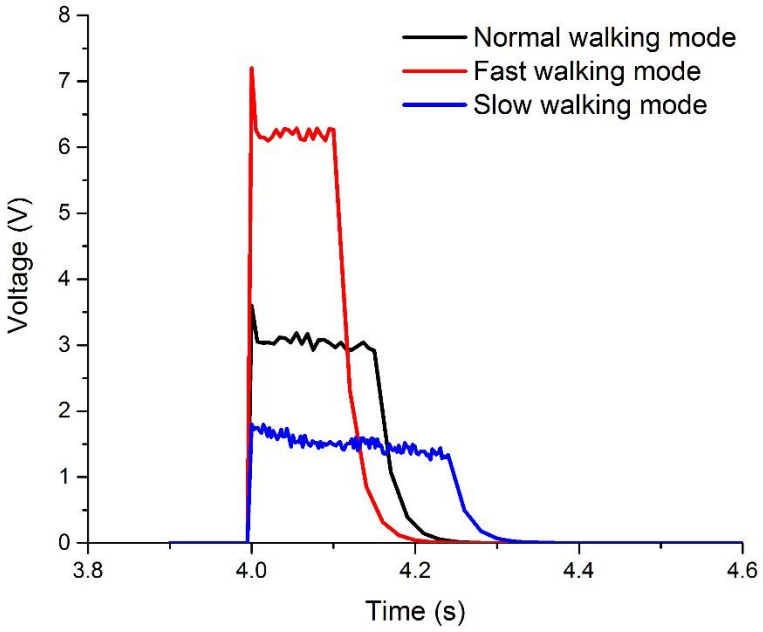

Figure 5-23: Output voltage pulse for three different walking mode under a constant force of 800 N

$$F = -kX \tag{5-1}$$

Where F is the applied force, k is a spring constant and X is the deformation of sample.

Thus the force F is directly proportional to X. With the step frequency increasing, the slope of applied force is increasing resulting in increasing deformation of the sample in unit time. As mentioned in previous chapter, the generated charge is directly proportional to the deformation of sample as:

$$V = \frac{\Delta Q}{t} R \tag{5-2}$$

Where V is the output voltage, ΔQ is the variation of charge, t is the time and R is the load resistance.

For these three walking modes, the applied force are the same resulting in the final deformation of sample should be the same. Thus the amount of variation of charge should be the same. Form Eq. (5-2), the peak voltage V of an output pulse is directly proportional to the duration of the applied force. It means that the peak voltage increase with the slope of applied force increasing. This explain the difference in voltage output in different walking modes. For the fast walking mode, it has the shortest transition time of the applied force from 0 to 800 N resulting in the maximum output peak voltage. Comparing with output pulses and the applied force wave function, the duration of output pulses is determined by transition time of the applied force. In addition, with the duration of force holding increasing, the duration of output pulses cannot be enhanced.

5.4 Conclusions

In this chapter, the piezoelectric characteristics, electric charging behaviour and energy harvesting capability of PDMS ferroelectret fabricated using silicon moulding were investigated.

The practical experiment revealed that the PDMS ferroelectret with lower effective area ratio sr_1 can generate higher piezoelectric coefficients d_{33} and the parallelogram void PDMS ferroelectret based on the same effective area ratio can achieve higher piezoelectric coefficients d_{33} than the rectangular void PDMS ferroelectret. The thickness ratio can also affect the piezoelectric coefficient d_{33}. For one void layer, two void layers and three void layers PDMS ferroelectret, the optimized thickness ratio are achieved around 0.8, 0.6 and 0.55, respectively. However, with the number of void increasing, the difference in piezoelectric coefficients d_{33} varying with the thickness ratio is becoming less distinct. For the long term piezoelectric coefficients measurement, the piezoelectric properties stability of PDMS ferroelectret is poor. The piezoelectric coefficient drops to about half of the initial value in 3 days.

For multilayer ferroelectret, the piezoelectric coefficients of four-layer PDMS ferroelectret is almost twice the piezoelectric coefficients of one void layer PDMS ferroelectret. The reason of this phenomenon is that, with the number of void increasing, the void can be

considered as distributing more and more away from the horizontal centerline of the ferroelectret. The piezoelectricity properties can be enhanced by the off horizontal centerline ratio. While the number of void layers in the range of 5 to 10, the piezoelectric coefficients d_{33} remain almost the same or even decline slightly. This is caused by the fact that the influence of void disturbed effect is decreased and the effective Young' modulus of the ferroelectret is increasing resulting in reduced piezoelectric properties.

To investigate the energy harvesting performance of fabricated PDMS ferroelectret, an electrodynamic instrument is used to quantify the applied compressive forces and their frequency, thus quantitatively correlates the output energy to the forces by resembling human walking. The parallelogram void PDMS ferroelectret with the maximum piezoelectric coefficients 520 pC/N and size of 2 cm×2 cm generates maximally 13 V, 2.73 μW with a 65 MΩ loading under a compressive force in normal walking model. From these results, it is found that the output voltage increases linearly with increasing forces. The maximum output voltage peak is affected by the step frequency. In other word, the peak voltage is directly proportional to the slope of applied force. In addition, the duration of output is determined by duration of applied force increasing and cannot enhanced by force holding duration increasing. It means that the static force cannot improve the energy output.

6 PDMS Ferroelectet with Enhanced Piezoelectricity

6.1 Introduction

In the previous chapter, the piezoelectric properties stability of PDMS ferroelectret is poor. The objective of this chapter is to present the use of ammonium dihydrogen phosphate (ADP) based polyvinyl alcohol (PVA) composite as electret material to enhance the charge density of the PDMS ferroelectret. ADP/PVA composite is selected as the electret material on account of their intrinsic properties such as: good flexibility, easy processing, cost effectiveness and non-toxic to human body [135]. Section 6.2 presents a theoretical model to study the piezoelectricity affected by introduced materials for PDMS ferroelectret. The fabrication process, the investigation of surface potential and the improved effects are presented in section 6.3, 6.4 and 6.5, respectively.

6.2 Principle

To analyse the piezoelectricity properties of ferroelectret, a simplified model for the piezoelectricity of a charge implanted PDMS-ADP/PVA composites ferroelectret structure with one void layer is illustrated in Figure 6-1.

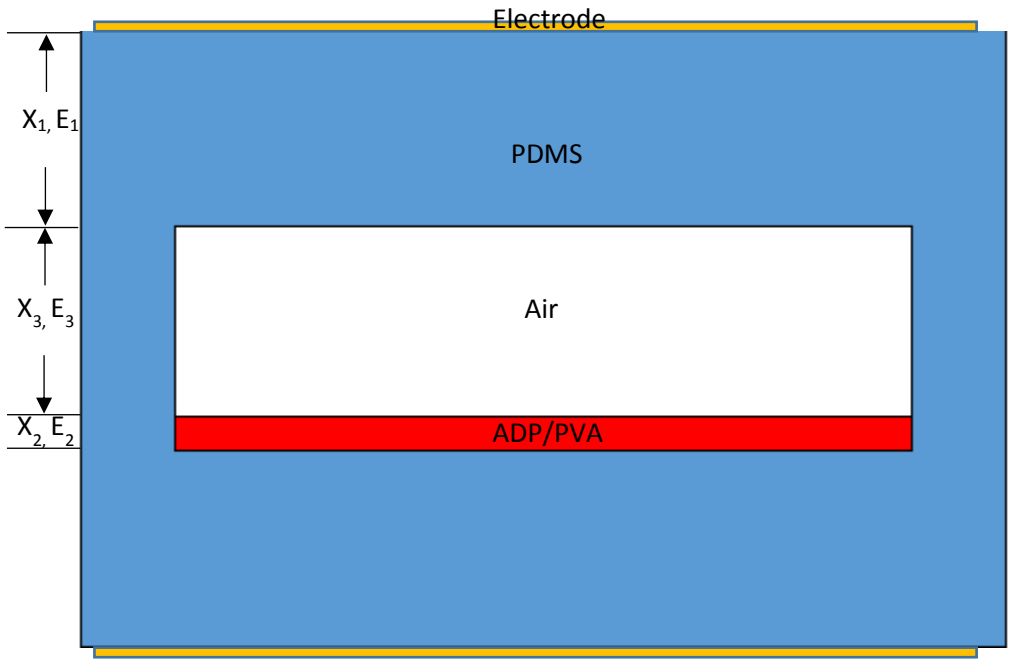

Figure 6-1: A simplified mode for charge implanted PDMS-ADP/PVA composites ferroelectret

For this ferroelectret structure, the electric field in the solid layer (E_1), the ADP/PVA layer (E_2) and void layer (E_3) can be obtained from Gauss' law for the interfaces:

$$E_1 = \frac{\sigma_m}{\varepsilon_1 \varepsilon_0}, E_2 = \frac{\sigma_m - \sigma}{\varepsilon_2 \varepsilon_0} and\ E_3 = \frac{\sigma_m - \sigma}{\varepsilon_0} \quad (6\text{-}1)$$

Where σ_m is the charge density on the electrodes, σ is the charge density on void surface, and ε_1 and ε_2 are the relative dielectric constant of PDMS and the relative dielectric constant of ADP/AVP composites, respectively. From Kirchhoff's second law under short circuit conditions

$$V = \int E\, dx = 2x_1E_1 + x_2E_2 + x_3E_3 = 0 \quad (6\text{-}2)$$

Where V is the electric potential applied on the PDMS-ADP/PVA ferroelectret, and x_1, x_2 and x_3 are the thickness of PDMS layer, ADP/PVA layer and void layer, respectively.

By substituting Eq. (6-1) into Eq. (6-2), it is found that

$$\sigma = \sigma_m * {(2\frac{x_1}{\varepsilon_1} + \frac{x_2}{\varepsilon_2} + x_3)}\Big/{(\frac{x_2}{\varepsilon_2} + x_3)} \quad (6\text{-}3)$$

Therefore, equation (6-3) can be simplified as

$$\sigma = \sigma_m * ({2\frac{x_1}{\varepsilon_1}}\Big/{\left(\frac{x_2}{\varepsilon_2} + x_3\right)} + 1) \quad (6\text{-}4)$$

If the ADP/PVA composites layer replaced by the air,

$$\varepsilon_2 = 1 \quad (6\text{-}5)$$

Then, Eq. (6-3) becomes:

$$\sigma' = \sigma_m * {(2\frac{x_1}{\varepsilon_1} + x_2 + x_3)}\Big/{(x_2 + x_3)} \quad (6\text{-}6)$$

Where σ' is the charge density on void surface for PDMS ferroelectret without ADP/PVA composites.

Therefore, Eq. (6-4) can be simplified as

$$\sigma' = \sigma_m * ({2\frac{x_1}{\varepsilon_1}}\Big/{(x_2 + x_3)} + 1) \quad (6\text{-}7)$$

The relative permittivity for ADP/PVA is around 300 which is higher than that of air. Therefore, we have

$$\left(\frac{x_2}{\varepsilon_2} + x_3\right) < (x_2 + x_3) \quad (6\text{-}8)$$

Hence,

$$\sigma = \sigma_m * ({2\frac{x_1}{\varepsilon_1}}\Big/{\left(\frac{x_2}{\varepsilon_2} + x_3\right)} + 1) > \sigma_m * ({2\frac{x_1}{\varepsilon_1}}\Big/{(x_2 + x_3)} + 1) = \sigma' \quad (6\text{-}9)$$

Based on the analysis above, casting a thin layer ADP/PVA composites on void surface can increase the void surface charge density.

The piezoelectric coefficient d_{33} is proportional to its void surface charge density

$$d_{33} \leq \frac{(1-sr_1)^2\sigma}{4sr_1c_{33}} (0 < sr_1 < 1) \qquad (6\text{-}10)$$

It can be found that the piezoelectric coefficient d_{33} is proportion to its void surface charge density. In other words, casting an electret material on void surface is a possible way to improve the piezoelectricity of ferroelectret.

The dielectric permittivity of ADP/PVA composites can be significantly improved with low concentration of ADP [135]. Figure 6-2 shows the relationship between the dependence of value fraction of the ADP and the effective permittivity of the ADP/PVA composites.

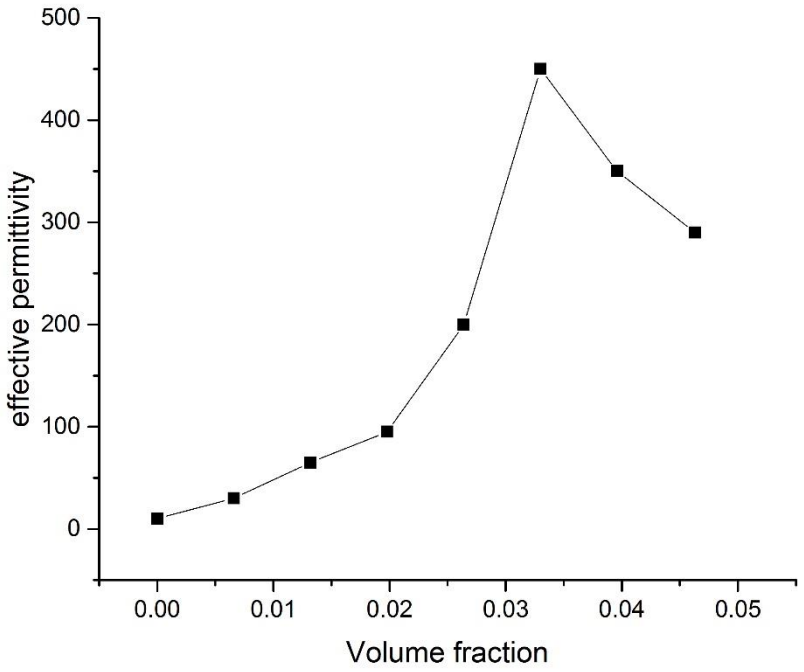

Figure 6-2: Dielectric permittivity of ADP/PVA composites as a function of volume fraction, measured at 1000 Hz and at room temperature [135]

6.3 Fabrication process

The proposed PDMS/PVA composite ferreoelectret with rectangular voids is fabricated using a 3D-printed moulding process as illustrated in Figure 6-3. The detail of the 3D-printed mould fabrication process has described in section 4.2.1.

Before fabricating the PDMS structure, liquid PDMS and curing agent (Sylgard 184 from Dow Corning, MI, USA) were mixed at a 10:1 weight ratio and the mixture was degassed in a vacuum desiccator. The degassed PDMS was poured into the glass-backed mould which were again degassed and then baked at 80 °C for 1 hour. When the degassed PDMS was poured into the mould, the fluid level in the mould was monitored to ensure the degassed PDMS would not overflow. This step is used to control the thickness of the material. Next, the PVA solution was prepared by dissolving 10g in 200 ml of distilled water in a glass beaker and stirred for 30 minutes while being heated at 40 °C due to the higher solubility PVA at this temperature. 2 g of ammonium salt was then dissolved in 100 ml of distilled water in another beaker and stirred for 30 minutes at room temperature. The PVA solution and ammonium salt solution were then mixed together by electromagnetic stirring for 10 minutes at 40 °C. The PVA composite solution is deposited using a doctor blade to the flat PDMS layer. The composite films was baked in an oven for 5 mins at 60 °C.

There are two possible methods to bond the two PDMS parts together: applying an adhesive or utilizing oxygen plasma machine. For the first method, degassed PDMS can be used as the adhesive. After detaching the polymerized PDMS from the moulds, the degassed liquid PDMS was painted on the part 1 with smooth surface and then the other PDMS layer was placed on to it, with its patterned surface in contact with the smooth surface (see figure 6-3). This bonding method was easy to implement but it was found to be difficult to control the amount of adhesive and overflow of the PDMS into the void would change the geometry of the whole cellular structure. In the second method, after detaching the polymerized PDMS from the moulds, an oxygen plasma treatment (Femto Asher, Diener, Germany, 30 S at 35-40W) was applied to both patterned surface of the PDMS part 2 and the smooth surface of PDMS part 1 which are then bonded together. In this experiment, plasma treatment was selected as the bonding method to avoid damage the structure ratio. The bonded PDMS-

ADP/PVA composite ferroelectret was baked in oven at 80 °C for 1 hour. A 10 N force was applied to the sample during the bake to improve the bond quality, and also to recover the original hydrophobic PDMS surface chemistry. The image of a fabricated PDMS-ADP/PVA composite ferreoelectret is shown in Figure 6-3.

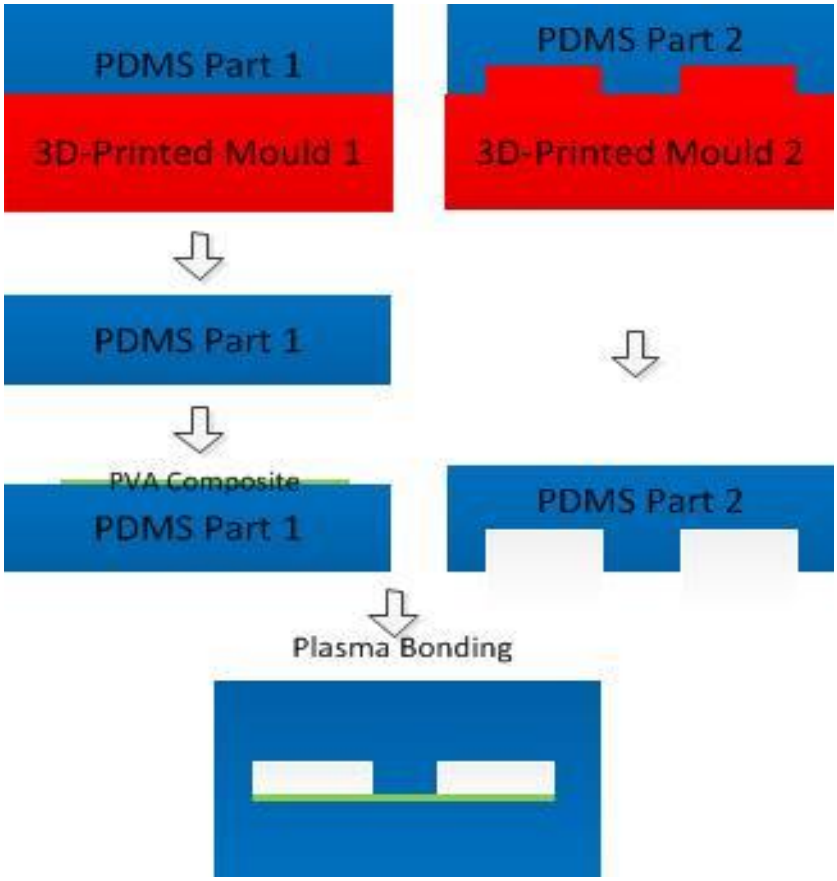

Figure 6-3: Schematic of PDMS-ADP/PVA composites ferroelectret fabrication processes

6.4 Investigation of surface potential

PDMS ferroelectret need to be electrically charged in order to present piezoelectric activities. The surface potential measurement for PDMS ferroelectret does not indicate the internal charges, because the measured surface potential is contributed to by both surface charges and compensating charges. To verify the casting electret material on void surface can improve its surface charge, in this experiment, a PDMS film with a thin layer of ADP/PVA

on surface is charged by corona charge. By contrast, a pure PDMS film is also charged by corona charging under the same condition.

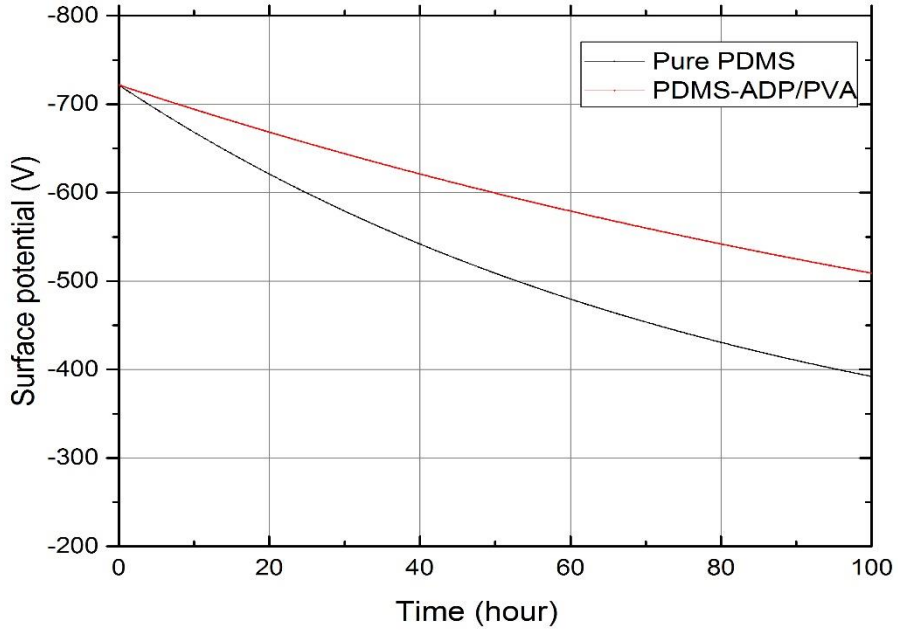

Figure 6-4: The surface potential as function of time for PDMS film with a thin layer of ADP/PVA composite and pure PDMS film at room temperature

Figure 6-4 show the decay of the surface potential as function of time for PDMS film with a thin layer of APD/PVA and pure PDMS film at room temperature. Both of the samples was corona charged with a corona-tip voltage of -25 kV for 2 minutes at room temperature. For the pure PDMS sample, the initial surface potential is -720 V, but it decreases significantly to a value of -390 V after 100 hours; the initial surface potential of the PDMS-ADP/PVA sample is -720 V and then it decay to -510 V after 100 hours. After corona charging, the initial surface potential of the PDMS film with a thin layer of ADP/PVA is equal to the initial surface potential of the pure PDMS film because the surface potential is formed by corona ions which were deposited on sample surface. The surface potential does not indicate the amount of the internal charges, because the measured surface potential is superposition of the induced charges and charges on sample surface. The surface charge is deposited by corona to establish internal electric field for breakdown and do not contribute

to the piezoelectricity. The decay rate end value of surface potential indicate the PDMS-ADP/PVA film can keep higher surface charge density than the pure PDMS film. Because the samples are exposed in atmosphere condition, the surface charges will be neutralized quickly. Hence, the majority of the surface potential is contributed to the induced charges. Moreover, the induced charge is formed by the internal charges. It means that the PDMS ferroelectret with a thin layer ADP/PVA composites should be achieved higher surface charge density on internal void surface than the pure PDMS ferroelectret.

6.5 Investigation of electromechanical properties

6.5.1 Piezoelectric coefficients measurement

To investigate the piezoelectric coefficients d_{33} affected by the ADP/PVA composites, the PDMS ferroelectret with a thin layer of ADP/PVA on the internal void surface is polarized by a corona charging. A corona-tip voltage of -25 kV and a charging time of 2 minutes are employed. Another pure PDMS ferroelectret is also polarized under the same condition as reference sample. Figure 6-5 shows a comparison of piezoelectric performance between PDMS ferroelectret and PDMS-ADP/PVA composite ferroelectret. The initial piezoelectricity of PDMS-ADP/PVA ferroelectret is 110 pC/N which is 1.5 times greater than that of the PDMS ferroelectret. The PDMS-ADP/PVA ferroelectret retain around 80 % of its initial piezoelectric coefficients d_{33} over 72 hours comparing with 40 % for the pure PDMS material over 72 hours.

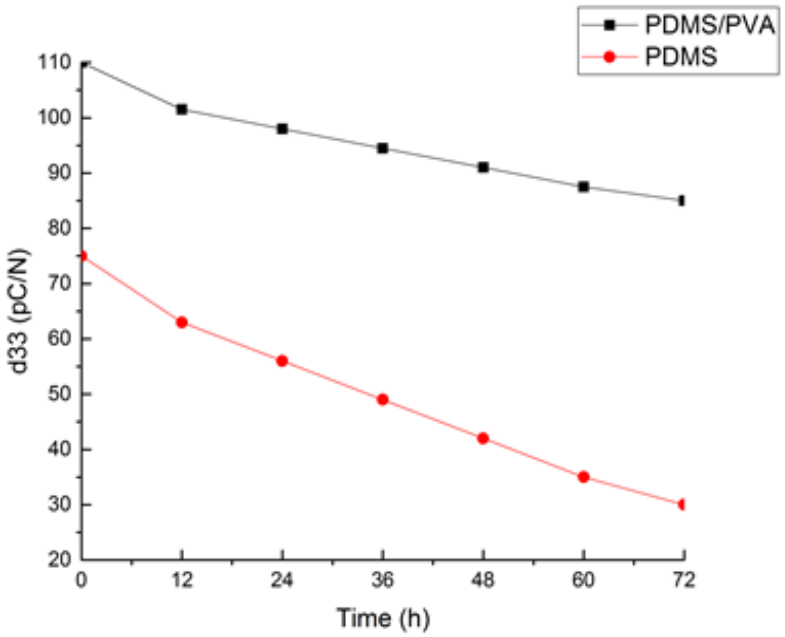

Figure 6-5: Piezoelectric coefficient d_{33} decay for 72 hours

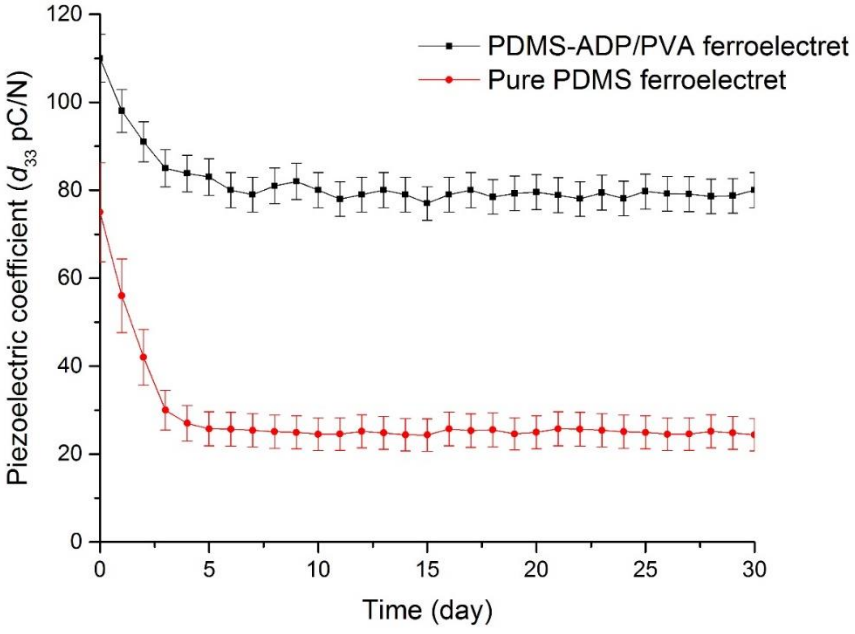

Figure 6-6: The long term measurement of piezoelectric coefficient at room temperature

Figure shows 6-6 the long term measurement of piezoelectric coefficients d_{33} at room temperature for both of the samples. The decay of d_{33} for PDMS-ADP/PVA ferroelectret becomes slow with time, and about 72 % of the initial value is remain after 30 days. For pure PDMS ferroelectret, the piezoelectric coefficients d_{33} decline to 32 % of the initial value after 30 days. The piezoelectric coefficient d_{33} used in Figure 6-6 are the average of measured piezoelectric coefficient from 5 times measurement. The error bar of measured piezoelectric coefficient d_{33} can be caused by the change of the measurement position on the sample. Once the sample was removed from the sample holder after measurement, it is difficult for take measurement at exactly the same position in the next time. In addition, as the experimental period was extentded to one month, the experiment conditions such as temperature and humidity, were not well controlled and were varying over time.

6.5.2 Energy harvesting performance

To investigate the energy harvesting performance affected by the ADP/PVA composites, the output voltage these sample are recorded using an oscilloscope. To quantify the applied force on the test sample, an Instron electrodynamic instrument (ElectroPuls E1000, Instron Ltd) is used. In this experiment, the dynamic force with square waveform applied on these sample is set as 800 N and the frequency of the dynamic force is set 1 Hz.

The output voltage of the PDMS ferroelectret and PDMS-APD/PVA ferroelectret under compressive forces is as shown in Figure 6-7 and Figure 6-8. From Figure 6-7, the maximal peak voltage measured 1 hour after corona charging for PDMS ferroelectret and PDMS-ADP/PVA ferroelectret are about 1 V and 1.5 V, respectively. In Figure 6-8, the maximum peak voltage at 72 hours after corona charging for PDMS ferroelectret and PDMS-APD/PVA ferroelectret are about 0.5 V and 1.1 V, respectively. Thus, the PDMS-APD/PVA retains about 73 % of its output voltage after 72 hours while output voltage of the PDMS ferroelectret dropped by a half.

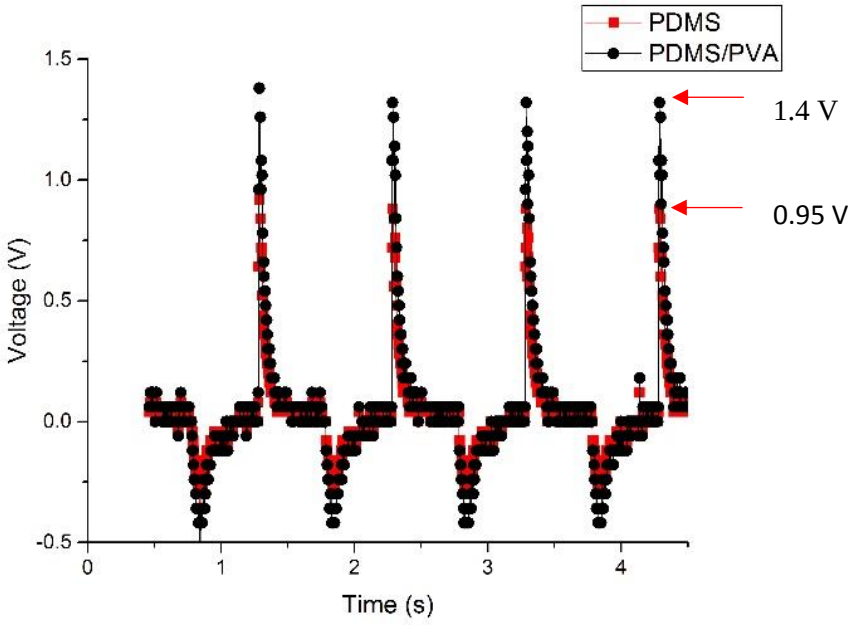

Figure 6-7: Measured voltage output pulse for PDMS and PDMS-AVP/PVA composite ferroelectret

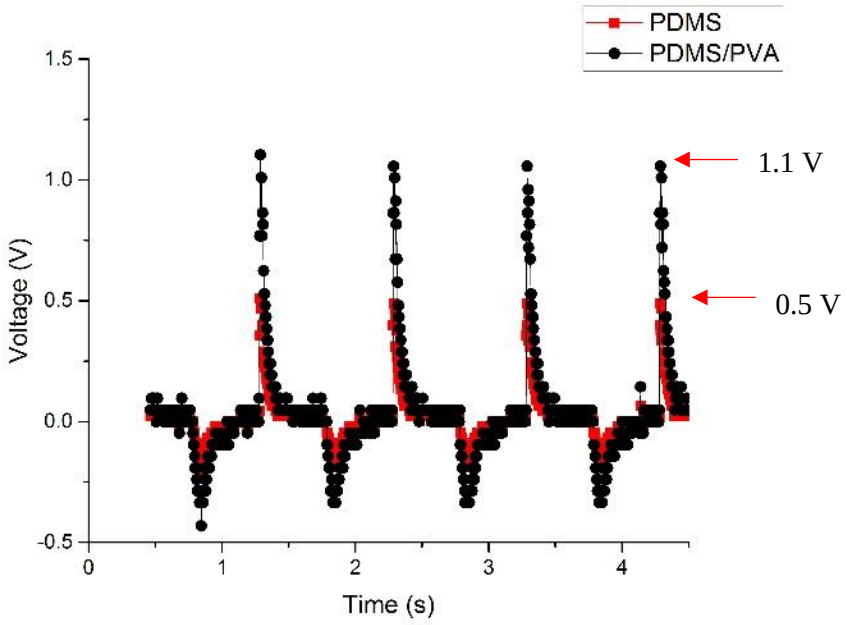

Figure 6-8: Measured voltage output for PDMS and PDMS-AVP/PVA composite ferroelectret at 72 hour after corona charging

In addition, after 1000 measurements, the thin layer of ADP/PVA composites on the internal void surface is broken by the repeated mechanical loading, but the PDMS structure remains intact. Figure 6-9 show the mechanical failure for PDMS-ADP/PVA ferroelectret. The piezoelectric coefficients of PDMS-ADP/PVA is decline to around 5 pC/N.

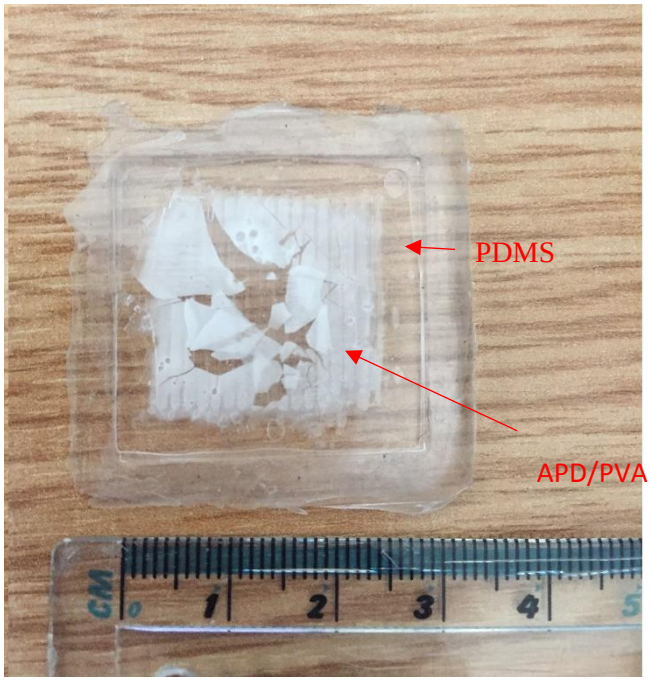

Figure 6-9: The image of mechanical failure for PDMS-ADP/PVA composites ferroelectret

6.6 Conclusion

In this chapter, a mathematical model is established to reveal the relationship between the piezoelectric coefficients d_{33} for PDMS ferroelectret and the dielectric constant of the introduced electret material. Then, the practical experiment verified that the high dielectric constant can achieve higher surface charge density on void surface and generate higher piezoelectric coefficient d_{33}. In the experiment, the piezoelectric coefficient of the PDMS-ADP/PVA ferroelectret was 80% of its initial value 72 hours after corona charging. In comparison, the piezoelectric coefficients of the PDMS structure without the ADP/PVA layer reduced to 40 % of its initial value over the same period of time. In the test under compressive forces, the output voltage of the PDMS-ADP/PVA ferroelectret was about 73 % of its initial value 72 hours after corona charging compared to 50 % for PDMS ferroelectret.

However, due to the poor mechanical characteristic of the thin layer of ADP/PVA, the thin layer of ADP/PVA composites was broken after 1000 times testing.

7 Conclusions and Future Work

7.1 Conclusion

Energy harvesting technology has emerged as an alternative power supply method for wearable electrical device due to the sustainability of energy supplying. In the literature, the most common energy source for wearable electronic systems is kinetic energy. To harvest kinetic energy, the popular approach is using piezoelectric material which convert kinetic energy into electric energy. Comparing with the common piezoelectric materials (PZT, PVDF), ferroelectret with high piezoelectric properties, light and soft has attracted more and more research. The piezoelectric properties of ferroelectrets are strongly determined by the geometry of the cellular structure. However, present foaming techniques are usually ill-controlled in both individual void geometry and cellular structure. This preparation defect usually impacts the resulting piezoelectric properties, limits the reproducibility in industry and also obstructs to further integrate with wearable electronic systems.

This research established a mathematical model and simulated in ANSYS to reveal the relationship between the geometry of ferroelectret cellular structure and its piezoelectric properties. It further presented the fabrication processes for the cellular structure and evaluate its piezoelectric properties and energy harvesting performance. In addition, introducing electret material to enhance the piezoelectric properties of ferroelectret has presented.

From the analytical model and ANSYS simulation, the piezoelectric coefficients d_{33} is determined by the effective area of the solid and void layers (sr_1) and the ratio of the void thickness to solid thickness (tr_1). The results for single void layer PDMS ferroelectret show that the optimized piezoelectric coefficients d_{33} is achieved at the thickness ratio tr_1=0.8 and a lowest possible sr_1. For multilayers PDMS ferroelectret, the optimized piezoelectric coefficient d_{33} is obtained at the tr_1=0.4 which is the ratio of the effective area of void layers to the effective area of solid layers. Moreover, the results for different void shapes show that the parallelogram void ferroelectret can achieve higher piezoelectric coefficients d_{33} compared to rectangular and sector voids.

In this work, the PDMS ferroelectrets were fabricated by 3D-printed moulding method and silicon moulding, respectively. The practical experiment revealed that the PDMS ferroelectret with lower effective area (sr_1) can generate higher piezoelectric coefficient d_{33} and the thinner PDMS ferroelectret based on the same structure can enhance the piezoelectric coefficient d_{33} to some extent. For 3D-printed moulding fabrication processes, the designed PDMS ferroelectret presented a maximum piezoelectric coefficient d_{33} of 71 pC/N. It can provide the maximum output voltage of 0.68 V and average output power of 0.46 μW when connected to a 1 MΩ resistive load under a square compressive force of 800 N and 14 Hz. This is corresponding to area unit power output of 0.318 nW/mm^2, and volume unit power output of 0.308 nW/mm^3. For silicon moulding fabrication processes, the designed PDMS ferroelectret presented a maximum piezoelectric coefficient d_{33} of 520 pC/N. It can provide the maximum output voltage of 13 V and average output of 2.73 μW when connected to a 65 MΩ resistive load under a compressive force of 800 N at normal walking model. This is corresponding to area unit power output of 3.03 nW/mm^2, and volume unit power output of 6.53 nW/mm^3. The parallelogram void ferroelectret present higher piezoelectric coefficient than the rectangular void ferroelectret. These experimental results reveal the relationship between the piezoelectric properties of ferroelectret and its cellular structure, which are in good agreement with simulations results. This analysis method may provide useful reference to design ferroelectrets.

Although experimental results of the fabricated PDMS ferroelectret are very promising, the piezoelectric coefficient d_{33} decline very quickly after corona charging, because the weak charge stability on PDMS surface. The capability of PDMS material also limit PDMS piezoelectric coefficient due to its small surface charge density. To solve this problem, a thin layer of ADP/PVA composites is deposited on ferroelectret internal void surface. The piezoelectric coefficient of the PDMS-ADP/PVA ferroelectret was 80% of its initial value 72 hours after corona charging. In comparison, the piezoelectric coefficients of the PDMS structure without the ADP/PVA layer reduced to 40 % of its initial value over the same period of time. In the test under compressive forces, the output voltage of the PDMS-ADP/PVA ferroelectret was about 73 % of its initial value 72 hours after corona charging compared to 50 % for PDMS ferroelectret. These results prove that PVA composite is

effective in extending the charge lifespan and enhancing the piezoelectric activity for PDMS ferroelectret. However, due to the poor mechanical characteristic of the thin layer of ADP/PVA, the thin layer of ADP/PVA composites was broken after 1000 times testing.

7.2 Outlook

Further research is needed in order to improve the sustainability of the introduced electret material. From present experimental results, the ADP/PVA composites can only survive less than 1000 times of compression. The reason for the mechanical fatigue for the ADP/PVA composites layer should be investigated. This mechanical fatigue could be caused by the relative displacement between the ADP/PVA composites layer and PDMS layer or the mechanical properties of ADP/PVA composites. A new electret material can be considered with strong adhesion to PDMS and better mechanical properties. With the silicon fabrication process, the compatibility of the new electret material should be considered to make it possible for industrial production on large scale. In addition, multilayer void ferroelectret can be suggested. Due to the reproducibility of the MEMS fabrication processes, PDMS ferroelectret with uniform properties can be produced.

Based on the proposed model, the piezoelectric properties under different conditions, such as in bending, in rub and contact with human skin, can also be investigated to find the optimized cellular structure for the most possible wearable applications. For human body energy harvesting application, the inherent frequency of cellular structure is main parameter should be considered, because the frequency of energy source from human body is below 5 Hz. The possible solutions are injecting dielectric oil into the voids of ferroelectret to reduce the frequency of the ferroelectret or attached other mechanical part to form a suitable harvester. In addition, the effect of layer alignment in the multilayer micro-machined ferroelectret should be considered.

Some proper treatments should be considered, including some preparation treatment and polarization method. Using inert gas, such as nitrogen, replacing the air inside the voids of ferroelectret, the charge storage ability for the ferroelectret are possible to be enhanced. Adjusting the charging temperature, the charging efficiency may be increased therefore

enhance the piezoelectric properties. Except for corona charging and contact charging, there are several other charging techniques, such as electron beam, which can be applied on the ferroelectret in order to achieve better polarization effect.

List of References

[1] Priya S, Inman DJ "Energy Harvesting Technologies", New York: Springer. 2009

[2] T. J. Kazmierski and S. Beeby. "Energy harvesting systems principles, modeling and applications", Springer Science, Berlin, Heidelberg. 2011

[3] H. Kawai, "Piezoelectricity of poly(vinylidene fluoride)", Japan J. Appl. Phys., vol. 8 (7), pp. 975-976, 1969.

[4] T. T. Wang, J. M. Herbert, and A. M. Glass, "The Applications of Ferroelectric Polymers," Chapman & Hall, New York, USA, 1998, ch. Introduction.

[5] N. Behrendt, G. Greiner, F. Fisher, T. Frese, V. Altstädt, H. -W. Schmidt, R. Giesa, J. Hillenbrand, and G. M. Sessler, "Morphology and electret behaviour of microcellular high glass temperature films", Appl. Phys. A: Mater. Sci. Process., vol. 85 (1), pp. 87-93, 2006.

[6] S. Bauer, R. Gerhard-Multhaupt, and G. M. Sessler, "Ferroelectrets: soft electroactive foams for transducers", Physics Today, vol. 57 (2), pp. 37-43, 2004.

[7] M. Wegener and S. Bauer, "Microstorms in cellular polymers: a route to soft piezoelectric transducer materials with engineered macroscopic dipoles", ChemPhysChem, vol. 6, pp. 1014-1025, 2005.

[8] S. Bauer, "Piezo-, pyro- and ferroelectrets: soft transducer materials for electromechanical energy conversion", IEEE Trans. Dielect. Electr. Insul., vol. 13 (5), pp. 953-962, 2006.

[9] M. Paajanen, "The cellular polypropylene electret material-Electromechanical properties", Dissertation, VTT Publications 436, Technical Research Center of Finland, Tampere University of Technology, 2001.

[10] S. Bauer, R. Gerhard-Multhaupt, and G. M. Sessler, "Ferroelectrets: soft electroactive foams for transducers", Physics Today, vol. 57 (2), pp. 37-43, 2004.

[11] M. Wegener and S. Bauer, "Microstorms in cellular polymers: a route to soft piezoelectric transducer materials with engineered macroscopic dipoles", ChemPhysChem, vol. 6, pp. 1014-1025, 2005.

[12] J. Lekkala, R. Poramo, K. Nyholm, and T. Kaikkonen, "EMF force sensor – a flexible electret film for physiological applications", Med. Biol. Eng. Comput., vol. 34, pp. 67-68, 1996.

[13] M. Paajanen, H. Välimäki, and J. Lekkala, “Modelling the electromechanical film (EMFi)”, J. Electrostat., vol. 48 (3-4), pp. 193-204, 2000.
[14] J. Backman. “Audio applications of electrothermomechanical film (ETMF)”, J. Aud. Eng. Soc., vol. 38 (5), pp. 364-371, 1990.
[15] R. Kressmann, “New piezoelectric polymer for air-borne and water-borne sound transducers”, J. Acoust. Soc. Am., vol. 109 (4), pp. 1412-1416, 2001.
[16] J. Hillenbrand and G. M. Sessler, “High-sensitivity piezoelectric microphones based on stacked cellular polymer films”, J. Acoust. Soc. Am., vol. 116 (6), pp. 3267-3270, 2004.
[17] M. Wegener, S. Bergweiler, W. Wirges, A. Pucher, and R. Gerhard-Multhaupt, “Voided space-charge electrets - piezoelectric transducer materials for electroacoustic applications”, J. Audio Engin. Soc., Convention Paper 6149 (Audio Engineering Society, New York, USA 2004), pp. 1-8.
[18] M. Wegener, S. Bergweiler, W. Wirges, A. Pucher, E. Tuncer, and R. Gerhard-Multhaupt, “Piezoelectric two-layer stacks of cellular polypropylene ferroelectrets: transducer response at audio and ultrasound frequencies”, IEEE Trans. Ultras. Ferroelectr. Freq. Contr., vol. 52, pp. 1601-1607, 2005.
[19] M. Paajanen, J. Lekkala, and K. Kirjavainen, “Electromechanical film (EMFi) - a new multipurpose electret material”, Sens. Actu. A: Phys., vol. 84 (1-2), pp. 95-102, 2000.
[20] I. Graz, M. Kaltenbrunner, C. Keplinger, R. Schwödiauer, S. Bauer, S. P. Lacour, and S. Wagner, “Flexible ferroelectret field-effect transistor for large-area sensor skins and microphones”, Appl. Phys. Lett., vol. 89 (7), no. 073501, 2006.
[21] L. Räisänen, K. Kirjavainen, K. Korhonen, and J. Sarlin, “Eletromechanical film - a new promising material”, High Technology Finland, pp. 164-165, 1995.
[22] G. M. Sessler and J. Hillenbrand, “Electromechanical response of cellular electret films”, Appl. Phys. Lett., vol. 75 (21), pp. 3405-3407, 1999.
[23] J. Hillenbrand and G. M. Sessler, “Piezoelectricity in cellular electret films”, IEEE Trans. Dielect. Electr. Insul., vol. 7 (4), pp. 537-542, 2000.
[24] M. Paajanen, J. Lekkala, and H. Välimäki, “Electromechanical modeling and properties of the electret film EMFi”, IEEE Trans. Dielect. Electr. Insul., vol. 8 (4), pp. 629-636, 2001.

[25] P. Bauer, M. Sichitiu, R. Istepanian, and K. Premaratne, “The mobile patient: Wireless distributed sensor networks for patient monitoring and care”, in Proc. Int. Conf. Inf. Technol. Applicat. Biomed. *(EMBS*), Arlington, VA, Nov. 2000, pp. 17–21.

[26] B. P. L. Lo and G. Z. Yang, “Key technical challenges and current implementation of body sensor networks,” in 2nd Int. Workshop Wearable Implantable Body Sensor Netw., Imperial College London, South Kensington, London, U.K., Apr. 2005, pp. 1–5.

[27] G. Go¨rge, M. Kirstein, and R. Erbel, “Microgenerators for energy autarkic pacemakers and defibrillators: Fact or fiction?”, Herz, vol. 26, no. 1, pp. 64–68, Feb. 2001.

[28] M. G. Allen, “Implantable micromachined wireless pressure sensors: Approach and clinical demonstration”, in Proc. 2nd Int. Workshop Wearable Implantable Body Sensor Netw., Imperial College London, South Kensington, U.K., Apr. 2005, pp. 40–43.

[29] B. B. Owens, “Batteries for Implantable Biomedical Devices”, New York: Plenum, 1986.

[30] D. Wanless, “Securing our future health: Taking a long term view,” HM Treasury, U.K., Apr. 2002, Tech. Rep.

[31] A. Flowerday and R. Smith, “Lessons learnt from long-term chronic condition monitoring”, in Proc. 1st Int. Workshop Wearable Implantable Body Sensor Netw., Imperial College London, U.K., Apr. 2004, p. 48.

[32] P. Needham and L. Gamlyn, “Arrhythmia analysis in the community,” in Proc. 1st Int. Workshop Wearable Implantable Body Sensor Netw., Imperial College London, U.K., Apr. 2004, pp. 49–50.

[33] A. Heller, “Drug delivering integrated therapeutic systems”, in Proc. 2nd Int. Workshop Wearable Implantable Body Sensor Netw., Imperial College London, South Kensington, London, U.K., Apr. 2005, pp. 6–11.

[34] T. Starner. “Human-powered wearable computing”, IBM SYSTEM JOURNAL, Vol 35, NOS 3&4, 1996.

[35] Goto H, Sugiura T and Kazui T “Feasibility of the automatic generating system (AGS) for quartz watches as a leadless pacemaker power source: a preliminary report”, Eng.Med. Biol. Soc. **1** 417–9 1998

[36] Morais R, Silva N M, Santos P M, Frias C M, Ferreira J A F, Ramos A M, Sim˜oes J A O, Baptista J M R and Reis M C 2011 “Double permanent magnet vibration power generator for smart hip prosthesis”, Sensors Actuators A **172** 259–68

[37] Luciano V, Sardini E, Serpelloni M and Baronio G “Analysis of an electromechanical generator implanted in a human total knee prosthesis”, IEEE Sensors Applications Symp. *(SAS)* pp 1–5 2012

[38] R. Tashiro, N. Kabei, K. Katayama, Y. Ishizuka, F. Tsuboi, and K. Tsuchiya, “Development of an electrostatic generator that harnesses the motion of a living body”, JSME Int. J., ser. C, vol. 43, no. 4, pp. 916–922, 2000.

[39] Naruse Y, Matsubara N, Mabuchi K, Izumi M and Honma K 2008 “Electrostatic micro power generator from low frequency vibration such as human motion” Proc. Power MEMS 2008 pp 19–22

[40] Umeda M, Nakamura K and Ueha S “Analysis of the transformation of mechanical impact energy to electric energy using piezoelectric vibrator”, Japan. J. Appl. Phys.35 3267-73 1996

[41] N. A. Shenck and J. A. Paradiso, “Energy scavenging with shoe mounted piezoelectrics,” *IEEE Micro,* vol. 21, pp. 30–42, May–Jun. 2001.

[42] Renaud M, Sterken T, Fiorini P, Puers R, Baert K and van Hoof C “Scavenging energy from human body: design of a piezoelectric transducer”, Tech. Digest 13th Int. Conf. on Solid-State Sensors and Actuators Transducers ’05 (Seoul, Korea) vol 1, pp 784–7 2005

[43] N. G. Elvin, A. A. Elvin, and M. Spector, “A self-powered mechanical strain energy sensor,” Smart Mater. Struct., vol. 10, pp. 293–299, 2001.

[44] Shukla, R. and A. J. Bell. "PENDEXE: A novel energy harvesting concept for low frequency human waistline", Sensors and Actuators A: Physical 222(0): 39-47. 2015

[45] J.-H. Yang , H.-S. Cho , S.-H. Park , S.-H. Song , K.-S. Yun , and J. H. Lee, ”effect of garment design on piezoelectricity harvesting from joint movement”, Smart Mater. Struct. 25, 035012 (2016). https://doi.org/10.1088/0964-1726/25/3/035012,

[46] S. C. Jacobsen, D. L. Wells, C. C. Davis, and J. E. wood, “Fabrication of microstructures using non-planar lithography(NPL)”, in Tech, Dig., IEEE Micro Electro Mechanical Systems Workshop, Nara, Japan, Jan. 30-Feb. 2, 1991, pp. 45-50

[47] Lin, C.-J.; Lin, P.-T. “Tracking control of a biaxial piezo-actuated positioning stage using generalized Duhem model”, Comput Math Appl 2012, 64, 766-787

[48] Qaiss, A.; Saidi, H.; Fassi-Fehri, O.; Bousmina, M. “Cellular polypropylene-based piezoelectric films”, Polym Eng Sci 2012, 52, 2637.

[49] Kawai, H. “The piezoelectricity of poly(vinylidene fluoride)”, Jpn J Appl Phys 1969, 8, 975.

[50] Kirjavainen, K. “Electromechanical film and procedure for manufacturing same”, US Patents 4,654,546, 1987.

[51] Savolainen, A.; Kirjavainen, K. J Macromol Sci, Chem “Electrothermomechanical film: part 1. Design and characteristics”,1989, 26, 583.

[52] Gilbert-Tremblay, H.; Mighri, F.; Rodrigue, D. J Cell “Morphology development of polypropylene cellular films fro piezoelectric applications”, Plast 2012, 48, 341.

[53] Wegener, M. “Piezoelectric polymer foams: transducer mechanism and preparation as well as touch-sensor and ultrasonic-transducer properties”, In Proceedings of SPIE, 7644, 76441A, 2010, pp. 1–9.

[54] Fang, P.; Wirges, W.; Wegener, M.; Zirkel, L.; Gerhard, R. “Cellular polyethylene-naphthalate films for ferroelectret applications: foaming, inflation and stretching, assessment of electromechanically relevant structural features”, e-Polymers 2008, 8, 487.

[55] Lindner, M.; Hoislbauer, H.; Schwodiauer, R.; Bauer-Gogonea, S.; Bauer, S. “Charged cellular polymers with “ferroelectretic” bhavior”, IEEE Trans Dielectr Electr Insul 2004, 11, 255.

[56] L. J. Gibson, M. F. Ashby, “Cellular Solids: Structure and Properties”, Cambridge U. Press, New York (1999).

[57] S. Bauer, R. Gerhard-Multhaupt, and G. M. Sessler, “Ferroelectrets: soft electroactive foams for transducers”, Physics Today, vol. 57 (2), pp. 37-43, 2004.

[58] M. Wegener, W. Wirges, J. Fohlmeister, B. Tiersch, and R. Gerhard-Multhaupt, “Two-step inflation of cellular polypropylene films: void-thickness increase and enhanced electromechanical properties”, J. Phys. D: Appl. Phys., vol. 37 (4), pp. 623-627, 2004

[59] M. Wegener, W. Wirges, and R. Gerhard-Multhaupt, “Piezoelectric polyethylene terephthalate (PETP) foams - Specifically designed and prepared ferroelectret films ”, Adv. Engi. Mat., vol. 7 (12), pp. 1128-1131, 2005.

[60] G. M. Sessler (Ed.), “Electrets”, 3rd Edition, vol. 1, Laplacian Press, Morgan Hill, California, 1998, ch. 2, pp. 54-57, 60-66.
[61] R. Gerhard-Multhaupt (Ed.), “Electrets”, 3rd Edition, vol. 2, Laplacian Press, Morgan Hill, California, USA, 1999, ch. 9-10.
[62] M. M. Perlman and S. Unger, “Electron-bombardment of electret foils”, Appl. Phys. Lett., vol. 24 (12), pp. 579-580, 1974.
[63] J. van Turnhout, “Thermally Stimulated Discharge of Polymer Electrets”, Elsevier, Amsterdam, 1975.
[64] H. von Seggern and J. E. West, “Stabilization of positive charge in fluorinated ethylene propylene copolymer”, J. Appl. Phys., vol. 55 (7), pp. 2754-2757, 1984.
[65] Z. Xia, H. Ding, G. Yang, T. Lu, and X. Sun, “Constant-current corona charging of Teflon PFA”, IEEE Trans. Electr. Insul., vol. 26 (1), pp. 35-41, 1991.
[66] An, Z.; Zhao, M.; Yao, J.; Zhang, Y.; Xia, Z. “Improved piezoelectric properties of cellular polypropylene ferroelectrets by chemical modification”, Appl Phys A 2009, 95, 801.
[67] M. Paajanen, J. Lekkala, and K. Kirjavainen, “Electromechanical film (EMFi) - a new multipurpose electret material”, Sens. Actu. A: Phys., vol. 84 (1-2), pp. 95-102, 2000.
[68] I. Graz, M. Kaltenbrunner, C. Keplinger, R. Schwödiauer, S. Bauer, S. P. Lacour, and S. Wagner, “Flexible ferroelectret field-effect transistor for large-area sensor skins and microphones”, Appl. Phys. Lett., vol. 89 (7), no. 073501, 2006.
[69] M. Paajanen, H. Välimäki, and J. Lekkala, “Modelling the sensor and actuator operations of the ElectroMechanical Film EMFi”, Proceedings, 10th International Symposium on Electrets, 22-24 September 1999, Delphi, Greece (IEEE Service Center, Piscataway, NJ, USA 1999), pp. 735-738.
[70] G. M. Sessler and J. Hillenbrand, “Electromechanical response equations of cellular electret films”, Proceedings, 10th International Symposium on Electrets, 22-24 September 1999, Delphi, Greece (IEEE Service Center, Piscataway, NJ, USA 1999), pp. 261-264.
[71] X. Zhang, J. Hillenbrand, and G. M. Sessler, “Improvement of piezoelectric activity of cellular polymers using a double-expansion process”, J. Phys. D: Appl. Phys., vol. 37, pp. 2146-2150, 2004.

[72] J. Hillenbrand, G. M. Sessler, and X. Zhang, "Verification of a model for the piezoelectric d33 coefficient of cellular electret films", J. Appl. Phys., vol. 98 (6), no. 064105, 2005.

[73] P. Zhang, Z. Xia, X. Qiu, F. Wang, and X. Wu, "Influence of charging parameters on piezoelectricity for cellular PP film electrets", Chin. Phys. Soc., vol. 55 (2), pp. 904-909, 2006.

[74] S. Qu, Y.Yu, "Electromechanical coupling properties and stability of ferroelectrets" J. Appl. Phys., 110 (2011), p. 043225

[75] Bauer, S.; Gerhard-Multhaupt, R.; Sessler, G. M. "Ferroelectrets: soft electroactive foams for transducers", Phys Today 2004, 57, 37.

[76] Zhang, X.; Hillenbrand, J.; Sessler, G. "Piezoelectric d_{33} coefficient of cellular polypropylene subjected to expansion by pressure treatment", Appl Phys Lett 2004, 85, 1226.

[77] Qiu, X.; Xia, Z.;Wang, F. "Piezoelectricity of single-and multi-layer cellular polypropylene film electrets", Front Mater Sci China 2007, 1, 72.

[78] Brana, G. O.; Segovia, P. L.; Magraner, F.; Quijano, A. "Influence of corona charging in cellular polyethylene film", J Phys: Conf Ser 2011, 301, 012054.

[79] Wirges,W.;Wegener, M.; Voronina, O.; Zirkel, L.; Gerhard-Multhaupt, R.Adv "Optimized preparation of elastically soft, highly piezoelectric, cellular ferroelectrets from nonvoided poly(ethylene terephthalate) films", Funct Mater 2007, 17, 324.

[80] Fang, P.;Wegener, M.;Wirges,W.; Gerhard, R.; Zirkel, L. " Cellular polyethylene-naphthalate ferroelectrets: Foaming in supercritical carbon dioxide, structural and electrical preparation, and resulting piezoelectricity", Appl Phys Lett 2007, 90, 192908.

[81] Xia, Z.; Gerhard-Multhaupt, R.; K¨ unstler, W.; Wedel, A.; Danz, R. J "High surface-charge stability of porous polytetrafluoroethylene electret films at room and elevated temperatures", Phys D: Appl Phys 1999, 32, L83.

[82] Gerhard-Multhaupt, R.; Kunstler, W.;Gome, T.; Pucher, A.;Weinhold, T.; Seiß, M.; Xia, Z.;Wedel, A.; Danz, R. "Porous PTFE space-charge electrets for piezoelectric applications", IEEE Trans Dielectr Electr Insul 2000, 7, 480.

[83] Saarimaki, E.; Paajanen, M.; Savijarvi, A.-M.; Minkkinen, H.; Wegener, M.; Voronina, O.; Schulze, R.; Wirges, W.; Gerhard-Multhaupt, R. "Novel heat durable electromechanical

film: processing for electromechanical and electret applications", IEEE Trans Dielectr Electr Insul 2006, 13, 963.

[84] Montanari, G.; Fabiani, D.; Ciani, F.; Motori, A.; Paajanen, M.; Gerhard- Multhaupt, R.; Wegener, M. "Charging properties and time-temperature stability of innovative polymeric cellular ferroelectrets", IEEE Trans Dielectr Electr Insul 2007, 14, 238.

[85] Saarimaki, E.; Paajanen,M.; Savijarvi, A.-M.; Minkkinen, H. "Novel heat durable electromechanical film processing: preparations for electromechanical and electret applications", In IEEE 2005 12th International Symposium on Electrets, 2005, pp. 220–223.

[86] Wegener, M.; Wirges, W.; Gerhard-Multhaupt, R. Adv Eng Mater 2005, 7, 1128.

[87] Wirges, W.; Wegener, M.; Voronina, O.; Zirkel, L.; Gerhard-Multhaupt, R. Adv "Optimized Preparation of Elastically Soft, Highly Piezoelectric, Cellular Ferroelectrets from Nonvoided Poly(ethylene Terephthalate) Films", Funct Mater 2007, 17, 324.

[88] Li, Y. and Zeng, C. (2013), "Low-Temperature CO2-Assisted Assembly of Cyclic Olefin Copolymer Ferroelectrets of High Piezoelectricity and Thermal Stability." Macromol. Chem. Phys., 214: 2733–2738. doi: 10.1002/macp.201300440

[89] R. Gerhard-Multhaupt (Ed.), Electrets, 3rd edn. Vol. 2, Laplacian Press, Morgan Hill, CA, USA 1999.

[90] L.M. Heikkinen, H.E.Panula, T. Lyyra, H. Olkkonen, I. Kiviranta, T. Nevalainen, and H.j. Helminen, *Scand. J. Lab. Animal Sci*. 1997,24, 85-92

[91] J. Lekkala, R. Poramo, K. Nyholm, T. Kaikkonen, "EMF-force sensor - a flexible and sensitive electret film for physiological applications", Medical & Biological Engineering & Computing, vol. 34, no. Supplement 1, 1996.

[92] A. Savolainen and K. Kirjavainen, "Electromechanical film. Part I. Design and characteristics", J. Macromol. Sci., Part A: Pure Appl. Chem., vol. A26, pp. 583-591, 1989.

[93] M. K. Hämäläinen, J. K. Parvianen, and T. Jaaskelainen, "A novel micromovement actuator manufactured using plastic electromechanical film", Rev. Sci. Instrum., vol. 67 (4), pp. 1598-1601, 1996.

[94] M. Paajanen, M. Wegener, and R. Gerhard-Multhaupt, "Understanding the role of the gas in the voids during corona charging of cellular electret films a way to enhance their piezoelectricity", J. Phys. D: Appl. Phys., vol. 34 (16), pp. 2482-2488, 2001.

[95] M. Paajanen, H. Minkkinen, and J. Raukola, “Gas diffusion expansion increased thickness and enhanced electromechanical response of cellular polymer electret films”, Proceedings, 11th International Symposium on Electrets, 1-3 October 2002, Melbourne, Australia (IEEE Service Center, Piscataway, NJ, USA 2002), pp. 191-194.

[96] M. Wegener, W. Wirges, J. Fohlmeister, B. Tiersch, and R. Gerhard-Multhaupt, “Two-step inflation of cellular polypropylene films: void-thickness increase and enhanced electromechanical properties”, J. Phys. D: Appl. Phys., vol. 37 (4), pp. 623-627, 2004.

[97] M. Wegener, W. Wirges, R. Gerhard-Multhaupt, M. Dansachmüller, R. Schwödiauer, S. Bauer-Gogonea, S. Bauer, M. Paajanen, H. Minkkinen, and J. Raukola, “Controlled inflation of voids in cellular polymer ferroelectrets: optimizing electromechanical transducer properties”, Appl. Phys. Lett., vol. 84 (3), pp. 392-394, 2004.

[98] W. Wirges, M. Wegener, O. Voronina, L. Zirkel, and R. Gerhard-Multhaupt, “Optimized preparation of elastically soft, highly piezoelectric, cellular ferroelectrets from nonvoided Poly(ethyleneterephthalate) films”, Adv. Funct. Mater., vol. 17 (2), pp. 324-329, 2007.

[99] O. Voronina, “Structure-property relations in polymer ferroelectrets”, Dissertation, University of Potsdam, 2008.

[100] M. A. Jacobs, “Measurement and modeling of thermodynamic properties for the processing of polymers in supercritical fluids”, Dissertation, Technische Universität Eindhoven, 2004.

[101] L. Zirkel, M. Jakob, and H. Münstedt, “Foaming of thin films of a fluorinated ethylene propylene copolymer using supercritical carbon dioxide”, J. Supercrit. Fluid., vol. 49 (1), pp. 103-110, 2009.

[102] Voronina, O., Wegener, M., Wirges, W. et al. “Physical foaming of fluorinated ethylene-propylene (FEP) copolymers in supercritical carbon dioxide: single-film fluoropolymer piezoelectrets”, Appl. Phys. A (2008) 90: 615. doi:10.1007/s00339-007-4371-4

[103] R. A. C. Altafim, C. Dias, L. G. Neto, H. C. Basso, C. Murakami, P. R. Veronese, and E. F. Rodrigues, “Piezoelectricity of multi-layers space-charge electrets from Teflon FEP film with homogeneous voids distributed on its surface”, Annual Report, Conference on

Electrical Insulation and Dielectric Phenomena, 19-22 October 2003, Albuquerque, NM, USA (IEEE Service Center, Piscataway, NJ, USA 2003), pp. 225-228.

[104] R. A. C. Altafim, H. C. Basso, R. A. P. Altafim, L. Lima, C. V. de Aquino, L. G. Neto, and R. Gerhard-Multhaupt, "Piezoelectrets from thermo-formed bubble structures of fluoropolymer-electret films", IEEE Trans. Dielect. Electr. Insul., vol. 13 (5), pp. 979-985, 2006.

[105] R. A. P. Altafim, X. Qiu, W. Wirges, R. Gerhard, R. A. C. Altafim, H. C. Basso, W. Jenninger, and J. Wagner, "Template-based fluoroethylenepropylene piezoelectrets with tubular channels for transducer applications", J. Appl. Phys., vol. 106 (1), no. 014106, 2009.

[106] R. A. P. Altafim, X. Qiu, W. Wirges, R. Gerhard, R. A. C. Altafim, H. C. Basso, W. Jenninger, and J. Wagner, "Template-based fluoroethylenepropylene piezoelectrets with tubular channels for transducer applications", J. Appl. Phys., vol. 106 (1), no. 014106, 2009.

[107] X. Zhang, J. Hillenbrand, G.M. Sessler, S. Haberzettl, K. Lou "Fluoroethylenepropylene Ferroelectrets with Patterned K. Fluoroethylenepropylene Ferroelectrets with Patterned" city. Appl. Phys. A: Mater. Sci. Process. 2012, 107, 621–629.

[108] Tsai, J.; Wang, J.; Su, Y., "Piezoelectric rubber films for human physiological monitoring and energy harvesting," Micro Electro Mechanical Systems (MEMS), 2013 IEEE 26th International Conference on , vol., no., pp.841,844, 20-24 Jan. 2013

[109] Yue Feng; Suzuki, Y., "All-polymer soft-X-ray-charged piezoelectret with embedded PEDOT electrode," Micro Electro Mechanical Systems (MEMS), 2013 IEEE 26th International Conference on , vol., no., pp.865,868, 20-24 Jan. 2013

[110] M. Sborikas, X. Qiu, W. Wirges, R. Gerhard, W. Jenninger, and D. Lovera, Screen printing for producing ferroelectret systems with polymer-electret films and well-defined cavities. Appl Phys A. 114, 515–520 (2014).

[111] Sessler, G.; Hillenbrand, J. Appl Phys Lett 1999, 75, 3405.

[112] Qiu, X.; Mellinger, A.; Gerhard, R. Appl Phys Lett 2008, 92, 052901.

[113] Zhang, P.; Xia, Z.; Qiu, X.; Wang, F.; Wu, X. In IEEE 12th International Symposium on Electrets 2005, 2005, pp. 39–42.

[114] U. Kogelschatz and J. Salge, "Fundamental aspects and applications", Low Temperature Plasma Physics, edited by R. Hippler, S. Pfau, M. Schmidt, and K. H. Schoenback, Wiley VCH, New York, USA, 2001, ch. 13, pp. 331-357.

[115] X. Qiu, A. Mellinger, M. Wegener, W. Wirges, and R. Gerhard, “Barrier discharges in cellular polypropylene ferroelectrets: How do they influence the electromechanical properties”, J. Appl. Phys., vol. 101 (10), no. 104112, 2007.

[116] X. Qiu, A. Mellinger, W. Wirges, and R. Gerhard, “Spectroscopic study of dielectric barrier discharges in cellular polypropylene ferroelectrets”, Appl. Phys. Lett., vol. 91, no. 132905, 2007.

[117] X. Qiu, R. Gerhard, A. Mellinger, "Turning Polymer Foams or Polymer-Film Systems into Ferroelectrets: Dielectric Barrier Discharges in the Voids", *IEEE Trans. Dielectr. Electr. Insul.*, vol. 18, pp. 34-42, 2011.

[118] B. Hilczer and J. Malecki. “Electrets,” Elsevier, 1986.

[119] J. A. Giacometti, S. Fedosov, and M. M. Costa, “Corona charging of polymers: Recent advances on constant current charging”, Braz. J. Phys., vol. 29, no. 2, pp. 269-279, 1999.

[120] G. M. Sessler (Ed.), Electrets, 3rd Edition, vol. 1, Laplacian Press, Morgan Hill, California, 1998, ch. 2, pp. 30-32.

[121] M.Wegener, M. Paajanen, W. Wirges, and R. Gerhard-multhaupt, proc. 11th int. Symp. Electrets, Melbourne, Australia 2002, 54-57.

[122] R. Gerhard-Multhaupt, M. Wegener, W. Wirges, J.A. Giacometti, R.A.C. Altafim, L.F. Santos, R.M. Faria, and M. Paajanen, Conf. Electrical Insulation and Dielectric Phenomena CEIDP, Annual report 200, 299-302

[123] Qiu, X.;Wegener, M.;Wirges,W.; Zhang, X.; Hillenbrand, J.; Xia, Z.; Gerhard-Multhaupt, R.; Sessler, G. M. J Phys D: Appl Phys 2005, 38, 649.

[124] Paajanen, M.; Wegener, M.; Gerhard-Multhaupt, R. In IEEE Conference on Annual Report Electrical Insulation and Dielectric Phenomena, 2001, pp. 24–27.

[125] SYLGARD® 184 SILICONE ELASTOMER KIT, Dow Corning Corporation, http://www.dowcorning.com/applications/search/products/details.aspx?prod=01064291&type=PROD (2000-2017)

[126] J.-J. Wang, T.-H. Hsu, C.-N. Yeh, J.-W. Tsai, and Y.-C. Su, "Piezoelectric PDM S Films for MEMS Transducers", *J MICROMECH MICROENG* 22 #015013, 2012

[127] Pawley JB (editor). Handbook of Biological Confocal Microscopy (3rd ed.). Berlin: Springer. 2006

[128] J. E. A. Bertram, "Constrained optimization in human walking: cost minimization and gait plasticity", Journal of experimental biology, Vol. 208, No. 6, pp. 979-991, 2005.

[129] J. E. A. Bertram and A. Ruina, "Multiple walking speed–frequency relations are predicted by constrained optimization", Journal of theoretical Biology, Vol. 209, No. 4 pp. 445-453, 2001.

[130] G. A. Cavagna and P. Franzetti, "The determinants of the step frequency in walking in humans", The Journal of Physiology, Vol. 373, No. 1, pp. 235-242, 1986

[131] Y. Rao, K. M. McEachern and D. P. Arnold, "A compact human-powered energy harvesting system", In Journal of Physics: Conference Series, Vol. 476, No. 1, pp. 012011, IOP Publishing, 2013.

[132] A. P. Chandrakasan, S. Sheng and R. W. Brodersen, "Low-power CMOS digital design", IEICE Transactions on Electronics, Vol. 75, No. 4, pp. 371-382, 1992

[133] V. Kursun, S. G. Narendra, V. K. De and E. G. Friedman, "Low-voltage-swing monolithic dc-dc conversion", IEEE Transactions on Circuits and Systems II: Express Briefs, Vol. 51, No. 5, pp. 241-248, 2004.

[134] G. Yang, G, B .H. Stark, S. J. Hollis, S. G. Burrow, "Challenges for energy harvesting systems under intermittent excitation", Emerging and Selected Topics in Circuits and Systems, IEEE Journal on, doi:10.1109/JETCAS.2014.2337172.

[135] Uddin M J, Masud M G, Ghosh A, Middya T R and Chaudhuri B K Ammonium dihydrogen phosphate/ PVA composite films with high dielectric constant and enhanced thermal stability Adv. Sci. Eng. Med. 5 126-5 2013

[136] Emfit corp. https://www.emfit.com/bed-alarm-fall-wandering-prevention

[137] Wang Y, Li T, Yang H. Nanofabrication, effects and sensors based on micro-electro-mechanical systems technology. Phil Trans R Soc A 371: 20120315. http://dx.doi.org/10.1098/rsta.2012.0315 2013

[138] James Marchetti ; Yie He ; Olaf Than and Sandeep Akkaraju "Efficient process development for bulk silicon etching using cellular automata simulation techniques", Proc. SPIE 3514, Micromachined Devices and Components IV, 287 (September 8, 1998); doi:10.1117/12.323900; http://dx.doi.org/10.1117/12.323900

[139] Koschwanez, J. H., Carlson, R. H. & Meldrum, D. R. "Thin PDMS Films Using Long Spin Times or Tert-Butyl Alcohol as a Solvent". PLoS ONE 4, e4572 (2009).